UC Berkeley
Working Papers

Title

Experimental Studies on High Speed Vehicle Steering Control with Magnetic Marker Referencing System

Permalink

https://escholarship.org/uc/item/6pq1x2tb

Authors

Tan, Han-Shue

Bougler, Bndicte

Publication Date

2000-05-01

Experimental Studies on High Speed Vehicle Steering Control with Magnetic Marker Referencing System

Han-Shue Tan
Bénédicte Bougler

The contents of this report reflect the views of the authors who are responsible for the facts and the accuracy of the data presented herein. The contents do not necessarily reflect the official views or policies of the State of California. This report does not constitute a standard, specification, or regulation.

CALIFORNIA PARTNERS FOR ADVANCED TRANSIT AND HIGHWAYS

Experimental Studies on High Speed Vehicle Steering Control With Magnetic Marker Referencing System

Han-Shue Tan and Bénédicte Bougler

Final Report MOU 259

California PATH

University of California at Berkeley

1357 S. 46th Street, Richmond, CA 94804-4698

hstan@path4.its.berkeley.edu

Abstract

This project is a one-and-half year research and experimental effort that builds on the results of as well as supplements the efforts in MOU 250, "Experimental Studies on Vehicle Control Systems." It focuses on an emerging issue of the high-speed steering control: how to conduct robust automatic vehicle steering control at highway speed based on a look-down lateral sensing system. The research results from MOU 250 have indicated that a look-down lateral sensing system based on magnetometers under the front bumper was not adequate to perform high speed lane-keeping function. Additional look-ahead capability will be required at high speed to deal with the increase of the vehicle lateral delay and the reduction of the vehicle lateral damping force.

The research completed under this project contributed to four sets of deliverables: (1) a comprehensive research report which presents the analysis and experimental results of the development of the robust high speed lane-keeping automated steering control system based on the magnetic marker lateral reference system, (2) a journal paper (*IEEE/ASME Transactions on Mechatronics*) detailing the general development of the automated steering vehicle based on roadway magnets, (3) a journal paper (*IEEE/ASME Transactions on Mechatronics*) presenting the analysis results of the influence of the suspension roll dynamics to vehicle steering control, and (4) demonstrations of high speed robust lane-keeping control at I-15 test track in San Diego.

1 Executive Summary

This project is a one-and-half year research and experimental effort, which supplements the tasks of MOU 250, "Experimental Studies on Vehicle Control Systems." This report focuses on an emerging issue of the high-speed steering control: how to conduct robust automatic vehicle steering control at highway speed based on a look-down lateral sensing system. The experimental work from MOU 250 has concluded that a look-down lateral sensing system based on magnetometers under the front bumper was not adequate to perform high speed lane-keeping function. Additional look-ahead capability would be required at high speed to deal with the increase of the vehicle lateral delay and the reduction of the vehicle lateral damping force. Under MOU 250, installation of additional magnetometers under the rear bumper has been proposed to create a virtual sensor in front of the vehicle to improve the look-ahead capability. The validation of the effectiveness of the new control architecture and the confirmation of the analysis of the high speed vehicle dynamics, both are crucial to the advancement of the technology for implementing lateral control in the AHS environment, will be presented in this report.

PATH has conducted research on vehicle lateral control since 1987, concentrating on the concept of a cooperative lateral control system using discrete magnetic markers and a preview control algorithm. Both theoretical and experimental work have been conducted to (1) develop and experiment with a signal processing scheme for accurately measuring the vehicle's lateral displacement, and a coding strategy for encode curvature information in the road reference system; (2) develop a preview control algorithm using Frequency Shaped Linear Quadratic (FSLQ) theory; (3) experiment with the reference/sensing system and the control algorithm for lane-keeping using a scaled experimental vehicle; (4) experiment with the integrated system for lane-keeping at low vehicle speeds at Richmond Field Station (RFS) using a full size vehicle; (5) develop and experiment with a fuzzy rule-based control algorithm for lane-keeping; (6) develop and open-loop experiment at low vehicle speed a lane change algorithm with lateral position estimated by yaw rate sensor and lateral accelerometer; (7) develop and open-loop validate a model-based tire burst control strategy; (8) design and construct a new intermediate test site at Golden Gate Field (GGF) parking lot

for vehicle experiments up to 55 MPH; and (9) conduct vehicle lateral control experiments based on two lane-keeping algorithms, one based on the vehicle kinematics and the Nyquist Criterion, the other on FSLQ, both with preview control, for speeds up to 50 MPH at GGF test track.

The period of performance of MOU 259 was originally from May 1996 to April 1997, and later extended to December 1997. Part of this period was also parallel to the preparation of the 1997 National Automated Highway System (AHS) Consortiums Demonstration. Results of both MOU 250 and 259 have been applied to and validated at the preparation of the demonstration. The AHS Demonstration took place in August 1997 in an eight-mile automated highway at I-15 in San Diego. It was requested by the U.S. Congress to demonstrate technical feasibility of AHS. The PATH platoon demonstration was one of the key elements of the demonstration. The PATH demonstration included eight Buick LeSabre's traveling at a spacing of 6.5 meters at highway speeds using integrated longitudinal and lateral control system. The control functions demonstrated included: lane keeping, lane-changing, close spacing longitudinal control, and platoon split and join. The test data at I-15 has shown that the lateral control system kept the vehicles within 5 centimeters to the lane center at freeway speeds with curve transition error of less than 10 centimeters. It is also worth mentioning that no single failure has occurred for the lateral control system throughout the 4-day demonstration period.

The project incorporates four major tasks:

- Task 1 comprised the validation of the high-speed vehicle characteristics.

- Task 2 comprised development of lateral sensing system based on both front and rear magnetometers.

- Task 3 comprised development of robust lateral control algorithms based on front and rear lateral displacement measurements.

- Task 4 comprised experimental evaluation of the new robust lane-keeping algorithm up to 55 MPH.

Task 1 studied the experimental identification of the vehicle lateral characteristics. PATH has conducted open loop frequency sweep to verify the lateral vehicle characteristics for both Pontiac and LeSabre test vehicles. Various amplitudes of steering commands, with frequencies ranging from 0.1 Hz to 6 Hz, were used to steer the vehicle at speeds of 22, 45, and 67 MPH (10, 20 and 30 m/s respectively). Two methods of data analysis have been employed to validate the methodology used and to double-check the frequency responses obtained. The two methods from two different sets of data yielded almost identical results. These data analysis concluded the following: (1) the bicycle model, vehicle lateral dynamics based on linear lateral mode and yaw mode, is sufficient to characterize the vehicle lateral behavior for the Pontiac test vehicle up to about 3 Hz, (2) LeSabre is much more "understeer" than the Pontiac test vehicle, i.e., the lateral characteristics of LeSabre is more sensitive to vehicle speed changes, (3) the frequency response from steering command to lateral acceleration at CG of LeSabre has a deeper notch effect at between 1 to 2 Hz than what the bicycle model predicts, and (4) this particular "zero" behavior coincides with the fundamental suspension mode of LeSabre. Since LeSabre test vehicle has a much softer suspension than that of Pontiac 6000, the soft suspension creates additional phase lag that limited the achievable bandwidth of the automated steering control to below the suspension frequency and made the high speed automated steering control design more difficult. Vehicle lateral model that includes vehicle suspension dynamics has been developed and has confirmed that this "notch" effect is indeed contributed by the suspension roll dynamics. Furthermore, analysis based on this model reveals that the natural control configuration to overcome such significant phase constraints is a "look-ahead" steering control algorithm. See [Appendix A] for the discussion of the influence of suspension roll dynamics to vehicle steering control.

Task 2 focused on the development of a reliable magnetometer sensor signal-processing algorithm that included the construction of a modularized lateral software structure. The modularized lateral software is crucial for long-term lateral control system development and sensor integration. PATH has determined to use a three-magnetometer sensor combination to provide wider lateral displacement measurement of the vehicle for the demonstration. Signal processing software and signal conditioning board have been developed for the

integration of the three sensors. The final lateral sensor range has been increased from ±15 cm to ±45 cm. In order to provide smooth transition among three magnetometers PATH has also developed software for switching among these sensors. PATH has completed the development of integrating the front and rear magnetometers to provide smooth front and rear lateral displacement measurements. PATH researcher has also extended the magnetometer calibration process and the reconstructive software development tool that were developed through MOU 250 for the front magnetometers to both front and rear sensors. The automated process for magnetometer table calibration was developed to speed up the calibration process. The "reconstructive" software system was developed to improve the reliability and reduce the development time of the lateral sensing system with the magnetic road markers. The reconstructive development tool generated the identical signal processing software in a desktop computer as the one ran in the real-time vehicle environment in the same QNX operating system. The inputs to this software were all the sensor data that stored during real vehicle testing. In such setup, any erroneous situation can be recreated in a lab environment and debug with ease. PATH has also linked the extensive Matlab data processing ability to this tool in a laptop computer so that the debugging process could be automated. With this new development environment, PATH staff could (1) capture the problematic performance as soon as it happens, (2) recreate the situation step by step in the lab environment, and (3) modify the software as well as validate the changes before upgrading the new version of software in the test vehicle. This tool had significantly shortened the development time for the integrating the rear and the front magnetometers. PATH staff has utilized this tool and checked through every magnet in the test tracks at both Richmond Field Station and Golden Gate Field.

The goal of Task 3 is to develop an automated lateral control system based on the magnetic marker lateral reference system that operates at highway speeds with extremely high reliability. To achieve this goal, it is necessary to first examine the relationships among vehicle dynamics, performance requirements, actuator bandwidth, lateral displacement sensing mechanism and automatic control methodologies. This study will provide the basic understanding of both analytical and practical limitations facing the

design of an automatic vehicle lateral control system as well as suggesting the design directions in practice. The analytical study was first conducted using mathematical model and computer simulation, and then verified by experiments. The conclusions describe the practical limitations of designing automatic lane keeping systems based on a "look-down" lateral reference mechanism at highway speeds. These limitations are resulted from the interactions among the following factors: (a) the additional time and phase lags coinciding with "bad" zero locations of vehicle dynamics when operated at high speed, (b) soft suspension roll characteristics that creates significantly phase lag and becomes the strongest constraints for using only one look-down sensor for high speed operation, (c) the practical limitation of the actuator bandwidth, (d) the inherent noise characteristics of the discrete lateral reference system as well as of inertia sensors mounted in a vehicle, (e) the requirement of high controller gain to satisfy both the high precision lane-keeping performance and the good robustness property against various operating conditions, and (f) the preference of low control gain to achieve passenger comfort. To design and to implement a robust lateral control system, PATH has performed the following tasks: (1) define a strong lateral control objectives that includes practical considerations and analyze appropriate control strategies, (2) design system software and hardware structures, (3) validate vehicle lateral dynamics, (4) develop reliable sensing system and signal processing algorithm with added sensor range, (5) incorporate steering actuator into overall control system design, (6) use both front and rear lateral sensors to improve the "bad" zero condition and desensitize against soft suspension roll dynamics, (7) design robust control algorithm, and (8) integrate software and experiment with extensive vehicle testing. Task 3 focuses the discussion of (1), (6), and (7). A unique "frequency shaped look-ahead" steering control law was designed as the robust lane-keeping control algorithm. See the *IEEE/ASME Transactions on Mechatronics* paper titled "Development of an Automated Steering Vehicle Based on Roadway Magnets - A Case Study of Mechatronic System Design." [Appendix B] for the detailed discussion.

The purpose of Task 4 is to implement the frequency-shaped look-ahead steering control algorithm based on front and rear magnetometers and to evaluate the resultant performance on the test tracks. Acceptable performance tradeoff and robustness

properties are validated and convincingly demonstrated at high vehicle speed with practical scenarios. The resultant automated steering control system was demonstrated by PATH at the 1997 NAHSC Demonstration. The test data at I-15 indicated that this automated steering control system keeps the vehicle within 5 centimeters to the lane center at freeway speeds except with maximum error less than 10 centimeters during curve transitions. The high-g Miramar Mini Demo has demonstrated up to 0.5 g lateral acceleration with 95% of the tracking error within 10 centimeters under the same control algorithm..

The work done to accomplish the above four tasks is detailed in the next four sections. For further information, the reader should consult the appended papers.

2   Vehicle Lateral Characteristics Verification

2.1   Vehicle Lateral Characteristics of Test Vehicles

PATH has conducted open loop frequency sweep to verify the lateral vehicle characteristics for both Pontiac and LeSabre test vehicles.

Open loop steering commands that consisted of sine waves with amplitude 1, 2 and 3 road degrees with frequencies ranging from 0.1 Hz to 5 Hz were selected as the inputs to the Pontiac test vehicle. These different steering inputs were then used to excite the vehicle lateral dynamics with speeds of 20, 40 and 60 MPH. Lateral acceleration, yaw rate, steering command and tire angle were stored for off-line analysis. Through these over 70 data files, the open loop vehicle lateral frequency response of the Pontiac test vehicle has been identified. This procedure also verified that the bicycle model, vehicle lateral dynamics based on linear lateral mode and yaw mode, is sufficient to characterize the vehicle lateral behavior for the Pontiac test vehicle up to about 3 Hz. Furthermore, the actuator installed in Pontiac has a gain-bandwidth of about 4.5 Hz. The actuator contributed 180 degree phase lag at 4.5 Hz to the lateral vehicle transfer function from steering command to lateral acceleration. This phase lag creates a strong limitation to the

achievable system bandwidth of the automatic steering control system. See Figure 2.1 and 2.2 show the frequency characteristics of the Pontiac test vehicle.

Analysis performed on the identified vehicle lateral model verified also that the vehicle lateral dynamics depends strongly on the vehicle longitudinal speed. The higher the vehicle speed, the more phase lag between the vehicle steering angle and the lateral acceleration. The further the sensor to the front of the CG, the more the phase lead would be recovered for the vehicle. The additional phase lead would create better stability margin for the automatic steering control problem. In addition, the identified open loop vehicle characteristics also pointed out the understeer nature of the Pontiac. The higher the speed, the larger the radius of curvature Pontiac would negotiate with the same steering angle. This suggested that preview steering angle based on geometric behavior would produce larger mismatch when the vehicle is traveling at higher speed.
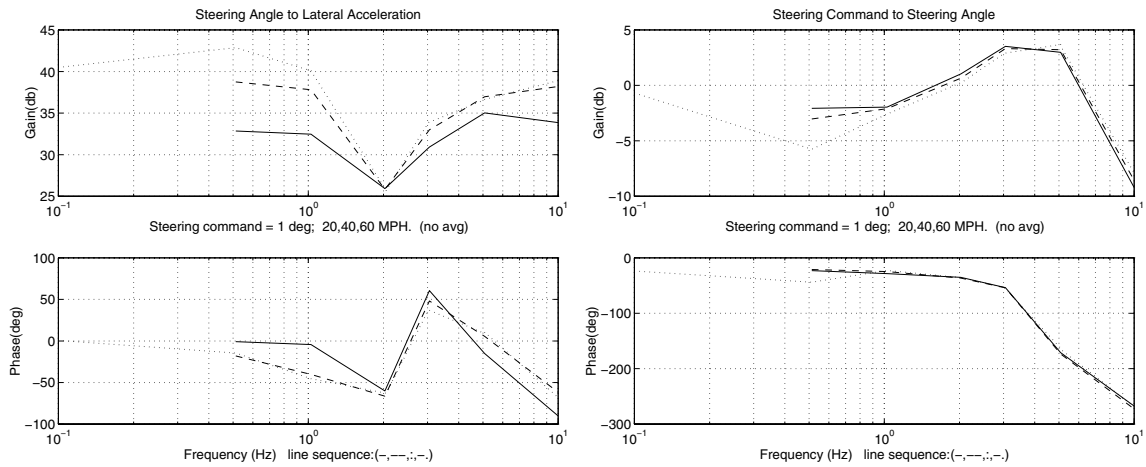

Fig. 2.1. Pontiac Lat. Dynamics (Lat. Accel.)   Fig. 2.2 Pontiac Lat. Dynamics (Yaw rate)

PATH has conducted open loop frequency sweep to verify the lateral vehicle model for the LeSabre test vehicle at Crows Landing. Various amplitudes of steering commands, with frequencies ranging from 0.1 Hz to 6 Hz, were used to steer the vehicle at speeds of 22, 45, and 67 MPH (10, 20 and 30 m/s respectively). Two methods of data analysis have been employed to validate the methodology used and to double-check the frequency responses obtained. Figure 2.3 and 2.4 show the frequency characteristics of the LeSabre test vehicle. The two methods from two different sets of data yielded almost identical

9

results. These data analysis concluded the following: (1) LeSabre is much more understeer than Pontiac 6000, the old test vehicle; the lateral characteristics of LeSabre is therefore more sensitive to vehicle speed changes, (2) the frequency response from steering command to lateral acceleration at CG of LeSabre has a deeper notch effect at between 1 to 2 Hz than what the bicycle model predicts, and (3) this particular "zero" behavior coincides with the fundamental suspension mode of LeSabre. Incidentally LeSabre has a much softer suspension than that of Pontiac 6000. The soft suspension creates additional phase lag that limits the achievable bandwidth of the automated steering control to below the suspension frequency and made the high-speed automated steering control design more difficult.
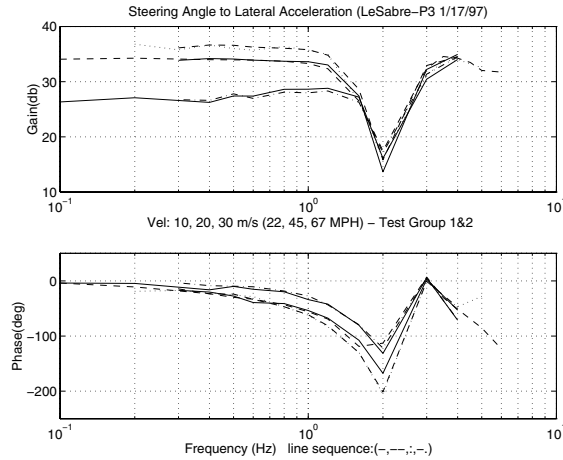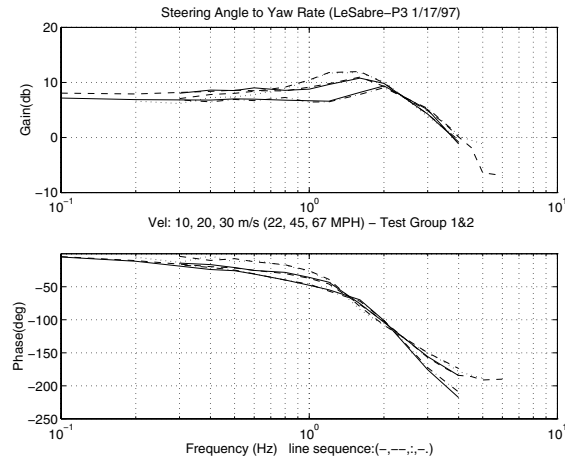

Fig. 2.3. LeSabre Lat. Dynamics (Lat. Accel.)   Fig. 2.4 LeSabre Lat. Dynamics (Yaw rate)

2.2   *Vehicle Lateral Model with Roll Dynamics*

The initial model identification result indicated a strong influence from the suspension roll dynamics to the vehicle lateral behavior. The conventional linearized bicycle model, which includes lateral and yaw dynamics, can not represent the lowered gain and phase characteristics in the frequency range from 1 to 4 Hz. This is attributed to the vehicle roll dynamics, which is affected by suspensions. In order to validate and to investigate the effect of suspension to steering control, a nonlinear 3 DOF vehicle model (as depicted in Fig. 2.5) is derived in Appendix A to comprehensively describe the coupling between the lateral, yaw and roll dynamics and is also used for controller design analysis. A linear 3

DOF model is simplified from the nonlinear model to validate with the experimental data both in frequency and time domains. Eq. 2.1 describes this linear 3 DOF vehicle model.
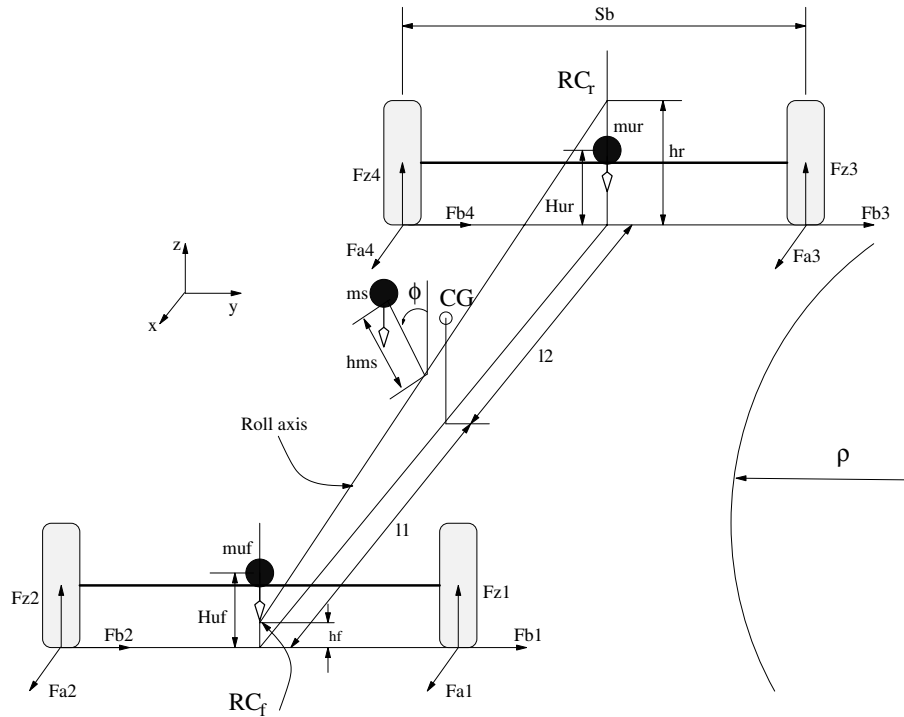

Fig. 2.5. Schematic Diagram of 3 DOF Vehicle Model

$$\frac{d}{dt}\begin{bmatrix} y_r \\ \dot{y}_r \\ \varepsilon_r \\ \dot{\varepsilon}_r \\ \phi \\ \dot{\phi} \end{bmatrix} = \begin{bmatrix} 0 & 1 & 0 & 0 & 0 & 0 \\ 0 & \dfrac{A_1 \cdot \Lambda_1}{V} & -A_1 \cdot \Lambda_1 & \dfrac{A_2 \cdot \Lambda_1}{V} & R_1 & R_2 \\ 0 & 0 & 0 & 1 & 0 & 0 \\ 0 & \dfrac{A_3}{V} & -A_3 & \dfrac{A_4}{V} & R_3 & 0 \\ 0 & 0 & 0 & 0 & 0 & 1 \\ 0 & \dfrac{A_1 \cdot \Lambda_2}{V} & -A_1 \cdot \Lambda_2 & \dfrac{A_2 \cdot \Lambda_2}{V} & R_4 & R_5 \end{bmatrix} \begin{bmatrix} y_r \\ \dot{y}_r \\ \varepsilon_r \\ \dot{\varepsilon}_r \\ \phi \\ \dot{\phi} \end{bmatrix} + \begin{bmatrix} 0 \\ B_1 \Lambda_1 \\ 0 \\ B_2 \\ 0 \\ B_1 \cdot \Lambda_2 \end{bmatrix} \delta + \begin{bmatrix} 0 \\ D_1 \\ 0 \\ D_2 \\ 0 \\ D_3 \end{bmatrix} \qquad (2.1)$$

Where

$$A_1 = \frac{-2}{M}(C_1 + C_2)$$

$$A_2 = \frac{2}{M}(-l_1 \cdot C_1 + l_2 \cdot C_2)$$

$$A_3 = \frac{2}{I_z}(-l_1 \cdot C_1 + l_2 \cdot C_2)$$

$$A_4 = \frac{-2}{I_z}(l_1^2 \cdot C_1 + l_2^2 \cdot C_2)$$

$$B_1 = \frac{2(C_1 + F_x)}{M}$$

$$B_2 = \frac{2C_1 \cdot l_1(F_x + C_1)}{I_z}$$

$$\Lambda_1 = (\frac{MI_{x_s}}{MI_{x_s} - m_s^2 h_{m_s}^2})$$

$$\Lambda_2 = \frac{Mm_s h_{m_s}}{MI_{x_x} - m_s^2 h_{m_s}^2}$$

$$R_1 = \frac{2(\gamma_1 l_1)I_{x_s} + m_s h_{m_s}(m_s gh_{m_s} - K_1 - K_2)}{MI_{x_x} - m_s^2 h_{m_s}^2}$$

$$R_2 = \frac{-m_s h_{m_s}(D_1 + D_2)}{MI_{x_x} - m_s^2 h_{m_s}^2}$$

$$R_3 = \frac{2(\gamma_1 l_1 - \gamma_2 l_2)}{I_z}$$

$$R_4 = \frac{2m_s h_{m_s}(\gamma_1 + \gamma_2) + M(m_s gh_{m_s} - K_1 - K_2)}{MI_{x_x} - m_s^2 h_{m_s}^2}$$

$$D_1 = \frac{\Lambda_1}{M}F_{wy} + \frac{A_2 \Lambda_1}{V}\dot{\varepsilon}_d - V^2\rho$$

$$D_2 = -\frac{2(l_1^2 C_1 + l_2^2 C_2)}{I_z V}\dot{\varepsilon}_d$$

$$D_3 = \frac{\Lambda_2}{M}F_{wy} + \frac{A_2 \Lambda_2}{V}\dot{\varepsilon}_d - 2\Lambda_2 V^2\rho$$

Both the linear 3 DOF vehicle model and the bicycle model have been used to validate with the test data. A typical bicycle model can be either obtained from the deviation in Appendix B or from Eq. (2.1) by eliminating the roll state variable ϕ by letting the CG of the sprung mass passing through the roll axis ($h_{m_s} = 0$). Using the procedure detailed in Appendix A, the model transfer functions can be matched with the test responses. The open loop transfer functions from steering angle to lateral acceleration of both the 3 DOF model and the bicycle model are shown in Fig. 2.6. The close matches confirm the significant lateral dynamics contribution from the suspension roll characteristics in LeSabre. The resultant identified vehicle parameters are listed in Table 2.1.
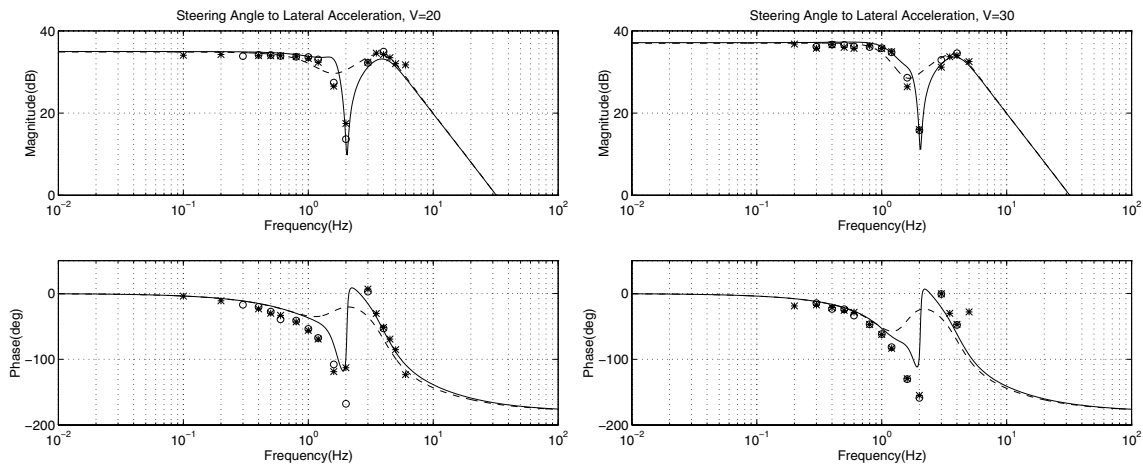

Fig. 2.6. Frequency Response from Steering Angle to Lateral Accel. with V=20,30m/s

(Two set of test data (*,o), 3DOF model (-), Bicycle model (--))

Table 2.1 The 3 DOF Vehicle Parameters

Vehicle mass (M):	1740 kg
Sprung mass (m_s)	1600 kg
Front unsprung mass (m_{uf})	80 kg
Rear unsprung mass (m_{ur})	60 kg
Roll inertia (Ix_s):	420 $kg.m^2$
Yaw inertia (Iz):	3214 $kg.m^2$
Front tire cornering stiffness (C_1):	29000 N/rad
Rear tire cornering stiffness (C_2):	60000 N/rad
Front axle to CG (l_1):	1.058 m
Rear axle to CG (l_2):	1.756 m
Front sensor to CG (d_f):	1.758 m
Rear sensor to CG (d_r):	2.456 m
Wheel base (s_b):	1.5 m
Roll damping (D_i):	1000 $N \cdot \sec/m$
Roll stiffness (K_i):	2000 $N-m$
Sprung mass center to sprung mass (hm_s):	0.38 m
Height of front unsprung mass (h_{uf}):	0.3 m
Height of rear unsprung mass (h_{ur}):	0.35 m
Center of front unsprung mass (h_f):	0.25 m
Center of rear unsprung mass (h_r):	0.75 m
Roll steering coefficient (γ):	1000
Actuator damping ratio (ξ):	0.4
Actuator natural frequency (ω_n):	5 Hz

2.3   Controller Design w/wo the Effect of Roll Dynamics

The µ-synthesis and H_∞ optimization [1, 2] are used in this report to obtain the "equivalent" robust controllers based on the two vehicle models, the 3 DOF linear model and the bicycle model, developed with and without the suspension roll dynamics. These two controllers will be designed based on the identical performance indexes with the same synthesis. Since the two vehicle models differ from each other only in the area of roll coupling, a fair comparison is therefore established. Performance of these two controllers will then be evaluated to investigate the effect of the roll dynamics. See Appendix A for the detailed discussion of the controller design.

Using the analysis results in Appendix A, two robust controllers using the same weighting functions, one designed based on the 3 DOF model, the other one on the bicycle model are simulated on the same nonlinear 3 DOF model for performance comparison. The simulated maneuvers are defined as first following a straight road and then a curved road with 0.1g curvature from t=1 to 9 sec, and finally back to straight road again. A 200Nt wind gust happened at t=6 sec is also included. Performance specifications include tracking errors less than 0.2m, actuator bandwidth of 5Hz, measurement noise of 0.02m and good ride quality. Controllers are designed by D-K iteration for both models under different velocities as discussed in Appendix A. The frequency responses of the two controllers are shown in Fig. 2.7 as V = 20 m/s.
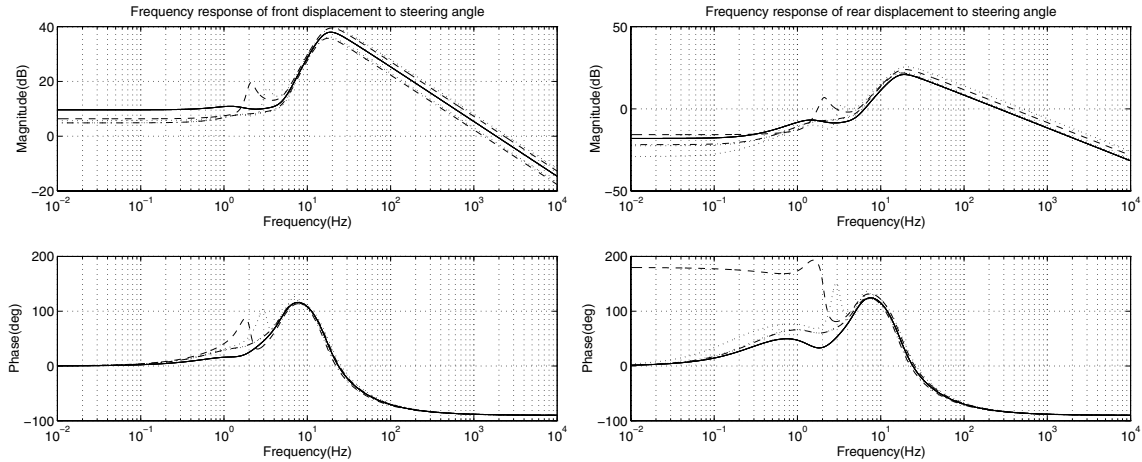

Fig. 2.7. Frequency Responses of Front and Rear Controllers

[Bicycle model(-); 3DOF: K_i=20000(--), K_i=40000(.), K_i=200000(-.), K_i=2*10^{10}(-..-)]

From Fig. 2.7 different controller characteristics can be observed around the suspension frequency. In the right figures, the controller with soft suspension for the rear sensor provides larger phase lead at lower frequencies than those with stiff suspensions. More specifically, under closer examination, the rear controller with soft suspension (K_i=20000) exhibits 180-degree phase lead at low frequency when compared to those from the stiffer suspension. This result using the robust controller synthesis implies that a "look-ahead" steering controller scheme (which exhibits such phase characteristics) is a natural solution to deal with the difficult lateral control problem imposed by the soft suspension.

14

In order to study the different closed-loop performance from the controller design by the 3 DOF model and the bicycle model, two simulation cases are shown for comparison:

- Controller designed by the bicycle model is applied on several nonlinear 3 DOF vehicle models with different suspension stiffness as shown in Fig. 2.8.

- Controller designed by the 3 DOF model with soft suspension (K_i=20000) is applied on the same nonlinear 3 DOF vehicle models with different suspension stiffness as shown in Fig. 2.9.
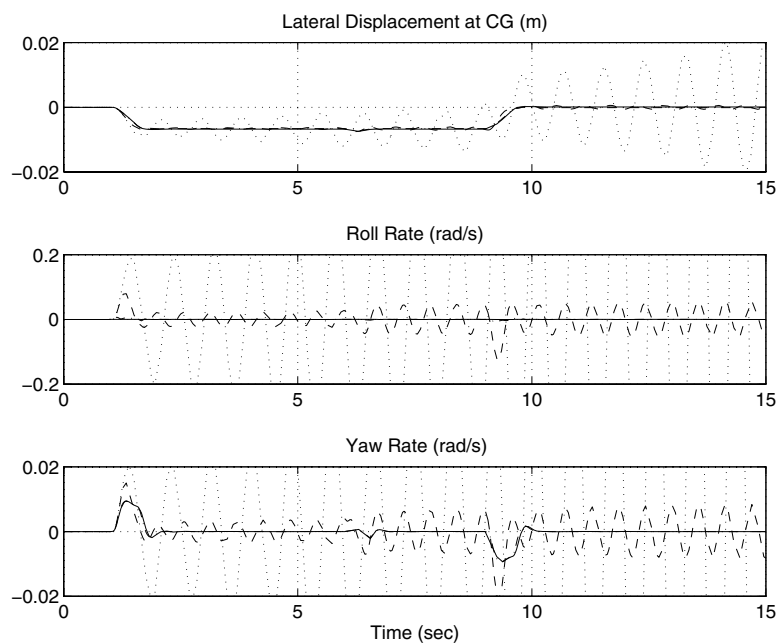

Fig. 2.8. Closed loop Response for Bicycle Controller with v=20m/s and 20% uncertainty
[K_i=20000(--), K_i=40000(.), K_i=200000(-.), K_i=2*10^{10}(-...-)]

20% parameter variation of the cornering stiffness is considered in both cases to also examine the robustness. It can be seen that both controllers provide similar responses for model with stiff suspension. It is interesting to note that the controller designed based on a 3 DOF model with soft suspension exhibits similar performance to that from a bicycle model even when the suspension turns out to be very stiff. The closed-loop responses with the controller designed by the bicycle model could become unstable as the suspension becomes "too" soft, while the 3 DOF controller still satisfies the performance criterion. Since the 3 DOF controller considers the suspension mode at the design stage,

15

it provide better stability and performance than the bicycle model controller. Moreover, these simulation results exemplify the potential detrimental coupling effect of the roll dynamics to the vehicle steering control.
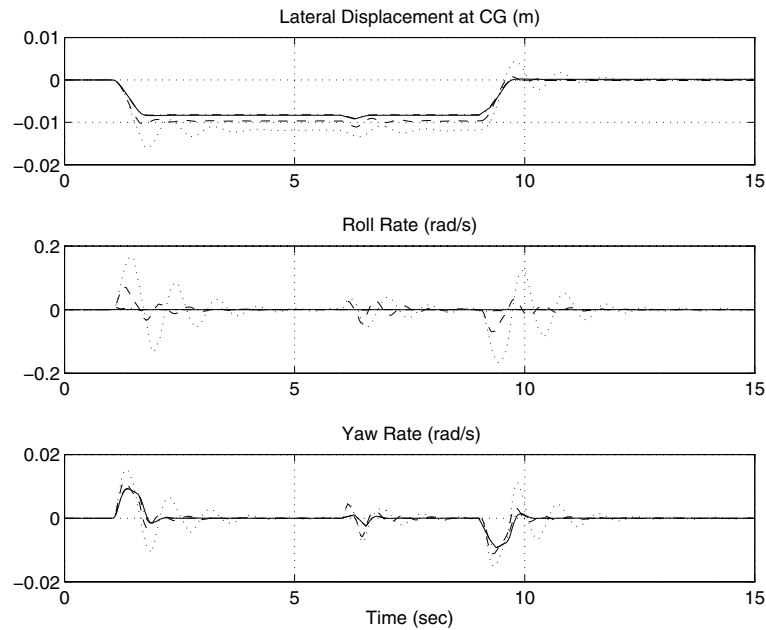

Fig. 2.9. Closed loop Response for 3DOF soft Controller at (K_i=20000) with v=20m/s and 20% uncertainty [K_i=20000(--), K_i=40000(.), K_i=200000(-.), K_i=2*10^{10}(-..-)]

3   Lateral Sensing System Development

The development of a reliable and accurate lateral referencing system is crucial to the success of the lateral control and guidance system. PATH has developed the use of magnetic markers embedded in the road center to provide the lateral position and road geometric information [3]. Extensive development and experimentation has been performed on magnetic marker-based lateral sensing systems for many PATH vehicles equipped with automated steering control. The positive characteristics of this lateral sensing technique include good accuracy (better than one centimeter), highly reliability, insensitivity to weather conditions, and support for binary coding. The requirement of modifying the infrastructure (installing magnets) and the inherited "look-down" nature (the sensor measures lateral displacement at location within vehicle physical boundaries, versus look-ahead ability) of the sensing system [4] are two noticeable limitations of this

16

technology. Although the associated application software for this sensing system can be quite involved, the principle is straightforward. Magnetic markers (nails) are installed under the roadway delineating the center of each lane. Magnetometers mounted under the vehicle sense the strength of the magnetic field as the vehicle passes over each magnet. Onboard signal processing software calculates the relative displacement from the vehicle to the magnet based on the magnetic strength and the knowledge of the magnetic characteristics of the marker. This computation is insensitive to the vehicle bouncing (e.g., heave and pitch) and the ever-present natural and man-made magnetic noises. Furthermore, the road geometric information can be encoded as a sequence of bits, with each bit corresponding to a magnet [5]. The polarity of each magnet represents either 1 or 0 in the code. In addition to the lateral displacement measurement and road geometry preview information, other vehicle measurements such as yaw rate, lateral acceleration, and steering wheel angle may also be used to improve the performance of such lateral guidance system.

This section describes the background information on both the magnetic marker concept and the development of a reliable magnetometer sensor signal-processing algorithm.

3.1   *Magnetic Marker Model*

A representative mathematical model of the magnetic marker provides a base for understanding of many important issues regarding the design of a reliable signal-processing algorithm. Among these issues, how to reliably detect the magnets, how to remove the effect from vehicle bounces, and how to desensitize the noise disturbance effects, are the key problems that determine the effectiveness of any algorithm. Particularly the researchers from PATH have chosen to model the markers as magnetic dipoles for analysis purpose. Aside from its relative simplicity and compactness, extensive testing at the Richmond Field Station reveal a strong correlation between model prediction and empirical measurements [3, 6].

Under the dipole assumption, the magnetic field, $\vec{B}(x,y,z)$, at some location, $\vec{P}(x,y,z)$, can be given by

17

$$\vec{B} = \frac{\mu_0 M}{4\pi\, r^5} \left(3xz\vec{i} + 3yz\vec{j} + (2z^2 - x^2 - y^2)\vec{k}\right)$$ (3.1)

where $r = \sqrt{x^2 + y^2 + z^2}$, μ_0 is the permeability of the open space, and M is the magnetic moment of the magnetic marker. Also noted that the coordinate system ($\vec{P} = x\vec{i} + y\vec{j} + z\vec{k}$) is chosen so that $x\vec{i}$ corresponds to the direction of vehicle travel, $y\vec{j}$ the lateral deviation, and $z\vec{k}$ the height, relative to the marker's center.

From Equation (3.1), it is clear that, at any given longitudinal location x, in particular at x=0, there exists a one-to-one and into mapping from the magnetic field $\vec{B}(0, y, z)$ to the sensor location (0,y,z). Therefore it is theoretically plausible to invert this mapping to obtain the lateral deviation as well as the sensor height at the sensor location just as the vehicle passing over each magnet (x=0). The method of inverting this mapping is not unique. It can be analytical, numerical, or experimental. One crucial determination factor of designing a real-time algorithm of the inverse mapping is the tradeoff between the algorithm's effectiveness of handling noise and the algorithm's complexity.

3.2 Noise Effect

Four major noise sources are usually present in the magnetic signal measurements in a typical vehicle operational environment. They are: earth field, local magnetic field distortion, vehicle internal electromagnetic field, and electrical noise.

The most frequent external disturbance is the ever-present earth's permanent magnetic field, which is usually in the order of half a Gauss. The value of the earth field measured by the magnetometers on the vehicle depends on the location of the vehicle on earth as well as the attitude and orientation of the vehicle. Although the earth magnetic field usually change slowly, sharp turns and severe braking could quickly change the value of measurements along the vehicle axes.

The most serious noise problems are caused by local anomalies due to the presence of structural supports, reinforcing rebars, and the ferrous components in the vehicle. Power

line under ground is another source of such local field distortion. Rebar or structural support usually creates a sharp change in the background magnetic field and sometimes is difficult to identify. Most signal process algorithms would have some limitations to recover from such sharp distortions. The ferrous components in the vehicle, on the other hand, could be isolated as long as their locations are fixed with respect to the magnetometers.

A third source of noise comes from the alternating electric fields generated by various motors operating in the vehicle. These motors may include alternator, fan, electric pump, compressor and other actuators. However, their effects vary according to the motor rotational speeds and its distance to the magnetometers. The higher the motor rpm or the farther it is placed away from the magnetometers, the less the effect of the resultant noise is. Sometimes a modest change in sensor placement can alter the size of such disturbance.

The last common noise source arises from the electronical noise in the measurement signal itself. Such noise can be created by the voltage fluctuations in the electrical grounding or from the power source. It can also be a result of poor wiring insulation against electromagnetic disturbances. Usually, the longer the wire, the higher such noise is. Although low pass filter sometimes reduces the magnitude of such disturbance, noticeable degradation of the magnetic sensor signal process algorithm occurs when such noise level exceeds 0.04 Gauss,

3.3   Magnetic Sensing Algorithm

One of the important attribute of the lateral sensing system is its reliability. Currently, there exists several algorithms designed to detect the relative position between the marker and sensor (magnetometer), as well as to read the code embedded within a sequence of these markers. Three magnet marker detection and mapping algorithms have been experimented by PATH [3, 6]. The first is called the "peak-mapping" method that utilizes a single magnetometer to estimate the marker's relative lateral position when the sensor is passing over the magnet. The second algorithm is the "vector ratio" method and it requires a pair of magnetometers to sample the field at two locations. It returns a

sequence of lateral estimates in a neighborhood surrounding, but not including the peak. The third is the "differential peak-mapping" algorithm that compares the magnetic field measurements at two observation points to eliminate the common-mode contributions and reconstructs a functional relationship between the differential sensor readings and the lateral position using the knowledge of the sensor geometry. The "peak-mapping" algorithm is chosen for the LeSabre because it has been proven effective over a wide range of speeds and has been widespread applied in many experiments conducted at PATH.

Under the assumption that the vehicle lateral speed is significantly smaller than that of the vehicle longitudinal velocity, it is obvious that the largest vertical field B_z occurs at the point when the sensor is just passing over the magnetic marker, i.e. as x=0. This point is called "peak" because it corresponding to the point where the magnetic field achieves its maximum during its trajectory around the magnetic marker in question. The most important fact is that the three dimensional mapping as in Equation (3.1) can be reduced to a two dimensional mapping using the constraint relationship x=0.

Two basic methods can be used to detect the peaks: the variance method (using B_z) and the switching (using B_x) method. The variance method computes the instantaneous variance of the vertical field $\sigma_z(t_k)$ as

$$\sigma_z(t_k) = \sum_{i=k-N}^{k} \left(B_z(t_i) - \overline{B}_z(t_k) \right)^2 \tag{3.2}$$

where $\overline{B}(t_k)$ is the running average of the last N samples, i.e.,

$$\overline{B}_z(t_k) = \frac{1}{N} \sum_{i=k-N}^{k} B_z(t_i) . \tag{3.3}$$

Using this variance, the peak and the valley of the vertical field can be identified using the following relationship

$$\text{if } \left| B_z(t_k) - \hat{B}_{zEarth} \right| > HIGH\_threshold \ \& \ \sigma_z(t_k) < \varepsilon \ \Rightarrow \text{Peak detected,} \tag{3.4}$$

$$\text{if } \left| B_z(t_k) - \hat{B}_{zEarth} \right| < LOW\_threshold \; \& \; \sigma_z(t_k) < \varepsilon \; \Rightarrow \text{Valley detected.} \tag{3.5}$$

Equation (3.5) suggests that the marker is far away enough to the sensor that the field from the magnetic marker is negligible. Thus the earth field estimates (B_{zEarth}, B_{yEarth}): vertical and horizontal earth field, can be updated based on the sensor measurements at the valley. It should be noted that the earth estimates play a very important role in the accurate computation of the lateral deviation.

To improve the reliability of the peak detection process, the switching method utilizes the sign-change property of the longitudinal field (B_x) at peak both to provide candidates for peaks and to double-check any detected peak.

Once the peak is detected and the marker's magnetic field is computed as

$$B_{zMar\,ker} = B_z(t_m) - \hat{B}_{zEarth}, \text{ and } B_{yMar\,ker} = B_y(t_m) - \hat{B}_{yEarth}. \tag{3.6}$$

By setting $x=0$ on Equation (3.1), the slope function between the vertical and horizontal field of $\vec{B}_{Mar\,ker}$ can be expressed as

$$\frac{B_{zMar\,ker}}{B_{yMar\,ker}} = \frac{2z^2 - y^2}{3yz} \equiv \varphi(y, z). \tag{3.7}$$

It is known from calculus that the curve (B_z, B_y) form a field if $\varphi(y, z)$ is single-valued, or that partial derivatives of $\varphi(y, z)$ do not vanish. Since

$$\frac{\partial^2 \varphi(y, z)}{\partial y \partial z} = \frac{y^2 - 2z^2}{3y^2 z^2} \neq 0, \text{ as long as } y \neq \sqrt{2}z, \tag{3.8}$$

under the restriction that $y \in \{y_{min}, y_{max}\}$ and $z \in \{z_{min}, z_{max}\}$, with $z_{min} > 0$ and $y_{max} < \sqrt{2}z_{min}$, the curve $\{B_{yMar\,ker}, B_{zMar\,ker}\}$ does form a field. Therefore, the inverse mapping from $\{B_{yMar\,ker}, B_{zMar\,ker}\}$ to $\{y, z\}$ does exist for most of our application where z_{min} is usually greater than 15 cm and y_{max} is less than 20 cm.

A typical inverse map is shown in Fig. 3.1 where two sets of calibration data, one at 9 centimeter height and the other at 11 centimeter, for the vertical and horizontal field of the marker are collected at the interval of every 2 centimeter lateral displacement. One advantage of this method is its robustness against height variations. Observe from Fig. 3.1 that changes in z only serves to move the coordinates along the radial lines that denote constant y.
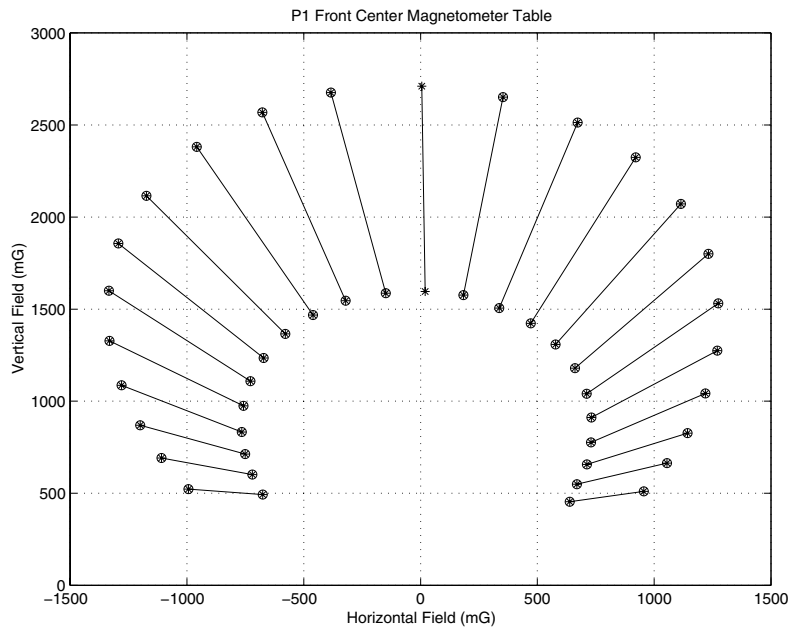

Fig. 3.1 LeSabre Front Center Magnetic Table

3.4 *Signal Processing Algorithm*

The magnetometer signal-processing for the "peak-mapping" method involves the following three procedures: peak detection, earth field removal and lateral displacement table look-up (see Figure 3.2 for block diagram of signal processing algorithm). Although it is straightforward in principle, it becomes complicated when the reliability of the process is the major concern. There are many parameters in the lateral sensing signal processing software needed to be tuned in order to provide consistent lateral displacement information regardless of vehicle speeds, orientations, operating lateral offsets and vehicle body motions. Debugging can become very time consuming when the failure

condition could not be recreated. To improve the reliability of the lateral sensing system with the magnetic road markers, PATH has developed a "reconstructive" software system for the lateral sensing signal processing. When specified as a "reconstructive run", the real-time software in the vehicle, besides processing data as usual, stores all sensor data in the memory and later dumped into a data file. Identical signal processing software as the one run in the real-time environment can later on be generated in a desk top computer using the data stored during vehicle testing as inputs with the same QNX operating system. In such setup, any erroneous situation can be recreated in a lab environment and debug with ease. With this new development environment, the developers could (1) capture the problematic performance as soon as it happens, (2) recreate the situation step by step in the lab environment, and (3) modify the software as well as validate the changes before upgrading the new version of software in the test vehicle.

Three magnetometers were installed under both the front and rear bumpers to extend the range of the lateral sensor. The resultant signal-processing algorithm achieved combined sensor range of ±50 centimeters with accuracy better than 1 centimeter. An independent lateral measurement has shown that the standard deviation of such measurement was under 0.4 centimeter. Furthermore, the ratio of miss-reading magnet was less than 0.1% for speeds up to 90 mph under various loading conditions.
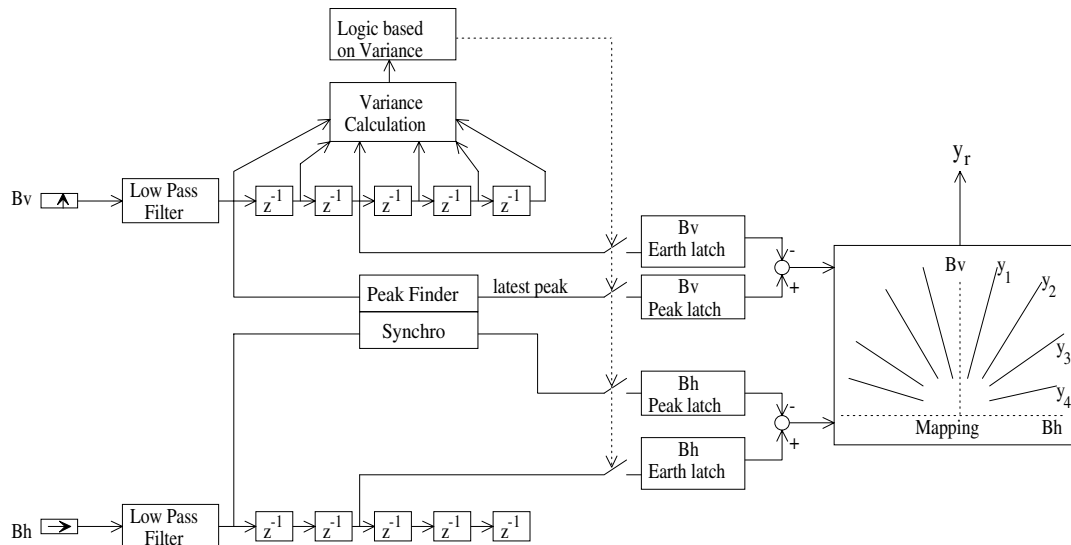

Figure 3.2 "Peak-Mapping" Magnetometer Signal Processing Block Diagram

4 High Speed Robust Lateral Control

4.1 System Configuration, Requirements and Design Philosophy

Four basic system components are required for an automated steering control system: (1) road markers or any other kind of road indicators that define the road, (2) sensors recognizing the road markers, (3) intelligence to determine how to steer, and (4) steering actuator that steers the wheels. The lateral reference system employed by the PATH demonstration is based on the magnetic markers embedded under the roadway center. Such reference system is generally more reliable due to the relatively short distance between the roadway magnets and the sensors (magnetometers) in the vehicle. However, the "look-down" nature of this sensing system creates a difficult control problem when high speed and high control authority are required [4]. An add-on brushless DC motor mounted on the upper steering column was chosen to be the steering actuator. Using the existing hydraulic assist system for steering power, such actuator design is relatively simple and potentially inexpensive. However it also produces an interesting servo design problem that pushes the bandwidth of the steering actuator close to the natural frequency of the handwheel mass and steering column. A Pentium 166 MHz PC computer with rugged chassis is used to perform both signal processing and real-time control functions.

The performance requirements for the demonstration of the automated steering control system were straight forward: the steering control system needed to perform both automated lane-keeping and lane-change maneuvers at highway speeds with good tracking accuracy and good passenger comfort. In order to negotiate the Mini Demo sharp curves, the automated vehicle needed to maintain at least 0.3-g lateral acceleration without ever coming close to the lateral sensor limit (±50 centimeters). Finally, extremely high reliability was required for a safe public demonstration.

The closed-loop system performance requirements were then flown down from the demonstration requirements. These performance requirements included the following:

(1) 0.15 meter maximum tracking error for highway driving and 0.3 meter maximum error for 0.3-g automated steering maneuvers without any prior knowledge of the roadway;

(2) no noticeable oscillations at frequencies above 0.3 Hz for passenger comfort, and 0.4 minimum damping coefficient for any mode at lower frequencies;

(3) 1 m/s^2 maximum lateral acceleration deviation between the lateral acceleration created by the vehicle and that from the road;

(4) consistent performance under various vehicle operating conditions.

The corresponding subsystem requirements were generated from the system performance requirements. These subsystem requirements are summarized as follows:

(1) at least 1 centimeter accuracy for the lateral displacement measurements,

(2) 0.1% maximum rate of miss-reading markers on the highway,

(3) 5 Hz minimum steering actuator bandwidth during normal operation.

Finally, the following limitations were imposed as the practical constraints for the control system:

(1) 2 centimeter maximum lateral error on the marker installation,

(2) 25 degree per second maximum rate of steering angle change when measured at the tire,

(3) existence of 0.005 rad/sec yaw rate sensor noise in addition to the possible sensor drift.

The objective was to develop a reliable automated steering control system that achieved all the above requirements. The process included the design and integration of reliable sensing system, reliable actuator, robust controller and robust decision-making. Since the fine tuning of the controller based on exact vehicle parameters was almost impossible for such scenarios, the philosophy of the controller design was to attain an acceptable performance under even the worst scenario. The concept of using "high gain" lane-

keeping controller was adopted to achieve the robustness against various environmental conditions, whereas soft trajectory planning was used for maintaining passenger comfort. The key concept was the realization of the fact that every process in the integration design was crucial for the final success of the product.

4.2   Control System Analysis

A linearized model is sufficient for studying vehicle steering under *normal* conditions [7]. Assuming small angles, this allows to use the classical *bicycle model* shown in Fig. 4.1. The transfer function from steering angle to the lateral acceleration produced at the sensor location S (d_s in front of the CG) is:

$$\ddot{y}_S(s) = V_S(s)\delta_f(s) = \frac{\mu c_f v^2 (M l_f d_S + I_\psi)s^2 + \mu^2 c_f c_r lv(d_S + l_r)s + \mu^2 c_f c_r lv^2}{D(s)}\delta_f(s) \qquad (4.1)$$

with $D(s) = I_\psi M v^2 s^2 + \mu v(I_\psi(c_f + c_r) + M(c_f l_f^2 + c_r l_r^2))s + \mu M v^2(c_r l_r - c_f l_f) + \mu^2 c_f c_r l^2$,

where I_ψ is the yaw moment of inertia, M the mass of the vehicle, μ the road adhesion coefficient, $l = l_f + l_r$ the wheel base, c_f and c_r the cornering stiffness of the front and rear tires respectively and v the longitudinal vehicle speed. The front wheel steering angle δ_f is realized by the actuator $A(s)$. The desired lateral acceleration at S is $\ddot{y}_{ref} = v^2 \rho_{ref}$, with the road curvature ρ_{ref}. This yields the vehicle lateral model as shown in Fig. 4.2, where the subsystems are identified as: (I) vehicle kinematics, (II) force generation mechanism, (III) road reference and (IV) steering actuator.
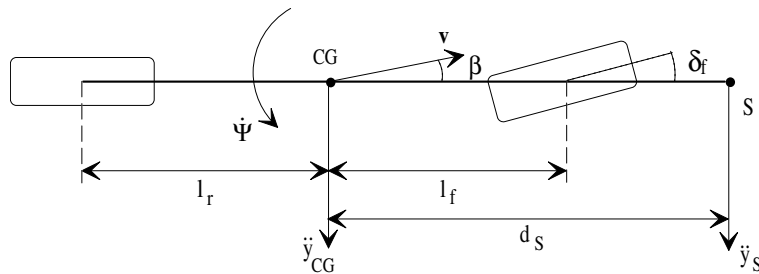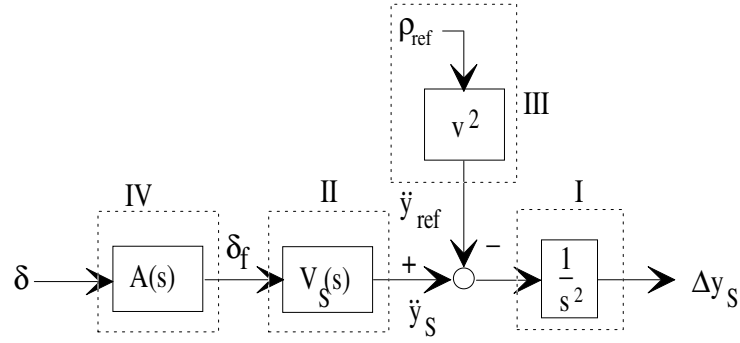

Fig. 4.1. Bicycle Model
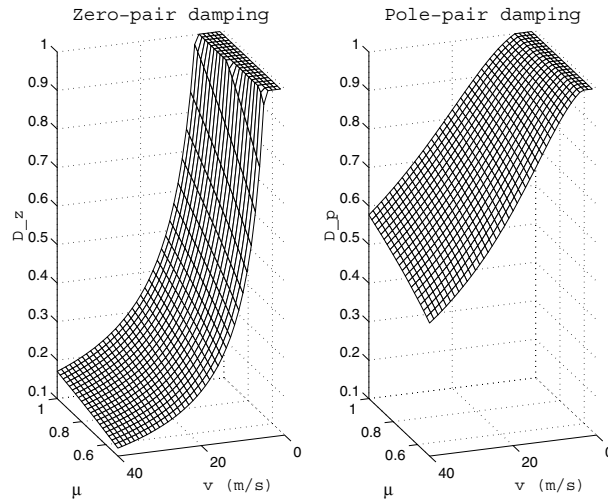
Fig. 4.2. Block Diagram of Vehicle System Dynamics

Fig. 4.3. Vehicle Pole-Zero Damping Ratio (μ: coefficient of road adhesion, v: vehicle speed)

In order to study the effect of lateral displacement output feedback, the pole-zero locations of the vehicle dynamics $V_s(s)$ are first examined with the sensor located under the front bumper. Fig. 4.3 shows the rapid decrease in pole and zero damping in $V_s(s)$, with increase of velocity and deterioration of road surface. Any high gain controller tends to drive the closed-loop poles towards the open-loop zeros, resulting in poorly damped closed-loop poles. A perfect pole-zero cancellation is impossible because of the system parameter uncertainties. However, attempting to cancel the $V_s(s)$ zeros by a pair of poles would result in a poorly damped imperfect pole-zero cancellation. Moreover, the lightly damped poles introduced by the controller would show up in yaw dynamics, without the corresponding zeros cancellation. This would result in excessive fish-tailing of the vehicle. The above analysis concludes that a pure lateral displacement output feedback is

27

impractical for highway speed automated steering control under the given performance requirements and design constraints [4, 8].

The above discussion suggests modifying the system control structure. Three possible options were considered: preview with the road curvature information, inertial sensor feedback, and modification of the system zeros. When the curvature information is known to the vehicle [5, 7], a feed-forward term based on the road curvature and vehicle dynamics can be generated in the controller to lessen the need for high gain feedback. However, due to uncertainty in $V_s(s)$, especially at high speeds, the feed-forward calculations are at best an approximation. Furthermore, a strong feedback control is still the key for a robust system; the feedforward control does not alleviate the stability and noise rejection problems. A feedback scheme utilizing the feedback of the inertial sensors like accelerometer and yaw rate can also be used to change the pole locations. However, these schemes can not modify the poorly damped zeros of $V_s(s)$. In turn, the closed-loop poles still are attracted towards the lightly damped zeros and lead to poor closed-loop characteristics. Thus, neither road preview feedforward control nor inertial sensor feedback control is efficient for dealing with the high-speed steering control problem.

Since the system zeros of $V_s(s)$ are determined by the sensor location S, a proportional increase of d_s to speed v seems to be required -- an observation known from human driving. Moreover, the modification of d_s does change the location of zeros in $V_s(s)$. A virtual look-ahead concept was therefore proposed for the look-down lateral sensing system [4, 8]. Complementing the lateral displacement sensor S at the front bumper by a second displacement sensor T, preferably placed at the tail of the vehicle, extrapolates the displacement measurement forward to a virtually increased look-ahead distance d_v beyond the vehicle boundaries. Furthermore, the analysis results in Section 3 suggest that a natural system configuration solution to deal with the difficult control problem imposed by the additional phase lag from the soft suspension is a virtual "look-ahead" steering control method. This "virtual look-ahead" concept turns out to be the key break-through that allows for the high gain robust steering controller design.

4.3   Control Algorithm Development

In order to experimentally validate the analysis results in both Section 3 and 4 concerning the advantages of the virtual look-ahead concept, various look-ahead distances were experimented on the LeSabre. A constant proportional feedback steering control with varying virtual look-ahead distance (from 0 to 10 car length virtual look-ahead distances where one car length equals to 4.8 meters) was first implemented in the LeSabre and experimented at I-15 with different vehicle speeds. The experiments concluded the following observations:

(1) The shorter the look-ahead distance is, the more oscillatory the closed-loop lateral mode is.

(2) The longer the look-ahead distance is, the larger both the actuator mode oscillation and the high frequency noise are.

The additional look-ahead distance creates the needed phase-lead starting from the yaw natural frequency, however this also comes with the side effect of increasing controller gains at higher frequencies. With the soft suspension of the LeSabre, high control gain above 1 Hz is likely to excite the suspension oscillation, especially at high vehicle speeds. Therefore as one increases the look-ahead distance, one has to reduce the overall controller gain. This generates large steady state error when large virtual look-ahead distance is used.

Many different control algorithms have been tested with the virtual look-ahead concept. Among them, a simple controller such as PI (proportional plus integration) control achieved automated steering control for speeds up to 70 mph at I-15 using several car length virtual look-ahead distance [9]; link control concept [103] where the vehicle is towed by an imaginary link that connects to the road center several car length ahead of the vehicle, also achieved 65 mph automatic highway lane-keeping. However, the PI controller prefers lower controller gain in order to maintain good passenger comfort, thus limits its ability for robust performance. The link controller is stiff at high frequencies and it tends to excite the vehicle suspension mode. Both controllers use feedforward steering input based on preview road curvature to reduce the need for large controller gains. The

main conclusions from these exercises are (1) the virtual look-ahead concept helps tremendously in the steering controller design, and (2) the frequency-shaped capability needs to be incorporated into the virtual look-ahead concept to reduce the adverse effects from extrapolating two potentially noisy measurements.

The control algorithm needs to satisfy both tracking accuracy and ride comfort requirements at all possible vehicle speeds regardless of the following uncertainties: road adhesion variations, preview errors, loss of road curvature information, marker installation misalignments, actuator bandwidth, vehicle dynamics changes, soft suspension modes, and all reasonable sensor and vehicle noises. A frequency shaped virtual look-ahead lane-keeping control algorithm using the form of the following equation was developed and implemented:

$$steer = -k_c G_c \left(\left(k_{\text{int}} + k_e k_{ext} \right) y_f - k_e k_{ext} y_r \right), \tag{4.2}$$

where k_{int} is the integrator at front sensor location, k_{ext} the virtual sensor extension filter, G_c the compensator at the virtual sensor location, k_e and k_c constants that can be tuned, y_f and y_r the lateral measurements at front and rear sensors respectively. The transfer functions of these frequency shaped filters are shown in Fig. 4.4. This algorithm consists of three elements:

(1) an integral control (k_{int}(s)) that keeps the steady state tracking error at the front sensor to zero,

(2) a frequency shaped look-ahead distance (k_{ext}(s)) that provides more look-ahead distance around the vehicle lateral modes and roll-off of the look-ahead distance at higher frequencies,

(3) a servo controller (g_c(s)) that uses the frequency shaped virtual displacement as input and compensates it for the actuator and suspension dynamics.
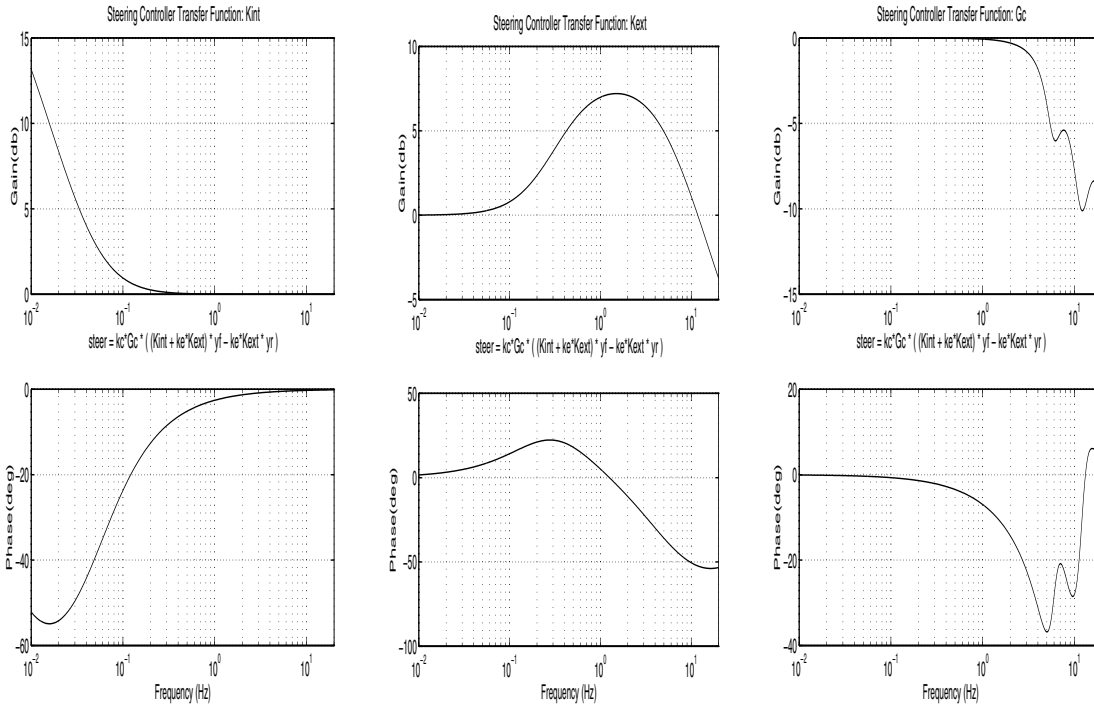
| Fig. 4.4.1 Kint (integrator) | Fig. 4.4.2. Kext (look-ahead) | Fig. 4.4.3. Gc (overall comp) |

Lane-keeping experiments at speeds up to 90 mph were conducted without preview information at I-15 using the frequency shaped virtual look-ahead controller with constant controller parameters. Adding the feedforward steering command based on curvature preview information provides slightly better tracking error (by a few centimeters) during changes of curvature. The overall standard deviation of tracking error is less than four centimeters even at such high speeds.

In order to minimize the adverse effect from any misalignment of the magnet markers, a gain-scheduling scheme was incorporated into the lane-keeping control algorithm to provide a better tradeoff between passenger comfort and tight tracking control. The gain-scheduling scheme consists of a single parameter that changes the magnitude of the controller gain in such a way that the steady state gain decreases with increasing virtual look-ahead distance. A built-in hysteresis, which is applied only when the controller gain is reduced, is employed to eliminate excessive switching. High gain is used in the following situations: low vehicle speed, large tracking error, large lateral acceleration, and large curvature if the road information is known. Otherwise, low gain will be chosen.

31

The scheme provides a single controller that achieves an overall tradeoff among robustness, tightness and comfort.

As part of the preparation of the 1997 NAHSC Demonstration, the robustness properties of the lane-keeping control algorithm were tested extensively on the I-15 test track. Test scenarios included missing magnets, missing coding information, loss of preview information, sudden tight curve transition, high vehicle speeds, and various passenger loading conditions. With several thousand-miles traveling under automated steering control, the lane-keeping algorithm was experimentally validated to be robust against all the above conditions.

5   Demonstration Results

Eight Buick LeSabres were used in the platoon demonstration on the I-15 lanes, as well as one vehicle on the Mini Demo track. These vehicles were supported by add-on hardware devices and control software in order to deliver automated driving features such as close space following and tight lane tracking. Fig. 5.1 illustrates the components in the test vehicle that relate to the steering control function.
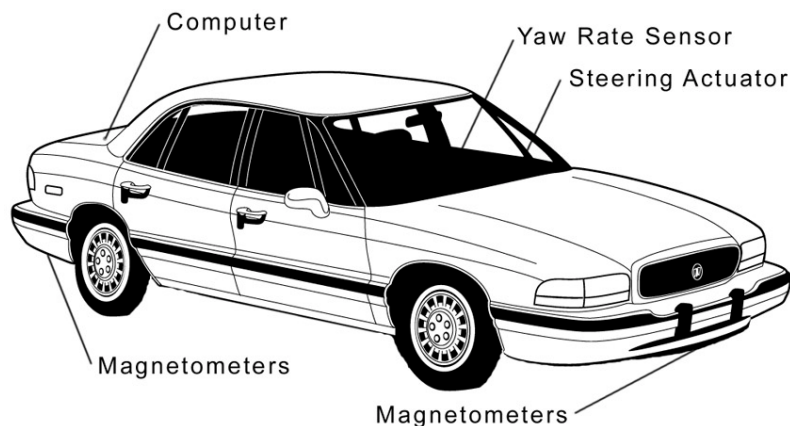

Fig. 5.1. Buick LeSabre Test Vehicle

Many data were collected and reviewed during the NAHSC preparation and demonstration. The test data at I-15 revealed that the tracking errors were generally

within 5 centimeters with a maximum lateral error of 10 centimeters during curve transition at highway speed. Taking into account that the magnet installation error is generally within 1.5 centimeters and that the standard deviation of the measurement error is about 0.4 centimeter, the steering controller is shown to maintain a consistently good tracking accuracy. The same algorithm as the one used for highway driving was applied to the high-g exhibition demonstration at the Miramar Mini Demo with consistent and robust performance. Over 1500 passengers rode in the automated vehicles, and no single failure occurred on the automated steering control system in all nine automated vehicles. The following figures present the capability, robustness, and versatility of the developed automated steering control system.

Fig. 5.2 compares the steering performance between that of an experienced human driver and that of the automated steering control system for speed up to 80 mph. No road preview information was used during this test run. Comparable lateral acceleration (standard deviation --STD: 0.24 m/s^2, maximum acceleration: 0.9 m/s^2) to a skilled manual driver (STD: 0.23 m/s^2, maximum acceleration: 1.2 m/s^2) was observed at I-15 but with much smaller tracking error for the automated steering system (STD of 3 vs. 11 centimeters, maximum error of 14 vs. 49 centimeters).
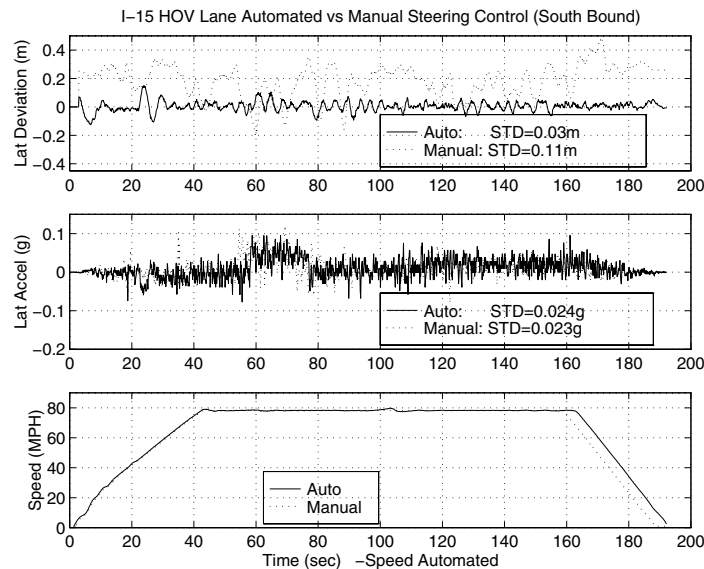

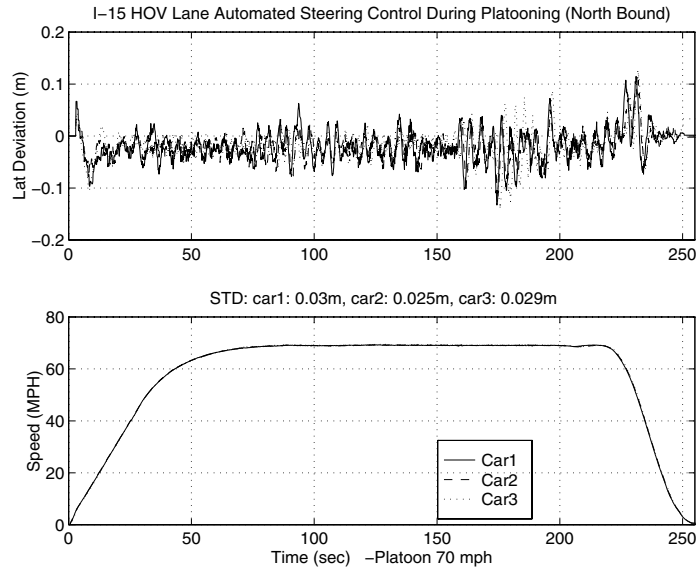Fig. 5.2. Automated vs. Manual Steering Comparison

Fig. 5.3. Platoon Automated Steering Control Performance

Fig. 5.3 shows the automated lane-keeping performance during a platoon demonstration at 70 mph at I-15. The standard deviations of the tracking error for cars number 1, 2 and 3 are 3.0, 2.5 and 2.9 centimeters, respectively. The tracking errors stay within 9 centimeters over 99% of the time. Furthermore, the tracking performances among these three cars are almost identical at every location, which also demonstrates the consistency of the automated steering control algorithm. It is worthwhile noticing that identical steering controller is used in every vehicle.
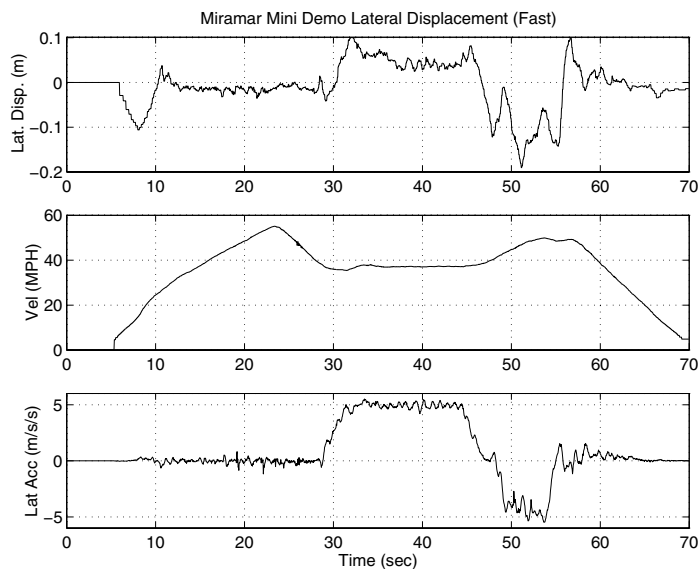

Fig. 5.4. Automated Steering Control Performance at Miramar Mini Demo
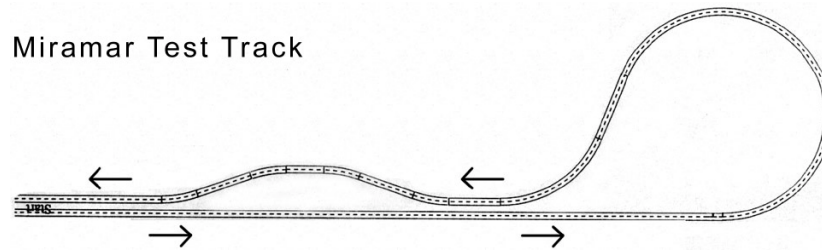
34

Fig. 5.5. Miramar Mini Demo Test Track Map

Fig, 5.4 illustrates the data from the Miramar Mini Demo where the lane-keeping capability was demonstrated through the high-g automated maneuver on a demanding test track. The automated steering control has consistently been demonstrated up to 0.5-g lateral acceleration with 95% of the tracking error within 10 centimeters. A couple of sharp transitions (54 meters radius of curvature) exhibit 20 centimeters tracking error but only during short transitions. Up to 0.7-g lateral acceleration has been maintained at the Miramar Demo site, however the demonstration speed was chosen to be far lower. Fig. 5.5 shows a map for the Miramar Demo test track.

6   Conclusion

Many results of MOU 259 have been applied to and validated at the preparation of the 1997 August AHS Demonstration in an eight-mile automated highway at I-15 in San Diego. The demonstration was requested by the U.S. Congress to demonstrate the technical feasibility of AHS. The PATH platoon demonstration was one of the key element of the demonstration and it included integrated longitudinal and lateral control systems in eight Buick LeSabre traveling at a spacing of 6.5 meters at highway speeds. The test data at I-15 has shown that the lateral control system kept the vehicles within 5 centimeters to the lane center at freeway speeds with curve transition error of less than 10 centimeters. The high-g Miramar Mini Demo has demonstrated up to 0.5 g lateral acceleration with 95% of the tracking error within 10 centimeters. It is also worth mentioning that no single failure has occurred for the lateral control system throughout the 4-day demonstration period. The results of MOU 259, especially the robust steering

control based on the "virtual look-ahead" concept, helped to prove the feasibility of the automated lateral control using magnetic marker reference system in practice.

## 7	References

[1]	J. C. Doyle, K. Glover, P.P. Khargonekar and B.A. Francis, "State-space Solution to Standard H_2 and H_∞ Control Problems," *IEEE Trans*., AC-34, 1989, pp. 831-847.

[2]	A. Parkard and J. Doyle, "The Complex Structure Singular Value," *Automatica*, vol. 29, 1993, pp. 71-109.

[3]	W.-B. Zhang, R. E. Parsons and T. West, "Intelligent Roadway Reference System for Vehicle Lateral Guidance and Control," United State Patent, 5347456, Sept. 13, 1994.

[4]	J. Guldner, H.-S. Tan, and S. Patwardhan., "Analysis of Automatic Steering Control for Highway Vehicle with Look-down Lateral Reference Systems," *Vehicle System Dynamics*, vol. 26, no. 4, pp. 243-269, 1996.

[5]	J. Guldner, S. Patwardhan, H.-S. Tan and W.-B. Zhang, "Coding of Road Information for Automated Highways," *ITS Journal*, vol. 4, no. 3-4, 1999, pp. 187-207.

[6]	H. Pham, "A Differnetial Magnetic Marker Sensing Algorithm: As Used in the 1996 Honda Accord AHS Vehicles: Final Report," PATH Draft Research Report, no. D98-011, 1998.

[7]	Peng, H. and M. Tomizuka, "Vehicle lateral control for highway automation", *Proc. American Control Conf.*, San Diego, CA, USA, 1990, pp. 788-794.

[8]	Chen, C and H.-S. Tan, "Steering Control of High Speed Vehicles: Dynamic Look Ahead and Yaw Rate Feedback*,"* in *Proceedings of the 37th IEEE Conference on Decision and Control*, pp. 1025-1030, Tampa, Florida, USA, Dec. 1998.

[9] Guldner, J., H.-S. Tan, and S. Patwardhan, "Study of Design Directions for Lateral Vehicle Control," *Proceedings of the 36th IEEE Conference on Decision and Control*, San Diego, CA, 1997.

[10] Patwardhan, S., H.-S. Tan, J. Guldner and M. Tomizuka, "Lane Following During Backward Driving for Front Wheel Steered Vehicles," in *Proc. American Control Conf.*, Vol. 5, pp. 3348-3353, Albuquerque, NM, USA, 1997.

8   Appendix

[A] K.-T. Feng, H.-S. Tan and M. Tomizuka, "The Influence of Suspension Roll Dynamics to Vehicle Steering Control," *IEEE/ASME Transactions on Mechatronics*, (submitted) 1999.

[B] H.-S. Tan, J. Guldner, S. Patwardhan, C. Chen and B. Bougler, "Development of an Automated Steering Vehicle Based on Roadway Magnets - A Case Study of Mechatronic System Design," *IEEE/ASME Transactions on Mechatronics*, vol. 4, no. 3, Sept., 1999, pp. 258-272.

The Influence of Suspension Roll Dynamics to Vehicle Steering Control[1]

Kai-Ten Feng[2], Han-Shue Tan[3] and Masayoshi Tomizuka[2]

Abstract

The two dominant motions of automatic vehicle steering control are yaw and lateral motions. A two degree-of-freedom (DOF) model commonly used to describe these motions is called the bicycle model. Experimental results for certain vehicles have shown some frequency characteristics that can not be explained by the bicycle model. In this paper, a 3 DOF model, which incorporate the suspension roll mode, is developed and verified against the experimental data. The results attribute the discrepancy in the frequency characteristics to the vehicle suspension, especially the roll dynamics. The fundamental coupling between the roll and lateral modes is addressed in this paper using the linear 3 DOF model. The μ-synthesis and H_∞ theory is applied to both the bicycle model and the linear 3 DOF model for a comparison study of robust steering controller design. The simulation results highlight the importance of the effect of roll dynamics to steering control, especially for vehicles with soft suspensions.

1 Introduction

Two fundamental tasks involved in automatic vehicle control are the longitudinal and lateral motion control. The longitudinal control problems involve vehicle speed regulation and platoon spacing control problems [1]. The lateral control problems are concerned with automatic

---

[2] Department of Mechanical Engineering, University of California, Berkeley.

[3] California PATH, Institute of Transportation Studies, University of California, Berkeley

steering of vehicles with lane following and lane change maneuvers. One application of such technology is the Automatic Highway Systems (AHS). An increasing amount of research have been motivated and are investigated worldwide in several programs, shch as ITS in the US (see e.g. [2]) and ASV, SSVS and ARTS under ITS Japan [3]. An overview of system studies of the highway automation can be found in [4].

In the field of vehicle lateral control, most researchers have considered yaw and lateral motion as the dominant vehicle dynamics in steering control [5]-[11]. A commonly used vehicle model describing the vehicle yaw and lateral motion is the bicycle model. Frequency shaped linear quadratic (FSLQ) control with preview has been applied by Peng and Tomizuka [5] for lateral control of passenger cars. Sliding mode control (SMC) was presented by Pham et al. [6] for combined lateral and longitudinal control of vehicles. A fuzzy rule-based controller was designed by Hessburg and Tomizuka [7] with experimental varification. Steering Controls based on virtual look ahead were proposed and successfully demonstrated to highway speeds by Tan et al. [8][9]. Decoupling of lateral motion and yaw motion was proposed by Ackermann [10] using yaw rate feedback and Chen and Tan [11] with dynamic look ahead. Most of the research in designing vehicle lateral controllers have been based on the bicycle model. Experimental data for certain vehicles with soft suspensions, however, suggest that the frequency response from steering input to lateral acceleration exhibits lowered gain characteristics over the frequency range around 1-4Hz, which can be attributed to suspension dynamics. This implies that the steering input may experience large excursions in this frequency range comparing with that from the bicycle model, which may adversely affects safety and ride comfort.

In contrast to using the bicycle model for the design of steering controller, considerably less research [12]-[15] has been conducted by utilizing the three degree-of-freedom (DOF) vehicle model, which includes the lateral, yaw and suspension roll dynamics. Segel [12] developed a linear 3 DOF vehicle model with relatively stiff syspension system. Nisonger and Wormley [13] proposed dual-axle steering controllers on a 3 DOF model. Yeh and Wu [14] presented a decoupling controller for a four-wheel 3 DOF steering vehicle. However, the influence of the suspension roll dynamics to the lateral steering control has not been emphasized in previous research. The effectiveness of utilizing the 3 DOF vehicle model instead of the bicycle model have not been discussed.

The objectives of this paper are to validate and to investigate the effect of suspension to steering control. A nonlinear 3 DOF vehicle model is proposed to comprehensively describe the

coupling between the lateral, yaw and roll dynamics and is used for performance evaluation. A linear 3 DOF model is simplified from the nonlinear model to validated with the experimental data both in frequency and time domains. The analysis has shown that the roll dynamics can be decoupled from the lateral motions either when the suspension stiffness approaches infinity or if the center of gravity (CG) of the vehicle sprung mass passes through the roll axis of the vehicle. In this paper, the μ-synthesis and H_∞ optimal control technique are utilized to provide a fair comparison study for lateral controller design with and without considering the suspension mode. The variation of the tire cornering stiffness is considered using the design of robust controllers. Comparisons between these two controllers show the advantages of including roll dynamics in the design of lateral controllers, especially for vehicle with soft suspension.

The paper is organized as follows: Section 2 shows the experimental data for open loop vehicle dynamics. Section 3 developed a nonlinear 3 DOF vehicle model and the corresponding linear model. Model validation with the test data is investigated in Section 4. Section 5 discusses the coupling mechanism between the roll and lateral dynamics. Section 6 presents the design of robust controllers with and without the effect of roll dynamics. Section 7 shows the comparison of the closed-loop performace by simulation results. Conclusions are given in Section 8.

2 Problem Description and the Vehicle Data

For the purpose of investigating the effect of roll dynamics on the vehicle's lateral motion, experiments were conducted by using a *Buick LaSabre*, a full-size sedan with relatively soft suspension. This vehicle is one of the test vehicles used in the 1997 NAHSC (National Automated Highway Systems Consortion) demonstration in San Diego [16]. The vehicle was equipped with a lateral accelerometer and a yaw rate sensor both installed around the vehicle's CG. Two sets of magnetic sensors, three under the front bumper and three under the rear bumper, were also installed to measure the lateral displacement of the vehicle with respect to the road reference. By using the frequency sweep technique, the experimental open loop frequency responses from steering angle to yaw rate and lateral acceleration can be obtained and are shown in Fig. 1. Experiments were performed at three different velocities, 10, 20, and 30 m/sec. As seen in the figure, the frequency response gain for lateral acceleration drops

over the frequency range centered around $2Hz$, which can not be predicted by the bicycle model. This frequency concides with that of the vehicle suspension roll dynamics observed by the driver. The early steering control experimentation based on the bicycle model using these vehicles has also exhibited excessive oscillations in this frequency range from time to time. This indicated the potential need of including roll dynamics in the steering controller design. A vehicle model including the roll dynamics is developed in next section to establish the foundation that will substantiate this point.
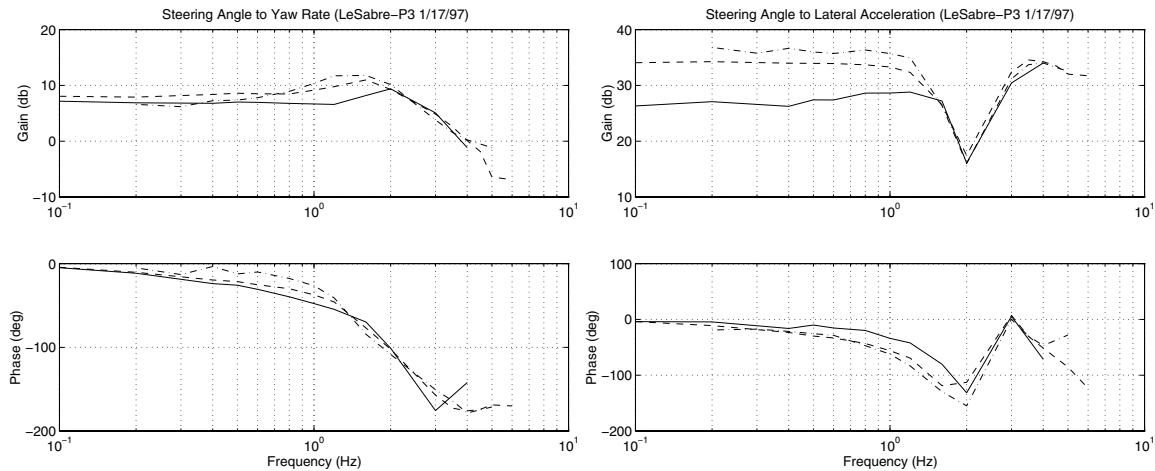

Figure 1: Experimental results [Velocities: $10(-)$, $20(- -)$, $30(- . -)m/s$ $(22, 45, 67mph)$]
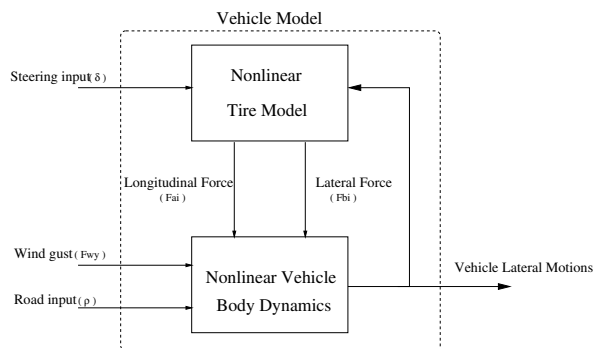
3   Vehicle Model

3.1   Nonlinear 3 DOF Vehicle Model

Figure 2: Structure of the nonlinear vehicle model

4

The lateral vehicle model can be schematically represented as in Fig. 2 with two major components: the tire model and the vehicle body dynamics. The external inputs to the vehicle model include steering angle (δ), wind gust (F_{wy}) and the reference road curvature (ρ). The tire model provides the forces (F_{ai} and F_{bi}) to the vehicle lateral body dynamics. These forces are determined based on the steering input and the natural feedback from the vehicle lateral motions. The nonlinear vehicle body dynamics and the tire model are discussed individually as following:

- *Nonlinear Vehicle Body Dynamics*

  The dynamics of vehicle has been studied in many literatures with varying complexity. A complex nonlinear model with full 6 DOF has been developed for simulations in [5][17] while a simplified linear 2 DOF bicycle model has been frequently used in the design and analysis of vehicle lateral controllers [5]-[11]. In order to study the influence of the suspension roll dynamics, a nonlinear 3 DOF vehicle model which includes lateral, yaw and roll dynamics, is derived in this section. To focus on the vehicle lateral dynamics, constant forward speed is assumed in this study so that heave and pitch motions are assumed not being excited and are ignored. The schematic diagram of the 3 DOF vehicle model is shown in Fig. 3. This two-axle vehicle model distinguishes the sprung mass m_s

Figure 3: Schematic diagram of 3 DOF vehicle model

from the front and real unsprung masses, m_{uf} and m_{ur}, with their own mass centers. The sprung mass interacts with the front and rear unsprung masses via the front and rear

5

suspensions. The roll centers, RC_f and RC_r, for both front and rear suspension systems are defined as the points subjecting to a pure roll moment. The roll axis is defined as the line connecting the roll centers of the front and rear suspensions as shown in Fig. 3. The roll axis is not parallel to the ground due to the different front and rear roll center heights, h_f and h_r. The dynamic equations of motion in terms of lateral y, roll ϕ and yaw ε directions can be derived by the Newtonian method as:

$$M(\ddot{y} + V\dot{\varepsilon}) - m_s h_{m_s} \ddot{\phi} \cos\phi + m_s h_{m_s} \dot{\phi}^2 \sin\phi + m_s d_{m_s} \ddot{\varepsilon} =$$
$$F_{b1} + F_{b2} + F_{b3} + F_{b4} + F_{wy} \quad (1)$$

$$I_{x_s} \ddot{\phi} - m_s (\ddot{y} + V\dot{\varepsilon}) h_{ms} \cos\phi - m_s h_{m_s} d_{m_s} \ddot{\varepsilon} \cos\phi =$$
$$m_s g h_{m_s} \sin\phi \cos\theta - (K_1 + K_2)\phi - (D_1 + D_2)\dot{\phi} \quad (2)$$

$$I_z \ddot{\varepsilon} + m_s d_{m_s} (\ddot{y} + V\dot{\varepsilon}) + m_s h_{m_s} d_{m_s} \dot{\phi}^2 \sin\phi - m_s h_{m_s} d_{m_s} \ddot{\phi} \cos\phi =$$
$$l_1 (F_{b_1} + F_{b_2}) - l_2 (F_{b_3} + F_{b_4}) - \frac{S_b}{2}(F_{a_1} + F_{a_3}) + \frac{S_b}{2}(F_{a_2} + F_{a_4}) \quad (3)$$

The derivation of the dynamic equations can be found in the Appendix. Variables and parameters in these and subsequent equations are defined in Table 1 and nomenclature is at the end of paper. Specifically, h_{m_s} is the distance between the CG of the sprung mass m_s and the roll axis. d_{m_s} is the horizontal distance between the sprung mass CG and the vehicle CG as shown in Fig. 16 in the Appendix. K_i and D_i ($i = 1, 2$) are the rotational spring and damper coefficients calculated from the respective coefficients of the front and real suspension springs and shock obsorbers. For simplicity, the wind gust F_{wy} is assumed to act on the vehicle's CG only. F_{ai} and F_{bi} are the forces acting on the ith tire along the longitudinal and lateral directions. They can be represented in terms of the forces along and perpendicular to the tire orientation, F_{xi} and F_{yi}, respectively at each wheel:

$$\begin{aligned} F_{ai} &= F_{xi} \cos\delta_i - F_{yi} \sin\delta_i \\ F_{bi} &= F_{xi} \sin\delta_i + F_{yi} \cos\delta_i \end{aligned} \quad (4)$$

For i=1, 2, 3 and 4. This force transformation is convenient to relate the vehicle body dynamics to the forces generated from the tire model.

- *Nonlinear Tire Model*

The nonlinear tire model is used to provide both the longitudinal and lateral forces with

6

respect to the tire orientation. The longitudinal tire forces can be written as $F_{x_1} = F_{x_2} = F_x$ and $F_{x_3} = F_{x_4} = 0$ since the driving thrust is assumed fixed for maintaining constant speed and is equally split between the two front wheels for simplicity. The nonlinear characteristics for the lateral tire force is obtained by applying the Bakker's empirical relation [20][21] as

$$F_{yi}^{Bakk} = g(\alpha_i, F_{zi}) \qquad \text{For i=1, 2, 3, 4} \qquad (5)$$

where the lateral tire force F_{yi}^{Bakk} is a nonlinear function of the slip angle α_i and the vertical froce F_{zi}. For front-wheel-steered vehicles, the steering angle can be assumed as $\delta_1 = \delta_2 = \delta$, $\delta_3 = \delta_4 = 0$. The slip angle α_i of the ith wheel can be determined by:

$$
\begin{aligned}
\alpha_1 &= \delta - \tan^{-1} \frac{\dot{y} + l_1 \dot{\varepsilon}}{V - \frac{S_b}{2}\dot{\varepsilon}} - \kappa_1 \phi &\qquad \alpha_2 &= \delta - \tan^{-1} \frac{\dot{y} + l_1 \dot{\varepsilon}}{V + \frac{S_b}{2}\dot{\varepsilon}} - \kappa_1 \phi \\
\alpha_3 &= -\tan^{-1} \frac{\dot{y} - l_2 \dot{\varepsilon}}{V - \frac{S_b}{2}\dot{\varepsilon}} - \kappa_2 \phi &\qquad \alpha_4 &= -\tan^{-1} \frac{\dot{y} - l_2 \dot{\varepsilon}}{V + \frac{S_b}{2}\dot{\varepsilon}} - \kappa_2 \phi \qquad (6)
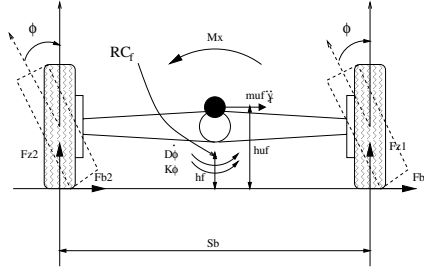\end{aligned}
$$

Figure 4: Schematic diagram of the front axle and the camber angle of the wheel assembly

where κ_1 and κ_2 are the front and rear roll steer coefficients. The roll steer is defined as the steering motion of the front and rear wheels induced by the rolling motion of the sprung mass [18]. Due to the cornering of the vehicle, the lateral load transfer is considered. The vertical force on each tire is the sum of the static load and the lateral load transfer which can be represented as:

$$
\begin{aligned}
F_{z1} &= M_1 - \Delta F_{zf}, &\qquad F_{z2} &= M_1 + \Delta F_{zf} \\
F_{z3} &= M_2 - \Delta F_{zr}, &\qquad F_{z4} &= M_2 + \Delta F_{zr} \qquad (7)
\end{aligned}
$$

where M_1 and M_2 are the gravitational forces composed of the effect of the sprung and unsprung masses:

$$M_1 = \frac{m_{uf}g}{2} + \frac{m_s g l_2}{2(l_1 + l_2)}$$

7

$$M_2 = \frac{m_{ur}g}{2} + \frac{m_s g l_1}{2(l_1 + l_2)} \tag{8}$$

The lateral load transfer can be obtained by considering the forces and moments acting on the front axle of the vehicle as shown in Fig. 4. The load transfer at the front axle ΔF_{zf} is determined by taking moment balance about the front roll center (RC_f):

$$\Delta F_{zf} = \frac{1}{S_b}[h_f(F_{b1} + F_{b2}) + K_1\phi + D_1\dot{\phi} - m_{uf}(\ddot{y} + V\dot{\varepsilon})(h_{uf} - h_f)] \tag{9}$$

where $K_1\phi$ is the moment from the front suspension spring and $D_1\dot{\phi}$ represents the moment created by the front shock obsorber. Similarly, the load transfer at the rear axle is obtained as:

$$\Delta F_{zr} = \frac{1}{S_b}[h_r(F_{b3} + F_{b4}) + K_2\phi + D_2\dot{\phi} - m_{ur}(\ddot{y} + V\dot{\varepsilon})(h_{ur} - h_r)] \tag{10}$$

Cambered tires are considered for completeness as in [19]. The camber thrust is assumed as function of the suspension roll angle ϕ. The total lateral force of a cambered tire is the sum of the cornering force and the camber thrust which can be extended from Eq.(5) as:

$$F_{yi} = f_i(\delta, \dot{y}, \dot{\varepsilon}, \phi, F_{zi}) \qquad \text{For i = 1, 2, 3, 4} \tag{11}$$

Eq.(11) describes the lateral tire force as a nonlinear function of the steering input, vehicle lateral dynamics and the vertical force.

3.2 Linear 3 DOF Vehicle Model

With small angle assumption, a linear 3 DOF vehicle model is developed in this section to perform vehicle model validation and linear analysis. The dynamic equations of the vehicle model are transformed from the local frame fixed on the principal axes of the vehicle (X, Y) to the road reference frame (X_r, Y_r). The road reference frame is attached to the road center at a point adjacent to the vehicle CG with X_r axis tangent to the road trajectory and moves along the road with the same speed as the vehicle. The vehicle model with respect to the road reference frame is convenient for obtaining the local sensor information. For small angle assumption, the yaw rate induced by the road curvature can be approximated as $\dot{\varepsilon}_d \cong V\rho$, where ρ is the radius of road curvature. The reference vehicle lateral acceleration at CG $(\ddot{y}_r)$ and the reference yaw rate $(\dot{\varepsilon}_r)$ can be obtained by:

$$\ddot{y}_r \cong \ddot{y} + V\dot{\varepsilon} - V^2\rho, \qquad \dot{\varepsilon}_r \cong \dot{\varepsilon} - V\rho \tag{12}$$

8

A linear 3 DOF vehicle model is simplified by assuming small roll angle such that $\dot{\phi}^2 \to 0$, $\sin\phi \cong \phi$ and $\cos\phi \cong 1$. In this paper, the horizontal distance between the vehicle CG and the CG of the sprung mass (d_{m_s}) is assumed zero for simplicity. The resultant equations of the linear vehicle body dynamics can be obtained from Eqs. (1)-(3) as:

$$M\ddot{y}_r - m_s h_{m_s}\ddot{\phi} = F_{b1} + F_{b2} + F_{b3} + F_{b4} + F_{wy} - MV^2\rho \tag{13}$$

$$I_{x_s}\ddot{\phi} - m_s h_{m_s}\ddot{y}_r = (m_s g h_{m_s}\cos\theta - K_1 - K_2)\phi - (D_1 + D_2)\dot{\phi} + m_s h_{m_s}V^2\rho \tag{14}$$

$$I_z\ddot{\varepsilon}_r = l_1(F_{b_1} + F_{b_2}) - l_2(F_{b_3} + F_{b_4}) - \frac{S_b}{2}(F_{a_1} + F_{a_3}) + \frac{S_b}{2}(F_{a_2} + F_{a_4}) \tag{15}$$

The force transformation between the forces (F_{ai}, F_{bi}) and (F_{xi}, F_{yi}) can be approximated from Eq.(4) as:

$$F_{ai} \cong F_{xi} - F_{yi}\delta_i, \qquad F_{bi} \cong F_{xi}\delta_i + F_{yi} \tag{16}$$

with $\delta_1 = \delta_2 = \delta$, $\delta_3 = \delta_4 = 0$, $F_{x1} = F_{x2} = F_x$ and $F_{x3} = F_{x4} = 0$. The linear slip angle α_i is obtained in terms of the reference vehicle state variables as

$$\alpha_{1,2} = \delta - \frac{1}{V}\dot{y}_r - \frac{l_1}{V}\dot{\varepsilon}_r + \varepsilon_r - \frac{l_1}{V}\dot{\varepsilon}_d - \kappa_1\phi$$

$$\alpha_{3,4} = -\frac{1}{V}\dot{y}_r - \frac{l_2}{V}\dot{\varepsilon}_r + \varepsilon_r - \frac{l_2}{V}\dot{\varepsilon}_d - \kappa_2\phi \tag{17}$$

Again, with small angle assumption, the cornering force is linear related to the slip angle α_i and the camber thrust is also linear with the roll angle ϕ [18]:

$$F_{y_{1,2}} = C_1\alpha_{1,2} + \gamma_1\phi$$

$$F_{y_{3,4}} = C_2\alpha_{3,4} + \gamma_2\phi \tag{18}$$

where C_1 and C_2 are the cornering stiffnesses of the front and rear tires. γ_1 and γ_2 are the respective coefficients from the camber thurst. The structure of the linear 3 DOF vehicle model is shown in Fig. 5. Combining Eqs.(13)-(18), the state-space repersentation $(\dot{\underline{x}} = \mathbf{A}\underline{x} + \mathbf{B}\delta + \underline{d})$ for the linear 3 DOF vehicle model is

$$\frac{d}{dt}\begin{bmatrix} y_r \\ \dot{y}_r \\ \varepsilon_r \\ \dot{\varepsilon}_r \\ \phi \\ \dot{\phi} \end{bmatrix} = \begin{bmatrix} 0 & 1 & 0 & 0 & 0 & 0 \\ 0 & \frac{A_1\Lambda_1}{V} & -A_1\Lambda_1 & \frac{A_2\Lambda_1}{V} & R_1 & R_2 \\ 0 & 0 & 0 & 1 & 0 & 0 \\ 0 & \frac{A_3}{V} & -A_3 & \frac{A_4}{V} & R_3 & 0 \\ 0 & 0 & 0 & 0 & 0 & 1 \\ 0 & \frac{A_1\Lambda_2}{V} & -A_1\Lambda_2 & \frac{A_2\Lambda_2}{V} & R_4 & R_5 \end{bmatrix}\begin{bmatrix} y_r \\ \dot{y}_r \\ \varepsilon_r \\ \dot{\varepsilon}_r \\ \phi \\ \dot{\phi} \end{bmatrix} + \begin{bmatrix} 0 \\ B_1\Lambda_1 \\ 0 \\ B_2 \\ 0 \\ B_1\Lambda_2 \end{bmatrix}\delta + \begin{bmatrix} 0 \\ d_1 \\ 0 \\ d_2 \\ 0 \\ d_3 \end{bmatrix} \tag{19}$$
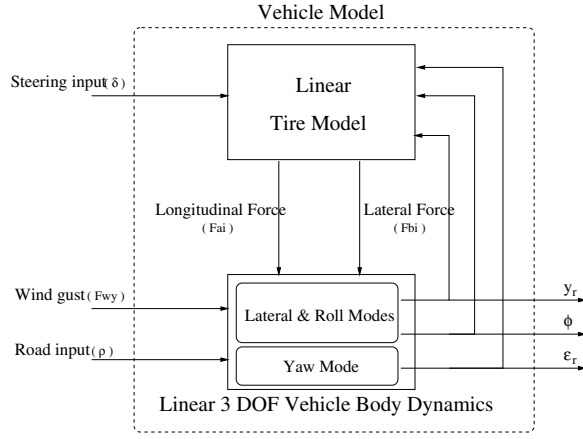
9

Figure 5: Structure of the linear vehicle model

where

$$A_1 = -\frac{2(C_1 + C_2)}{M}, \qquad A_2 = \frac{2(-l_1 C_1 + l_2 C_2)}{M}$$

$$A_3 = \frac{2(-l_1 C_1 + l_2 C_2)}{I_z}, \qquad A_4 = -\frac{2(l_1^2 C_1 + l_2^2 C_2)}{I_z}$$

$$\Lambda_1 = \frac{M I_{x_s}}{M I_{x_s} - m_s^2 h_{m_s}^2}, \qquad \Lambda_2 = \frac{M m_s h_{m_s}}{M I_{x_s} - m_s^2 h_{m_s}^2}$$

$$R_1 = \frac{2(\gamma_1 + \gamma_2) I_{x_s} + m_s h_{m_s}(m_s g h_{m_s} - K_1 - K_2)}{M I_{x_s} - m_s^2 h_{m_s}^2}, \qquad R_2 = \frac{-m_s h_{m_s}(D_1 + D_2)}{M I_{x_s} - m_s^2 h_{m_s}^2}$$

$$R_3 = \frac{2(\gamma_1 l_1 - \gamma_2 l_2)}{I_z}, \qquad R_4 = \frac{2 m_s h_{m_s}(\gamma_1 + \gamma_2) + M(m_s g h_{m_s} - K_1 - K_2)}{M I_{x_s} - m_s^2 h_{m_s}^2}$$

$$R_5 = \frac{-M(D_1 + D_2)}{M I_{x_s} - m_s^2 h_{m_s}^2}, \qquad B_1 = \frac{2(C_1 + F_x)}{M}$$

$$B_2 = \frac{2 l_1 C_1 (F_x + C_1)}{I_z}, \qquad d_1 = \frac{\Lambda_1}{M} F_{wy} + \frac{A_2 \Lambda_1}{V} \dot{\varepsilon}_d - V^2 \rho$$

$$d_2 = -\frac{2(l_1^2 C_1 + l_2^2 C_2)}{I_z V} \dot{\varepsilon}_d, \qquad d_3 = \frac{\Lambda_2}{M} F_{wy} + \frac{A_2 \Lambda_2}{V} \dot{\varepsilon}_d - 2 \Lambda_2 V^2 \rho$$

The nonlinear 3 DOF vehicle model (Eqs.(1)-(11)) will be used for simulations and the linear 3 DOF model (Eq.(19)) will be utilized for model validation and linear analysis.

4   Vehicle Model Validation

Both the linear 3 DOF vehicle model (Eq.(19)) and the bicycle model are used to validate with the test data. A typical bicycle model can either be obtained from the derivation in [5] or from Eq.(19) by eliminating the roll state variable ϕ by letting the CG of the sprung mass passing through the roll axis ($h_{m_s} = 0$) as will be further explained in the next section. One way to compare the difference between these two models is to observe the model behaviors both at steady-state and at high frequencies. By transforming the state-space equation of the 3 DOF

10

vehicle model and the bicycle model to their transfer functions ($\underline{y} = [\mathbf{C}(sI - \mathbf{A})^{-1}\mathbf{B}]\delta$), the steady-state gain from steering angle to yaw rate and that from steering angle to the lateral acceleration at the sensor location can be obtained by:

$$\left.\frac{\dot{\varepsilon}_r}{\delta}\right|_{w=0} = \frac{V}{(l_1 + l_2) + K_{us}V^2/g} \tag{20}$$

$$\left.\frac{\ddot{y}_s}{\delta}\right|_{w=0} = \frac{V^2}{(l_1 + l_2) + K_{us}V^2/g} \tag{21}$$

where

$$K_{us} = K_{slip} = \frac{Mg}{l_1 + l_2}\left(\frac{l_2}{2C_1} - \frac{l_1}{2C_2}\right) \qquad \text{For bicycle model}$$

$$K_{us} = K_{slip} + K_{camber+roll} \qquad \text{For 3 DOF model}$$

$$= \frac{Mg}{l_1 + l_2}\left(\frac{l_2}{2C_1} - \frac{l_1}{2C_2}\right) + \frac{m_s g h_{ms}}{K_1 + K_2 - m_s g h_{ms}}\left(\frac{\gamma_1}{C_1} - \frac{\gamma_2}{C_2} - \kappa_1 + \kappa_2\right)$$

$\dot{\varepsilon}_r$ is the yaw rate of the vehicle which is measured by the yaw rate sensor. $\ddot{y}_s$ is the lateral acceleration at the sensor location which is measured by the accelerometer ($\ddot{y}_s = \ddot{y}_r + d_s\ddot{\epsilon}_r + h_s\ddot{\phi}$) as shown in Fig. 16. K_{slip} is the understeer coefficient derived from the effect of the slip angle and $K_{camber+roll}$ is the additional effect from the camber angle and roll steer. The steady-state responses from steering angle to yaw rate and lateral acceleration with respect to different velocities for both models are shown in Fig. 6. It can be seen that the 3 DOF model ($K_{us} = 0.1173$) can match better with the test data comparing with the bicycle model ($K_{us} = 0.1080$). The 3 DOF vehicle model shares the same bicycle model parameters as shown in Table 1. However, both the camber thrust and roll steer provide higher understeer coefficient (K_{us}) for the 3 DOF model. $\gamma_1 = \gamma_2 = 1000$, $\kappa_1 = 0.01$ and $\kappa_2 = 0.03$ are chosen to reflect the influence from the roll dynamics to the steady-state responses. However, the effect from the roll steer and the camber thrust is comparably smaller than that from the slip angle for nominal driving situation under the linear assumption. In general, the steady-state responses for both the 3 DOF model and the bicycle model is similar.

In order to match the vehicle model with the test data in higher frequencies, the response from steering angle to the lateral acceleration at $w = \infty$ can be obtained from the model transfer function:

$$\left.\frac{\ddot{y}_s}{\delta}\right|_{w=\infty} = \frac{2C_1}{M - \frac{m_s h_{ms}^2}{I_{x_s}}}\left(1 + h_s\frac{m_s h_{ms}}{I_{x_s}}\right) + d_s\frac{2C_1 l_1}{I_z} \qquad \text{For 3 DOF model} \tag{22}$$

$$\left.\frac{\ddot{y}_s}{\delta}\right|_{w=\infty} = \frac{2C_1}{M} + d_s\frac{2C_1 l_1}{I_z} \qquad \text{For bicycle model} \tag{23}$$
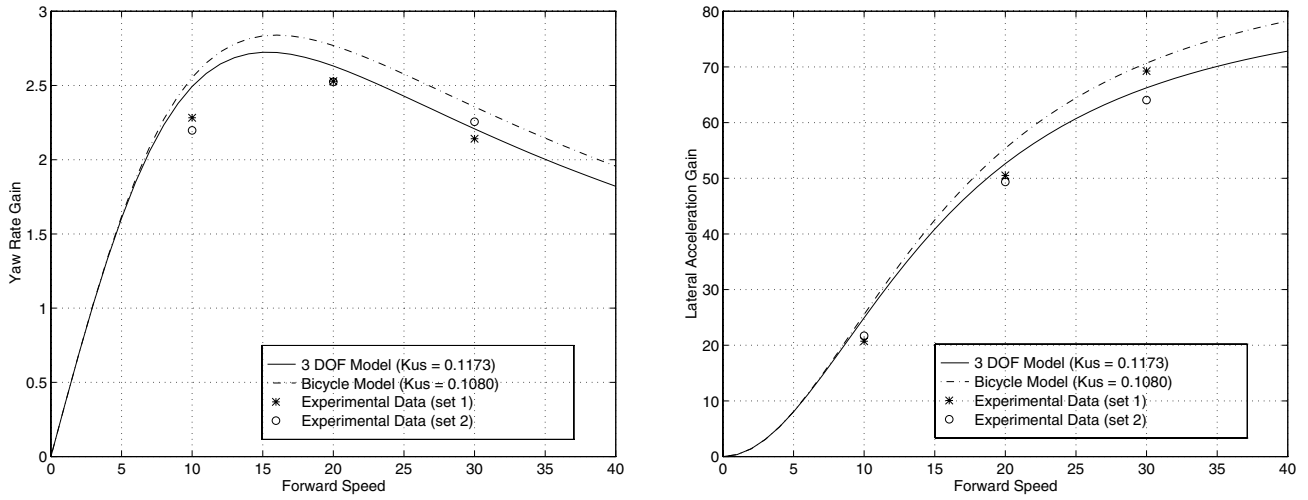
11

Figure 6: Steady-state response from steering angle to yaw rate and lateral acceleration

The major difference between the 3 DOF model and the bicycle model is created by h_{m_s}, the distance between the sprung mass CG and the roll axis. As shown in Eqs.(22) and (23), the characteristics of the 3 DOF model and the bicycle model at higher frequencies can be tuned by properly choosing the sensor location (d_s and/or h_s) while other vehicle parameters remain fixed. The 3 DOF model have an extra parameter, h_s, comparing with the bicycle model, which provides one more degree of freedom to match the test data in higher frequencies. Finally, the notch behavior in the lateral acceleration response can be matched with the test data by selecting the suspension constants K_i and damper coefficients D_i in the 3 DOF model. After matching the model transfer function with the test responses as in the above procedures, the open loop transfer functions from steering angle to yaw rate and lateral acceleration of both
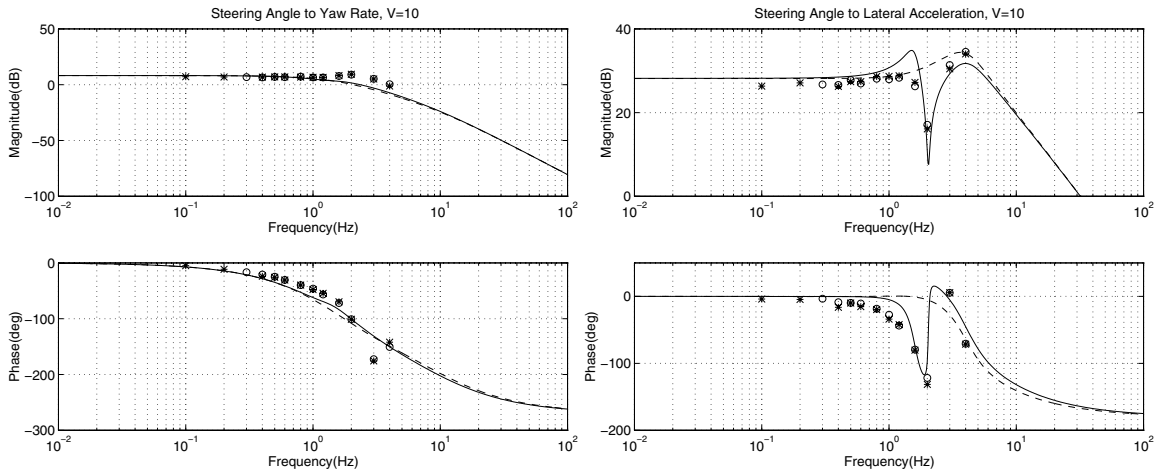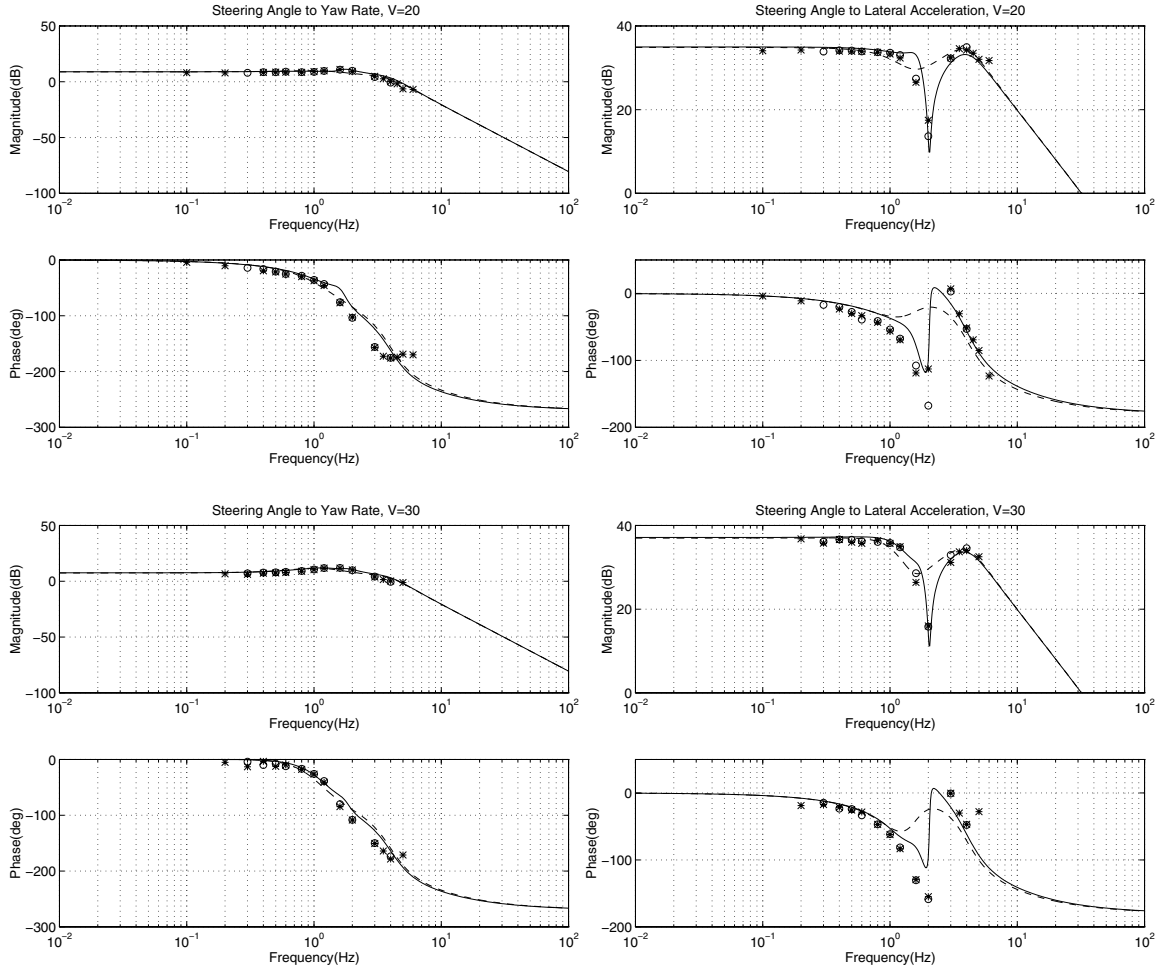
Figure 7: Frequency responses from steering angle to yaw rate and lateral acceleration with V=10, 20, $30m/sec$ [Two sets of experimental data(∗,∘), 3 DOF model(-), 2 DOF model(- -)]

the 3 DOF model and the bicycle model are as shown in Fig. 7. A third order transfer function with a natural frequency $\omega_n = 5Hz$, a damping ratio $\xi = 0.4$ and $\omega_1 = 10Hz$ is obtained via model identification using steering command and wheel angle, and is verified in [11] as the dynamics of steering actuator:

$$A(s) = \frac{\omega_n^2\,\omega_1}{(s^2 + 2\xi\omega_n s + \omega_n^2)(s + \omega_1)}$$

The introduction of the steering actuator is necessary since the suspension frequency in question is close to that of the actuator bandwidth. It can be seen that both the 3 DOF model and the bicycle model match the test responses up to about $0.9Hz$ for yaw rate and lateral acceleration responses. However, only the 3 DOF model has the extra degree of freedom to match the notch behavior of the test data centered around $2Hz$ where the roll suspension

13

has its natural frequency. Moreover, the additional actuator dynamics is recognizagble for the roll off effect at frequencies higher than $4Hz$ as shown in Fig. 7. Both the 3 DOF and bicycle models reproduce the low frequency vehicle behavior reasonably well while only the 3 DOF model has higher fidelity about the suspension mode frequency due to its inclusion of the suspension roll mode.

5   Analysis of the Coupling Effect between the Roll and Lateral Modes

The main purpose of this paper is to study the importance of the roll dynamics to the response of vehicle steering. As shown in the structure of the nonlinear vehicle model in Fig. 2, the vehicle body dynamics, y, ε and ϕ, have coupling effect with each other as can be seen in Eqs. (1)-(3). On the other hand, if one assumes that the CG of the sprung mass and the vehicle's CG share the same horizontal position ($d_{m_s} = 0$), the yaw dynamics is decoupled from the lateral and roll dynamics inside the vehicle body dynamics as shown in Eqs.(13)-(15). This is a reasonable assumption from a practical stand point since the values of m_s and M are usually very close, and the test data support this assumption as shown in previous section. The main coupling effect for yaw dynamics with the lateral and roll dynamics thus comes from the tire model as shown in Fig. 5. This coupling between the roll dynamics and the lateral dynamics provides the notch behavior around the suspension frequencies in the lateral acceleration characteristics. Furthermore, Eq.(19) suggests that the degree of coupling depends heavily on the following two factors: the distance between the sprung mass CG and the roll axis (h_{m_s}), as well as the suspension coefficients (K_i and D_i). Fig. 8 illustrates the coupling effects from h_{m_s} and K_i to the frequency characteristics of the lateral acceleration based on the 3 DOF linear vehicle model. It can be seen from the left figure of Fig. 8 that the response of the 3 DOF vehicle model becomes the same as that of the bicycle model as $h_{m_s} \to 0$. This can also be verified by taking $h_{m_s} = 0$ in Eq.(19). In fact, no roll motion is created by the tires when the roll axis passes through the CG of the sprung mass. From the right figure of Fig. 8, the 3 DOF model and the bicycle model are virtually the same when the suspension stiffness approaches infinity ($K_i \to \infty$). In reality, there always exists some coupling in the lateral dynamics from the roll dynamics since it is difficult to guarantee that

14

the roll axis will pass through the sprung mass CG $(h_{m_s} \neq 0)$ and the suspension stiffness does not goes to infinity $(K_i \neq \infty)$.
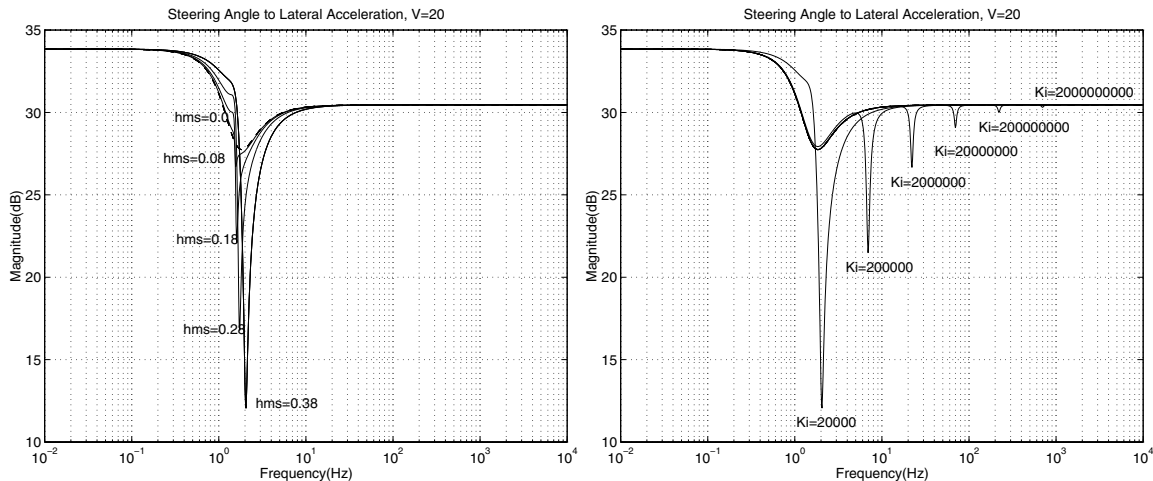

Figure 8: Frequency responses from steering input to the lateral acceleration with the effect of different h_{m_s} (left) and suspension constant K_i (right).

In order to investigate the effect of roll coupling to vehicle steering control, the establishment of a fair comparison between the 3 DOF model and the bicycle model is desirable. Vehicle parameters are chosen so that the frequency responses of these two models are virtually the same except at around the frequency of roll coupling. As shown in Eqs.(22) and (23), various sensor location (h_s) creates different characteristics between the 3 DOF model and the bicycle model in the high frequency range. Based on Eqs. (22) and (23), one can choose to place the sensor at the location where h_s equals to

$$h_s = -\frac{m_s h_{m_s}}{M} \tag{24}$$

With this choice of h_s, the 3 DOF vehicle model and the bicycle model would have the same freqnency responses except around the suspension frequencies as shown in Fig. 8. In next section, controllers will be designed based on these two models. The results will be used to evaluate the potential impact to the steering control due to the suspension roll coupling.

15

6 Controller Design with and without the Effect of Roll Dynamics

The μ-synthesis and H_∞ optimization [22][23] are used in this paper to obtain "equivalent" robust controllers based on the two vehicle models, the 3 DOF linear model and the bicycle model, developed with and without the suspension roll dynamics. These two controllers will be designed based on the identical performance indexes with the same synthesis. Since the two vehicle models differ from each other only in the area of roll coupling, a fair comparison is therefore established. Performance of these two controllers will then be evaluated to investigate the effect of the roll dynamics. Consider the uncertainties due to the variation of the cornering stiffness as

$$C_1 = \bar{C}_1(1 + \delta_{u1}), \quad C_2 = \bar{C}_2(1 + \delta_{u2})$$

where $\bar{C}_1$ and $\bar{C}_2$ represent the nominal values of the cornering stiffness. δ_{u1} and δ_{u2} are multiplicative uncertainties of the front and rear cornering stiffnesses. Due to the linear relation of the cornering stiffness to the state-space equations of the model, the uncertain state-space model can be constructed with parameter variations as a Linear Fractional Transformation (LFT) as follows [23]:

$$\begin{bmatrix} \dot{\underline{x}}(t) \\ \underline{y}(t) \end{bmatrix} = \left(\begin{bmatrix} \mathbf{A} & \mathbf{B} \\ \mathbf{C} & \mathbf{D} \end{bmatrix} + \sum_{i=1}^{2} \delta_{ui} \begin{bmatrix} \mathbf{A_i} & \mathbf{B_i} \\ \mathbf{C_i} & \mathbf{D_i} \end{bmatrix} \right) \begin{bmatrix} \underline{x}(t) \\ u(t) \end{bmatrix} \tag{25}$$

where $\mathbf{A}$, $\mathbf{B}$, $\mathbf{C}$ and $\mathbf{D}$ are the nominal coefficient matrices and $\mathbf{A_i}$, $\mathbf{B_i}$, $\mathbf{C_i}$ and $\mathbf{D_i}$ are the uncertain coefficient matrices. The input u of the system in Eq.(25) is the front wheel steering angle δ. From the available sensor measurements in the experimental vehicle, the lateral displacements under both the front and rear bumpers, y_f and y_b, can be obtained as the measurable outputs ($\underline{y} = [y_f \ y_b]^T$) for controller design:

$$y_f = y_r + d_f \varepsilon_r + h_s \phi, \qquad y_b = y_r + d_b \varepsilon_r + h_s \phi \qquad \text{For 3 DOF model} \tag{26}$$

$$y_f = y_r + d_f \varepsilon_r, \qquad y_b = y_r + d_b \varepsilon_r \qquad \text{For bicycle model} \tag{27}$$

Assuming that r_i is the rank of uncertainty LFT matrix, the uncertain coefficient matrices can be factorized as

$$\begin{bmatrix} \mathbf{A_i} & \mathbf{B_i} \\ \mathbf{C_i} & \mathbf{D_i} \end{bmatrix} = \begin{bmatrix} \mathbf{E_i} \\ \mathbf{F_i} \end{bmatrix} \begin{bmatrix} \mathbf{G_i} & \mathbf{H_i} \end{bmatrix} \qquad \text{For } i = 1, 2 \tag{28}$$

16

with $[\ \mathbf{E_i}\ \ \mathbf{F_i}\ ]^T \in R^{r_i \times (n+n_y)}$ and $[\ \mathbf{G_i}\ \ \mathbf{H_i}\ ] \in R^{r_i \times (n+n_u)}$ (n: the number of states, n_u: the number of inputs, n_y: the number of outputs).

Therefore, the LFT form of the extended plant $\mathbf{G_{ss}}$, which includes the parameter uncertainties δ_{u1} and δ_{u2}, can be expressed as:

$$
\begin{bmatrix} \dot{\underline{x}}(t) \\ \underline{y}(t) \\ \underline{w}_1(t) \\ \underline{w}_2(t) \end{bmatrix} = \begin{bmatrix} \mathbf{A} & \mathbf{B} & \mathbf{E_1} & \mathbf{E_2} \\ \mathbf{C} & \mathbf{D} & \mathbf{F_1} & \mathbf{F_2} \\ \mathbf{G_1} & \mathbf{H_1} & 0 & 0 \\ \mathbf{G_2} & \mathbf{H_2} & 0 & 0 \end{bmatrix} \begin{bmatrix} \underline{x}(t) \\ u(t) \\ \underline{z}_1(t) \\ \underline{z}_2(t) \end{bmatrix} \tag{29}
$$

where $[\underline{z}_1(t)\ \underline{z}_2(t)]^T$ is the input vector from the parameter uncertainty δ_{u1} and δ_{u2} to the extended plant, and $[\underline{w}_1(t)\ \underline{w}_2(t)]^T$ is the output vector from the extended plant to δ_{u1} and δ_{u2}. The controlled system, which includes unmodeled dynamics, parameter variations and
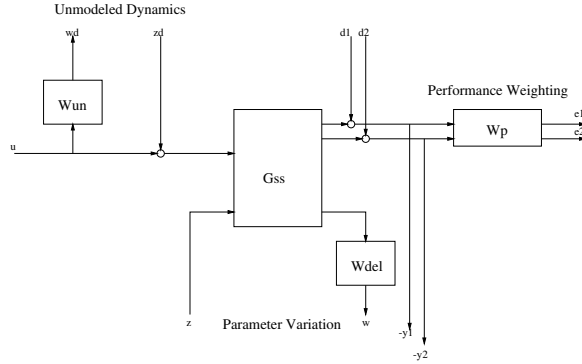
Figure 9: The controlled system with weighting functions

disturbances, can be established with proper selection of weighting functions as in Fig. 9. Assuming that there are 40% uncertainty at low frequencies and 100% above 2 Hz. The weighting function for parameter uncertainties W_{del} and unmodeled dynamics W_{un} are chosen as in Fig. 10:

$$
W_{del} = W_{un} = \frac{(s+2)}{(s+20)} \tag{30}
$$

the performance weighting function W_p is selected for y_f and y_b by assuming that the steady-state tracking error should remain within $\pm 25\%$. The frequency range around 1-2 Hz is also weighted by W_p to effectly penalize the suspension roll mode. W_p is chosen as:

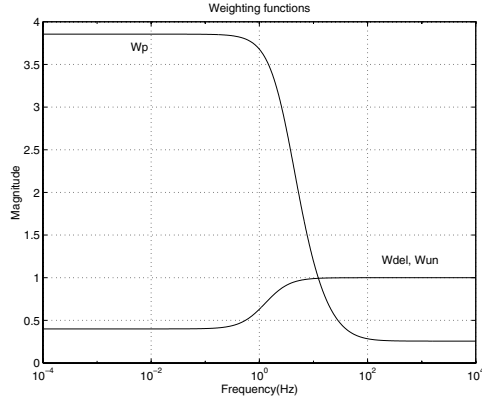$$
W_p = \frac{2.57(s+300)}{(10s+200)} \tag{31}
$$

17

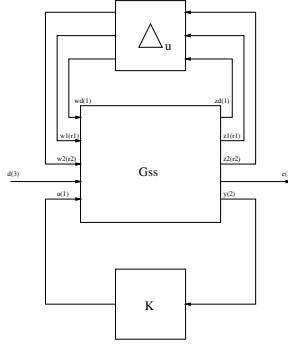Figure 10: The weighting functions for controller design

Figure 11: The closed-loop interconnection of the extended plant

The overall closed-loop interconnection, including the extended plant $\mathbf{G}_{ss}$, unmodeled dynamics, parameter variation and controller $\mathbf{K}$, can be shown in Fig. 11. Δ_u is the uncertain matrix which belongs to the set: $\boldsymbol{\Delta} = \{diag[\delta_{u1}I_{r1}, \ \delta_{u2}I_{r2}, \ \delta_{u3}I_1] : \ \delta_{ui} \in R, \ |\delta_{ui}| < \tau\}$ where δ_{u3} represents the uncertainty of the unmodeled dynamics and τ is the bound of the multiplicative uncertainty. The criterion of the controller design can be formulated as:

- Robust stability: The stability of the closed-loop system is guaranteed for all $\Delta_u \in \boldsymbol{\Delta}$ with τ large enough.

- Robust performance: Under the requirement of robust stability, the maximum gain from the disturbance to the error output is less than a prescribed value: $\| T_{\underline{d} \to \underline{e}} \|_\infty \leq \gamma$.

The diagonal structure of the uncertainty provides the design problem naturally fitting with the μ synthesis framework [23]. By introducing a fictitious uncertainty block Δ_f between the error output and disturbance input, the design problem can be reformulated as in Fig. 12 with $\Delta_p \in \boldsymbol{\Delta_p} = \{diag[\Delta, \ \Delta_f] : \ \Delta \in \boldsymbol{\Delta}, \ \Delta_f \in C^{2 \times 2}\}$. The objective of the μ synthesis is to find
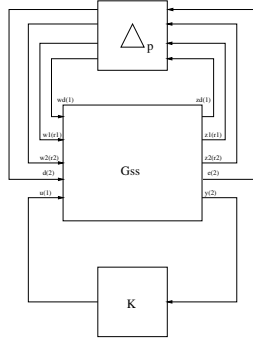
18

Figure 12: Reformulation of the closed-loop interconnection using μ-synthesis framework

a controller $\mathbf{K}$ such that

$$\sup_{w \in R} \mu_{\mathbf{\Delta_p}}(T_{\underline{w} \to \underline{z}}(jw)) \leq \gamma \tag{32}$$

where $\underline{w} = [\underline{w}_1 \ \underline{w}_2 \ w_d \ \underline{d}]^T$ and $\underline{z} = [\underline{z}_1 \ \underline{z}_2 \ z_d \ \underline{e}]^T$. $\mu_{\mathbf{\Delta_p}}(\cdot)$ is the structure singular as defined in [23]. If the Eq.(32) is satisfied, the following conditions can be guaranteed:

- Robust stability: For all $\Delta \in \mathbf{\Delta}$ with $\parallel \Delta \parallel_\infty < \gamma^{-1}$, the closed loop system is well-posed and internally stable.

- Robust performance: $\parallel T_{\underline{d} \to \underline{e}} \parallel_\infty \leq \gamma$ for all $\Delta \in \mathbf{\Delta}$ with $\parallel \Delta \parallel_\infty < \gamma^{-1}$.

Since the synthesis (Eq.(32)) is not directly solvable, an alternative approach is to solve the problem by using the D-K iteration [24]. Solution to Eq.(32) can be approximated by solving

$$\parallel \mathbf{D} T_{\underline{w} \to \underline{z}}(jw) \mathbf{D}^{-1} \parallel_\infty \leq \gamma \tag{33}$$

where $\mathbf{D}$ is a stable and minimum phase scaling matrix which satisfies $\mathbf{D}\Delta = \Delta \mathbf{D}$. The D-K iteration algorithm proceeds by performing minimization of Eq.(33) over $\mathbf{D}$ and $\mathbf{K}$: when $\mathbf{K}$ is fixed, the convex optimization problem has to be solved for the scaling matrix $\mathbf{D}$; when $\mathbf{D}$ is fixed, the standard H_∞ optimization problem is conducted to find the controller $\mathbf{K}$. The iteration terminate when the prespecified performance index γ is reached. The technique is used to find the suboptimal controller for both the 3 DOF model and the bicycle model. These two controllers will then be applied to the same nonlinear 3 DOF vehicle model for comparison.
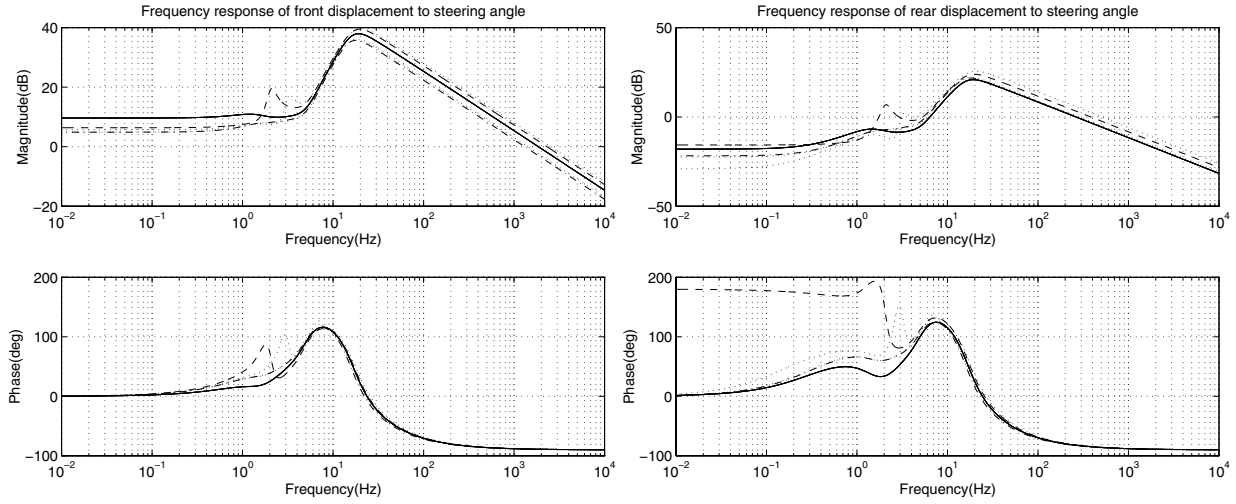
Figure 13: Frequency responses of controllers at front and rear sensor inputs [Bicycle model(-); 3 DOF model: K_i=20000(- -), K_i=40000($\cdot$), $K_i = 2 \times 10^5$(-.), $K_i = 2 \times 10^{10}$(-..-)]

7 Simulation Results

In this section, two robust controllers using the same weighting functions, one designed based on the 3 DOF model, the other one on the bicycle model are simulated on the same nonlinear 3 DOF model for performance comparison. The simulated maneuvers are defined as first following a straight road and then a curved road with $0.1g$ curvature from t=1 to 9 sec, and finally back to straight road again. A $200Nt$ wind gust happened at t=6 sec is also included. Performance specifications include tracking errors less than 0.2m, actuator bandwidth of $5Hz$, measurement noise of 0.02m and good ride quality. Controllers are designed by D-K iteration for both models under different velocities as discussed in the previous section. The frequency responses of the two controllers are shown in Fig. 13 at V = $20m/s$. From Fig. 13, different controller characteristics can be observed around the suspension frequency. In order to study the different closed-loop performance from the controller design by the 3 DOF model and the bicycle model, two simulation cases are shown for comparison:

- Controller designed by the bicycle model is applied on several nonlinear 3 DOF vehicle models with different suspension stiffness as shown in Fig. 14.

- Controller designed by the 3 DOF model with soft suspension ($K_i = 20000$) is applied on the same nonlinear 3 DOF vehicle models with different suspension stiffness as shown in Fig. 15.

20% parameter variation of the cornering stiffness is considered in both cases to also examine the robustness. It can be seen that both controllers provide similar responses for model with stiff suspension. It is interesting to note that the controller designed based on a 3 DOF model with soft suspension exhibits similar performance to that from a bicycle model even when the suspension turns out to be very stiff. The closed-loop responses with the controller designed by the bicycle model could become unstable as the suspension becomes "too" soft, while the 3 DOF controller still satisfies the performance criterion. Since the 3 DOF controller considers the suspension mode at the design stage, it provide better stability and performance than the bicycle model controller. Moreover, these simulation results examplify the potential detrimental coupling effect of the roll dyanmics to the vehicle steering control.

Figure 14: Closed-loop time responses for bicycle controller with V=20m/sec and 20% parameter uncertainty [$K_i = 20000(\cdot)$, K_i=40000(- -), $K_i = 2 \times 10^5$(-.),$K_i = 2 \times 10^{10}$(-)]

8 Conclusion

The advantage of considering the roll dynamics in steering control was addressed in this paper, especially for vehicles with soft suspension systems. The nonlinear 3 DOF vehicle model was constructed which includes the effects from the roll dynamics to the lateral motions. The developed linear 3 DOF vehicle model was verified against the experimental data. The coupling effect between the suspension roll mode and the lateral mode is dominated by the distance from the sprung mass CG to the roll axis as well as the suspension stiffness in the case when such distance is large and the suspension is soft. The steering controller design with the
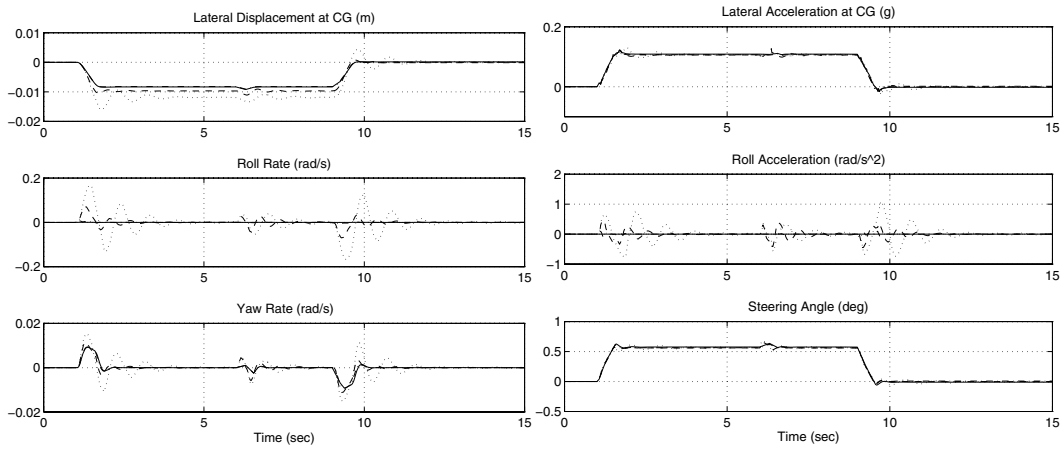
Figure 15: Closed-loop time responses for 3 DOF soft controller ($K_i = 20000$) with V=$20m/sec$ and 20% parameter uncertainty [$K_i = 20000(\cdot)$, K_i=40000(- -), $K_i = 2 \times 10^5$(-.),$K_i = 2 \times 10^{10}$(-)]

bicycle model may excite the suspension mode. The simulation results showed the importance of including roll dynamics in the design of vehicle steering controllers, especially when the suspension is soft. It also provides a good example of the potential influence from the roll coupling to vehicle steering control.

References

[1] P. Varaiya, "Smart Cars on Smart Roads: Problems of Control", *IEEE Trans. on Automatic Control*, AC-38-2, pp. 195-207, 1993.

[2] W. Stevens, "The Automated Highway System Program: A Progress Report", *Proc. of the 13th IFAC World Congrress*, Plenary Volume, San Francisco, California, USA, pp. 25-34, 1996.

[3] S. Tsugwawa, M. Aoki, A. Hosaka and K. Seki, "A Survey of Present IVHS Activities in Japan", *Proc. of the 13th IFAC World Congrress*, Volume Q, San Francisco, California, USA, pp. 147-152, 1996.

[4] J. G. Bender, "An Overview os Systems Studies of Automated Highway Systems", *IEEE Trans. on Vehicular Technology*, Vol. 40, no. 1, pp. 82-99, 1991.

[5] H. Peng and M. Tomizuka, "Preview Control for Vehicle Lateral Guidance in Highway Automation", *ASME Journal of Dynamic Systems, Measurement and Control*, Vol.115, No.4, pp.678-686, 1993.

[6] H. Pham, K. Hedrick, and M. Tomizuka, "Combined Lateral and Longitudinal Control of Vehicles", *Proc. of the American Control Cof.*, Baltimore, Maryland, pp. 1205-1206, 1994.

[7] T. Hessenburg, H. Peng, W.-B. Zhang, A. Arai, and M. Tomizuka, "Experimantal Results of Fuzzy Logic Control for Lateral Vehicle Guidance", *Publication of PATH Project*, UCB-ITS-PRR-94-03, ITS, UC Berkeley, Frbruary, 1994.

[8] J. Guldner, W. Sienel, H.-S. Tan, J. Ackermann, S. Patwardhan and T. Bunte, "Robust Automatic Steering Control for Look-down Reference Systems with Front and Rear Sensors", *IEEE Transaction on Control Systems Technology*, Vol. 7, no. 1, pp. 2-11, 1999.

[9] H.-S. Tan, J. Guldner, S. Patwardhan, C. Chen and B. Bougler, "The Development of an Automated Steering Vehicle Based on Roadway Magnets- A Case Study of Mechatronic System Design", *to appear in IEEE/ASME Transactions on Mechatronics* (1999).

[10] J. Ackermann, "Robust Decoupling of Car Steering Dynamics with Arbitrary Mass Distribution", *Proc. of the American Control Conf.*, Baltimore, Maryland, pp. 1964-1968, 1994.

[11] C. Chen and H.-S. Tan, "Steering Control of High Speed Vehicles: Dynamic Look Ahead and Yaw Rate Feedback", *Proc. IEEE Conf. Decision and Control*, Tampa, Florida, USA, pp. 1025-1030, December, 1998.

[12] L. Segel, "Theoretical Prediction and Experimental Substantiation of the Response of the Automobile to Steering Control", *Automobile Devision, The Institute of Mechanical Engineers*, pp. 22-46, 1956.

[13] R.L. Nisonger and D.N. Wormley, "Dynamic Performance of Automated Guideway Transit Vehicles", *ASME J. of Dynamic Sys., Meas. and Cont.*, Vol. 100, pp. 88-94, March, 1978.

[14] E. C. Yeh and R.-H. Wu, "Closed-loop design for Decoupling Control of a Four-wheel Steering Vehicle", *Int. J. of Vehicle Design*, Vol. 10, no. 6, pp. 703-727, 1989.

[15] A. G. Nalecz, "Investigation into the Effects of Suspension Design on Stability of Light Vehicles", *SAE Transaction*, Vol. 96, No. 1, Paper No. 870497, 1987.

[16] H.-S. Tan, R. Rajamani and W.-B. Zhang, "Demonstration of an Automated Highway Platoon System", *Proc. of the American Control Cof.*, Phildelphia, PA, pp. 1823-1827, 1998.

[17] P. Lunger, "The Influence of the Structure of Automobile Models and Tyre Characteristics on the Theoretical Results of Steady-state and Transient Vehicle Performance", *The Dynamic of Vehicles*, Proc. 5th VSD-2 IUTAM Symp., Vienna, Sept. 1977.

[18] T. D. Gillespie, "Fundamental of Vehicle Dynamics", *Society of Automotive Engineers, Inc.*, Second Printing, 1992.

[19] J.Y. Wong," Theory of Ground Vehicle", *John Wiley & Sons Inc.*, 1993.

[20] E. Bakker, L. Nyborg and H. B. Pacejka, "Tyre Modeling for Use in Vehicle Dynamic Studies", *International Congress and Exposition*, Detroit, MI, SAE paper 870421, 1987.

[21] E. Bakker, H.B. Pacejka and L. Lidner, "A New Tyre Model with an Application in Vehicle Dynamic Studies", *SAE Trans. J. of Passenger Cars*, , Vol. 98, SAE paper 890087, 1989.

[22] J.C. Doyle, K. Glover, P.P. Khargonekar and B.A. Francis, "State-space solution to Standard H_2 and H_∞ control problems", *IEEE Trans.*, AC-34, pp. 831-847, 1989.

[23] A. Packard and J. Doyle, "The Complex Structured Singular Value", *Automatica*, Vol. 29, pp. 71-109, 1993.

[24] G. J. Balas, J. C. Doyle, K. Glover, A. Packard and R. Smith, "μ-analysis and Synthesis Toolbox: User's Guide", *The Mathworks Inc.*, 1993.

9 Nomenclature

y : lateral displacement at CG w.r.t local frame (X, Y)

y_r : lateral displacement at CG w.r.t. road reference frame (X_r, Y_r)

y_f : lateral displacement at front sensor w.r.t. road reference frame (X_r, Y_r)

y_b : lateral displacement at rear sensor w.r.t. road reference frame (X_r, Y_r)

ε : yaw angle w.r.t local frame (X, Y)

ε : yaw angle w.r.t. road reference frame (X_r, Y_r)

ε_d : desired yaw angle from road curvature

ϕ : roll angle

δ : steering angle

F_{wy} : disturbance force at vehicle CG along y direction

F_{ai} : longitudinal force along the vehicle direction

F_{bi} : lateral force perpendicular to the vehicle direction

F_{xi} : longitudinal force along the tire orientation

F_{yi} : lateral force perpendicular to the tire orientation

V : vehicle forward velocity

ρ : radius of road curvature

10 Appendix

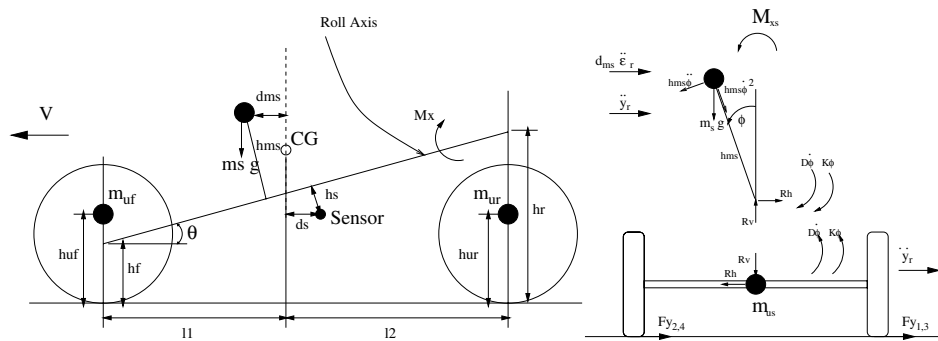## 10.1 Derivation of the nonlinear 3 DOF vehicle model

Figure 16: Schematic diagram of the side view (left) and the front view (right) of the vehicle

The vehicle model is derived by the newtonian method. As shown in the right figure of Fig. 16, the sprung mass rotates counterclockwise as the unsprung mass subjected to a lateral

25

force to the right. The balance of force along the lateral direction and the moment balance along the roll and yaw directions can be obtained by:

$$m_{us}(\ddot{y} + V\dot{\varepsilon}) = F_{b1} + F_{b2} + F_{b3} + F_{b4} + F_{wy} - R_h \tag{34}$$

$$I_{x_{m_s}}\ddot{\phi} = R_v h_{m_s} \sin\phi + R_h h_{m_s} \cos\phi - (K_1 + K_2)\phi - (D_1 + D_2)\dot{\phi} \tag{35}$$

$$I_{z_{us}}\ddot{\varepsilon} = M_{z_{us}} - R_h d_{m_s} \tag{36}$$

where $\theta = \tan^{-1}\frac{h_r - h_f}{l_1 + l_2}$ is the decline angle of the roll axis with respect to the ground. $(K_1 + K_2)\phi$ and $(D_1 + D_2)\dot{\phi}$ are the moments induced by the suspension springs and shock obsorbers. $I_{z_{us}}$ is the moment of inertia of the unsprung masses along the z axis which is centered at CG. $I_{x_{m_s}}$ is the moment of inertia of the sprung mass along the roll axis which is centered at the sprung mass m_s. The reaction froce R_v and R_h between sprung and unsprung masses can be obtained by:

$$R_h = m_s(\ddot{y} + V\dot{\varepsilon}) + m_s h_{m_s}\phi^2 \sin\phi - m_s h_{m_s}\ddot{\phi}\cos\phi + m_s d_{m_s}\ddot{\varepsilon} \tag{37}$$

$$R_v \sin\phi + R_h \cos\phi =$$
$$m_s g \cos\theta \sin\phi - m_s h_{m_s}\ddot{\phi} + m_s(\ddot{y} + V\dot{\varepsilon})\cos\phi + m_s d_{m_s}\ddot{\varepsilon}\cos\phi \tag{38}$$

$M_{z_{us}}$ is the moment induced from the contact forces between the tires and the road surface:

$$M_{z_{us}} = l_1(F_{b_1} + F_{b_2}) - l_2(F_{b_3} + F_{b_4}) - \frac{S_b}{2}(F_{a_1} + F_{a_3}) + \frac{S_b}{2}(F_{a_2} + F_{a_4}) \tag{39}$$

Define $I_z = I_{z_{us}} + m_s d_{m_s}^2$: the moment of inertia of both the sprung and unsprung masses along the z axis which is centered at CG; $I_{x_s} = I_{x_{m_s}} + m_s h_{m_s}^2$: the moment of inertia of the sprung mass along the roll axis which is centered at the roll axis. The dynamic equations of motion in terms of lateral y, roll ϕ and yaw ε directions can be derived by combining Eqs.(34)-(39) as:

$$M(\ddot{y} + V\dot{\varepsilon}) - m_s h_{m_s}\ddot{\phi}\cos\phi + m_s h_{m_s}\dot{\phi}^2 \sin\phi + m_s d_{m_s}\ddot{\varepsilon} =$$
$$F_{b1} + F_{b2} + F_{b3} + F_{b4} + F_{wy} \tag{40}$$

$$I_{x_s}\ddot{\phi} - m_s(\ddot{y} + V\dot{\varepsilon})h_{ms}\cos\phi - m_s h_{m_s}d_{m_s}\ddot{\varepsilon}\cos\phi =$$
$$m_s g h_{m_s}\sin\phi\cos\theta - (K_1 + K_2)\phi - (D_1 + D_2)\dot{\phi} \tag{41}$$

$$I_z\ddot{\varepsilon} + m_s d_{m_s}(\ddot{y} + V\dot{\varepsilon}) + m_s h_{m_s}d_{m_s}\dot{\phi}^2 \sin\phi - m_s h_{m_s}d_{m_s}\ddot{\phi}\cos\phi =$$
$$l_1(F_{b_1} + F_{b_2}) - l_2(F_{b_3} + F_{b_4}) - \frac{S_b}{2}(F_{a_1} + F_{a_3}) + \frac{S_b}{2}(F_{a_2} + F_{a_4}) \tag{42}$$

10.2   Table 1: the 3 DOF vehicle parameters

Vehicle mass (M):	$1740Kg$
Sprung mass (m_s):	$1600Kg$
Front unsprung mass (m_{uf}):	$80Kg$
Rear unsprung mass (m_{ur}):	$60Kg$
Roll inertia (I_{x_s}):	$420Kg \cdot m^2$
Yaw inertia (I_z):	$3214Kg \cdot m^2$
Front tire cornering stiffness (C_1):	$29000N/rad$
Rear tire cornering stiffness (C_2):	$60000N/rad$
Front axle to CG (l_1):	$1.058m$
Rear axle to CG (l_2):	$1.756m$
Front bumper to CG (d_f):	$1.758m$
Rear bumper to CG (d_b):	$2.456m$
Wheel base (S_b):	$1.5m$
Roll damping (D_i):	$1000N \cdot m \cdot sec$
Roll stiffness (K_i):	$20000N \cdot m$
Sprung mass center to sprung mass (h_{m_s})	$0.38m$
Height of front unsprung mass (h_{uf})	$0.3m$
Height of rear unsprung mass (h_{ur})	$0.35m$
Center of front unsprung mass (h_f)	$0.25m$
Center of rear unsprung mass (h_r)	$0.75m$
Roll steering coefficient (γ):	1000
Actuator damping ratio (ξ):	0.4
Actuator natural frequency (ω_n):	$5Hz$

Development of An Automated Steering Vehicle Based on Roadway Magnets - A Case Study of Mechatronic System Design

Han-Shue Tan, Jürgen Guldner, Satyajit Patwardhan, Chieh Chen, and Bénédicte Bougler

Abstract - Automated steering control is a crucial element of vehicle automation. California PATH has developed one such system using magnetic markers embedded under the roadway for lateral guidance. This system was demonstrated during the August 1997 National Automated Highway System Consortium Feasibility Demonstration in San Diego without a single failure. Developing a successful demonstration system not only required theoretical understanding of the various control problems involved, but also strong appreciation of all practical issues. In this paper, the comprehensive process of developing such automated steering control system is described. This process consists of control objectives' determination, system structure definition, vehicle dynamics validation, lateral sensing system development, steering actuator design, test track installation, control algorithm development, software/hardware integration and vehicle testing. The entire process also serves as a good case study for mechatronic system design integrating mechanical components, electronic devices, intelligence, and feedback control to perform vehicle automation functions.

I. INTRODUCTION.

Traffic congestion problems and driving safety issues on highways have motivated an increased amount of research on highway automation and have being investigated worldwide in several programs, such as ITS in the US (see [1] for example) and ASV, SSVS and ARTS under ITS Japan [2]. Comprehensive overviews of the Automated Highway System (AHS) were given by [3, 4]. The August 1997 National Automated Highway System Consortium (NAHSC) Demonstration, which took place on an eight-mile highway at I-15 in San Diego, was requested by the US Congress to demonstrate technical feasibility of AHS. The PATH platoon demonstration was one of the key elements of this demonstration. The demonstration system included eight fully automated automobiles traveling at highway speed with a

spacing of 6.5 meters [5]. The functions that were demonstrated included: lane-keeping, lane-changing, close spacing longitudinal control, and platoon split and join [6]. The test data at I-15 indicated that the automated steering control system kept the vehicle within 5 centimeters to the lane center at freeway speed with less than 10 centimeters maximum error at some curve transitions. Using the same control algorithm, the high-g single vehicle Miramar Mini Demo has also demonstrated the strong capability of the automated steering control system to sustain speeds with 0.5-g lateral acceleration and 95% of the tracking error within 10 centimeters. No single failure occurred for the steering control system throughout the four-day demonstration period. This paper will describe the development of the automated steering control system used by the PATH system.

An AHS vehicle requires two basic control tasks: longitudinal control and lateral control. Longitudinal control involves regulating the vehicle speed to keep proper spacing between vehicles. Lateral control maintains the vehicle in the center of the lane (lane-keeping maneuver) and steers the vehicle to an adjacent lane (lane-change maneuver), while maintaining good passenger comfort at all times. An automated steering control system needs to accomplish the following two tasks: (1) determine in real-time the vehicle position with respect to a reference path on the road, and (2) design a steering control system that steers the vehicle along the desired path. Human drivers have performed the tasks quite well every day using vision perception, future trajectory interpretation and hand-eye coordination. However, the replication of such functions turned out to be a non-trivial task. The practical and technical challenges were created by the strong performance and reliability requirements. One of the most important elements of an automated steering control system is the reference and sensing systems. The reference and sensing systems can be classified into two categories: look-ahead systems (e.g., machine vision systems) and look-down systems (e.g., magnetic markers installed in the center of the roadway). Look-ahead systems replicate human driving behavior by measuring the lateral displacement ahead of the vehicle, preferably increasing the look-ahead distance with increasing vehicle velocity. A number of research groups have conducted highway speed experiments using machine vision [7, 8, 9]. However, the susceptibility to variation of light or inclement

.H.-S. Tan and B. Bougler are with California PATH, University of California at Berkeley, Institute of Transportation Studies, Richmond, CA 94804-4698 USA.
J. Guldner is with BMW Technik GmbH, 80788 München, Germany.
S. Patwardhan is with Cyclonics Inc., Fremont, CA 94538 USA.
C. Chen is with Department of Mechanical Engineering, National Chiao Tung University, Hsinchu, Taiwan, 30050, R.O.C.

weather conditions is still problematic to the machine vision systems. The look-ahead effect can also be accomplished using radar reflective stripes [10] or other energy emitting or reflecting devices.

Look-down reference systems, on the other hand, measure the lateral displacement at a location within or in the close vicinity of the vehicle boundaries, typically straight down from the bumpers. Examples of the look-down reference systems are electric wire guidelines, first tested at The Ohio State University (OSU) in the US [11] for passenger cars and later by Daimler-Benz and MAN in Germany [12] for buses; radar reflecting guard rails studied at OSU [13]; and magnetic markers used by the California PATH Program [14]. Look-down reference systems are usually more reliable due to the smaller distance between the sensor and the road markers. This smaller distance is also the source of system limitations. The short look-ahead distance (both longitudinally and laterally) reduces the phase lead that is essential for good steering control [15]. Furthermore, the smaller lateral sensor range demands larger control gains for robustness. The automated lane-change maneuver is also more difficult when there is an area between lanes where no vehicle position measurement is available due to the finite sensing range of the look-down reference systems [16].

The two key requirements for a successful public demonstration of an automated steering vehicle are safety and performance. Safety means reliability and robustness. Performance highlights the consistency and passenger comfort. Since the strength of any system rests on its weakest component, no aspect of this system should be overlooked. The development demanded not only technical understanding of the control problems but also strong appreciation of system engineering practice. The researchers were very interested in demonstrating to themselves the "engineering" feasibility of an automated steering control vehicle. In particular, the question was posed whether it was feasible to design an automated steering control system based on a "look-down" lateral sensing system that could handle almost all practical steering scenarios. The ambitious goal and the short time table led to an aggressive one-year development period that combined technical research with product development. The entire process consisted of control objectives' determination, control problem analysis, lateral sensing system development, steering actuator design, test track installation, roadway coding and decoding schemes development, vehicle dynamics validation, control algorithm design, software integration and vehicle testing. Like any good mechatronic system design, every element was crucial to the success of the demonstration.

The dual purposes of this paper are to comprehensively report an automated steering control system design as well as to present this process as an example of a mechatronic system development. This paper is organized as follows. Section 2 explains the system requirements, configuration and design philosophy, Section 3 performs the system analysis and determines the control system topology. Section 4 describes the sensing system based on the magnetic markers. Steering actuator development is reported in Section 5 and vehicle model is validated and presented in Section 6. Lane-keeping and lane-change control algorithms are discussed in Section 7 and 8, respectively. Section 9 describes the hardware and software structures. Section 10 shows the demonstration test results and Section 11 concludes the paper.

II. SYSTEM CONFIGURATION, REQUIREMENTS AND DESIGN PHILOSOPHY

Four basic system components are required for an automated steering control system: (1) road markers or any other kind of road indicators that define the road, (2) sensors recognizing the road markers, (3) intelligence to determine how to steer, and (4) steering actuator that steers the wheels. The lateral reference system employed by the PATH demonstration is based on the magnetic markers embedded under the roadway center. Such reference system is generally more reliable due to the relatively short distance between the roadway magnets and the sensors (magnetometers) in the vehicle. However, the "look-down" nature of this sensing system creates a difficult control problem when high speed and high control authority are required [15]. An add-on brushless DC motor mounted on the upper steering column was chosen to be the steering actuator. Using the existing hydraulic assist system for steering power, such actuator design is relatively simple and potentially inexpensive. However it also produces an interesting servo design problem that pushes the bandwidth of the steering actuator close to the natural frequency of the handwheel mass and steering column. The brain of the system is a Pentium 166 MHz PC computer with rugged chassis. It performs both signal processing and real-time control functions. Since no magnet measurement is available between lanes, inertial sensors were installed in the vehicle to support dead reckoning estimation during automated lane-change maneuvers.

The performance requirements for the demonstration of the automated steering control system were straight forward: the steering control system needed to perform both automated lane-keeping and lane-change maneuvers at highway speeds with good tracking accuracy and good passenger comfort. In order to negotiate the Mini Demo sharp curves, the automated vehicle needed to maintain at least 0.3-g lateral acceleration without ever coming close to the lateral sensor limit (±50 centimeters). Finally, extremely high reliability was required for a safe public demonstration.

The closed-loop system performance requirements were then flown down from the demonstration requirements. These performance requirements included the following:
(1) 0.15 meter maximum tracking error for highway driving and 0.3 meter maximum error for 0.3-g automated steering maneuvers without any prior knowledge of the roadway;
(2) no noticeable oscillations at frequencies above 0.3 Hz for passenger comfort, and 0.4 minimum damping coefficient for any mode at lower frequencies;
(3) 1 m/s^2 maximum lateral acceleration deviation between the lateral acceleration created by the vehicle and that from the road;
(4) 200 minimum consecutive successful lane changes at freeway speeds with various loading conditions;

(5) consistent performance under various vehicle operating conditions.

The corresponding subsystem requirements were generated from the system performance requirements. These subsystem requirements are summarized as follows:

(1) at least 1 centimeter accuracy for the lateral displacement measurements,

(2) 0.1% maximum rate of misreading markers on the highway,

(3) 5 Hz minimum steering actuator bandwidth during normal operation.

Finally, the following limitations were imposed as the practical constraints for the control system:

(1) 2 centimeter maximum lateral error on the marker installation,

(2) 25 degree per second maximum rate of steering angle change when measured at the tire,

(3) existence of 0.005 rad/sec yaw rate sensor noise in addition to the possible sensor drift.

The objective was to develop a reliable automated steering control system that achieved all the above requirements. The process included the design and integration of reliable sensing system, reliable actuator, robust controller and robust decision making. The public demonstration involved the following three difficult scenarios: eight vehicles under automated control at close spacing, one vehicle performing automated high-g maneuvers with concrete barriers all around, and dead reckoning lane change at high speeds with limited sensor range. Since the fine tuning of the controller based on exact vehicle parameters was almost impossible for such scenarios, the philosophy of the controller design was to attain an acceptable performance under even the worst scenario. The concept of using "high gain" lane-keeping controller was adopted to achieve the robustness against various environmental conditions, whereas soft trajectory planning was used for maintaining passenger comfort. The key concept was the realization of the fact that every process in the integration design was crucial for the final success of the product.

III. CONTROL SYSTEM ANALYSIS

A linearized model is sufficient for studying vehicle steering under *normal* conditions [17]. Assuming small angles, this allows to use the classical *bicycle model* shown in Figure 3.1. The transfer function from steering angle to the lateral acceleration produced at the sensor location S (d_s in front of the CG) is:

$$\ddot{y}_S(s) = V_S(s)\delta_f(s)$$

$$= \frac{\mu c_f v^2 (Ml_f d_S + I_\psi)s^2 + \mu^2 c_f c_r lv(d_S + l_r)s + \mu^2 c_f c_r lv^2}{D(s)}\delta_f(s)$$

with

$$D(s) = I_\psi M v^2 s^2 + \mu v(I_\psi(c_f + c_r) + M(c_f l_f^2 + c_r l_r^2))s + \mu M v^2(c_r l_r - c_f l_f) + \mu^2 c_f c_r l^2,$$

where I_ψ is the yaw moment of inertia, M the mass of the vehicle, μ the road adhesion coefficient, $l=l_f+l_r$ the wheel base, c_f and c_r the cornering stiffness of the front and rear tires respectively and v the longitudinal vehicle speed. The front wheel steering angle δ_f is realized by the actuator $A(s)$. The

desired lateral acceleration at S is $\ddot{y}_{ref} = v^2 \rho_{ref}$, with the road curvature ρ_{ref}. This yields the vehicle lateral model as shown in Figure 3.2, where the subsystems are identified as: (I) vehicle kinematics, (II) force generation mechanism, (III) road reference and (IV) steering actuator.
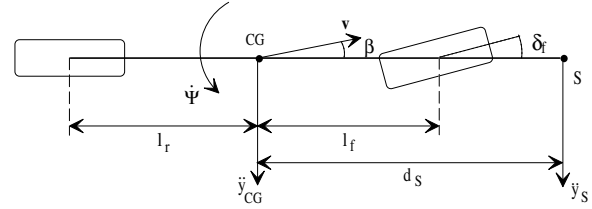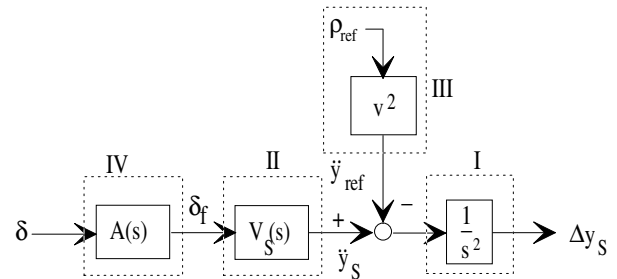

Fig. 3.1. Bicycle model.

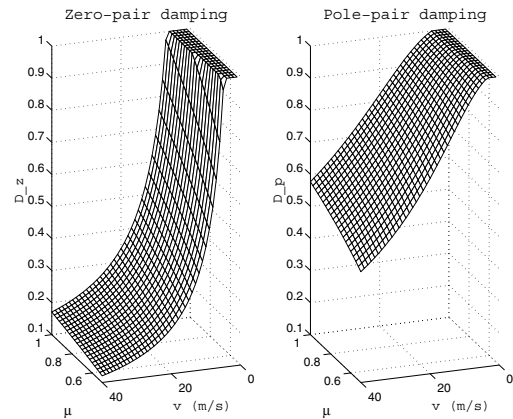Fig. 3.2. Block diagram of vehicle system dynamics.

Fig. 3.3. Vehicle pole-zero damping ratio (μ: coefficient of road adhesion, v: vehicle speed).

In order to study the effect of lateral displacement output feedback, the pole-zero locations of the vehicle dynamics $V_s(s)$ are first examined with the sensor located under the front bumper. Figure 3.3 shows the rapid decrease in pole and zero damping in $V_s(s)$, with increase of velocity and deterioration of road surface. Any high gain controller tends to drive the closed-loop poles towards the open-loop zeros, resulting in poorly damped closed-loop poles. A perfect pole-zero cancellation is impossible because of the system parameter uncertainties. However, attempting to cancel the $V_s(s)$ zeros by a pair of poles would result in a poorly damped imperfect pole-zero cancellation. Moreover, the lightly damped poles introduced by the controller would show up in yaw dynamics, without the corresponding zeros cancellation. This would result

in excessive fish-tailing of the vehicle. The above analysis concludes that a pure lateral displacement output feedback is impractical for highway speed automated steering control under the given performance requirements and design constraints [15, 19, 20].

The above discussion suggests to modify the system control structure. Three possible options were considered: preview with the road curvature information, inertial sensor feedback, and modification of the system zeros. When the curvature information is known to the vehicle [17, 18], a feed-forward term based on the road curvature and vehicle dynamics can be generated in the controller to lessen the need for high gain feedback. However, due to uncertainty in $V_s(s)$, especially at high speeds, the feed-forward calculations are at best an approximation. Furthermore, a strong feedback control is still the key for a robust system; the feedforward control does not alleviate the stability and noise rejection problems. A feedback scheme utilizing the feedback of the inertial sensors like accelerometer and yaw rate can also be used to change the pole locations. However, these schemes can not modify the poorly damped zeros of $V_s(s)$. In turn, the closed-loop poles still are attracted towards the lightly damped zeros and lead to poor closed-loop characteristics. Thus, neither road preview feedforward control nor inertial sensor feedback control is efficient for dealing with the high speed steering control problem.

Since the system zeros of $V_s(s)$ are determined by the sensor location S, a proportional increase of d_s to speed v seems to be required -- an observation known from human driving. Moreover, the modification of d_s does change the location of zeros in $V_s(s)$. A virtual look-ahead concept was therefore proposed for the look-down lateral sensing system [19, 20]. Complementing the lateral displacement sensor S at the front bumper by a second displacement sensor T, preferably placed at the tail of the vehicle, extrapolates the displacement measurement forward to a virtually increased look ahead distance d_v beyond the vehicle boundaries. This conclusion turns out to be the key concept that allows for the high gain robust steering controller design.

IV. SENSING SYSTEM DEVELOPMENT

The prerequisite to assure a robust steering control system is the reliability of the lateral sensing system. One of the important attributes to the magnetic marker lateral reference system is its reliability. Several algorithms have been designed to detect the relative position between the marker (nail) and sensor (magnetometer), as well as to read the code embedded within a sequence of these markers. Three magnet marker detection and mapping algorithms have been experimented by PATH. The first is called the "peak-mapping" method that utilizes a single magnetometer to estimate the marker's relative lateral position when the sensor is passing over the magnet. The second algorithm is the "vector ratio" method that requires a pair of magnetometers to sample the field at two locations, and returns a sequence of lateral estimates when the magnet is in between sensors. However, a singularity exists when the magnet is directly under a sensor. The third algorithm is the

"differential peak-mapping" that compares the magnetic field measurements at two observation points in order to eliminate the common-mode contributions. It determines the lateral position by using a functional relationship between the differential sensor readings and the knowledge of the sensor geometry. Because of its proven effectiveness over a wide range of vehicle speeds, the "peak-mapping" algorithm was chosen for the demonstration.

The magnetometer signal processing for the "peak-mapping" method involves the following three procedures: peak detection, earth field removal and lateral displacement table look-up. Although the algorithm is straightforward in principle, it becomes complicated when the major concern is the reliability of the process. Many parameters in the lateral sensing signal processing software need to be tuned in order to provide consistent lateral displacement information regardless of vehicle speeds, orientations, operating lateral offsets and vehicle body bouncing. Debugging becomes time consuming when the failure condition could not be recreated. In order to improve the reliability of the lateral sensing system with the magnetic road markers, a "reconstructive" software system for the lateral sensing signal processing was developed. When specified as a "reconstructive run", the real-time software in the vehicle, besides processing data as usual, stores all sensor data in the memory and later dumps them into a data file. Identical signal processing software as the one run in the real-time environment could later on be generated in a desktop computer with the same operating system using the raw sensor data stored during vehicle testing. Such a setup enables any erroneous situation to be recreated in a lab environment and to be debugged with ease. By using this new development environment, the developers could (1) capture the problematic performance as soon as it happens, (2) recreate the situation step by step in the lab environment, and (3) modify the software as well as validate the changes before upgrading the software in the test vehicle.

Three magnetometers were installed under both the front and rear bumpers to extend the range of the lateral sensor. The resultant signal processing algorithm achieved combined sensor range of ±50 centimeters with accuracy better than 1 centimeter. An independent lateral measurement has shown that the standard deviation of such measurement was under 0.4 centimeter [14]. Furthermore, the ratio of misreading magnet was less than 0.1% for speeds up to 90 mph under various loading conditions.

The roadway information is encoded into the magnets by exploiting binary polarity coding [18]. The signal processing algorithm also outputs the magnet polarities to the corresponding decoding scheme in order to retrieve the coded road information such as upcoming road geometry or lane merges/diverges locations from the roadway to the automated vehicles.

V. STEERING ACTUATOR DEVELOPMENT

The system analysis has also shown that the practical limitations of the steering actuator had an adverse effect on the lane-keeping performance, especially when a look-down lateral

sensing system was employed. The bandwidth and phase characteristics of the actuator have a significant impact on the steering control design. The maximum impact usually shows up within the frequency ranges from 1 to 4 Hz, the upper range of the vehicle fundamental lateral modes. The actuator becomes one of the strongest limitations in providing sufficient damping to the automatic steering control system at frequencies above 1 Hz. Minimum steering actuator specifications have thus been developed to reduce such restrictions. Some of the performance specifications are summarized as follows:

(1) accuracy: 0.1 degree at the road wheel or 0.4% of road wheel angle, whichever is greater;

(2) time domain response: 90% rise time = 0.1 sec, maximum overshoot = 5%, 2% settling time = 0.35 sec with 1 degree road wheel steering command;

(3) frequency domain response: 45 degree phase lag at 5Hz for 0.5 degree amplitude sinusoidal steering command at road wheel.

As a parallel effort, PATH and General Motors Saginaw Steering Division worked together to develop one such automatic steering actuator. The central piece of the steering actuator is an add-on DC motor attached to the top portion of the steering column through a gear interface. When a desired position is sent to the steering actuator controller, a command is sent out to the brushless DC motor. The motor then drives the standard hydraulic assist system in the vehicle. An encoder is installed on the motor shaft to measure the motor position for the servo loop. The accuracy of the tire position was verified using a separated tire position sensor during the design procedure to ensure that the performance requirements are attained without the direct measurement at the tire.

In order to satisfy all the requirements, iterations of the hardware and algorithm designs were conducted. The iterations included the following procedures: model development, model validation, data analysis, linear compensator design, small signal and friction analysis, hydraulic low gain evaluation, nonlinear compensator design, benchmark and vehicle performance validation, user interface development, software interface development, and fault management development. Some key results are briefly described in the following paragraphs.

Figure 5.1 shows the block diagram (Simulink model) of the steering actuator model. The parameters of the model were tuned until the fundamental frequencies associated with the motor and the handwheel were matched using the data from open and closed-loop frequency tests as well as various step response tests. Figure 5.2 shows a comparison of open-loop frequency response for model versus actual test data. Non-linearity such as rack friction and hydraulic characteristics generated the discrepancy on the gain plots at higher frequencies.

An initial linear compensator was designed based on the above model as shown in Figure 5.3. The corresponding closed-loop responses for various operating conditions are illustrated in Figure 5.4. As shown in Figure 5.4, the basic performance specifications have been met except for steering actuator saturation (large phase lag above 3 Hz) at command amplitudes larger than 1 degree.

The final compensator implemented in the actuator that satisfied the performance specifications 1, 2 and 3 is shown in Figure 5.5. The similarities between the initial design based on the model and the final design based on tuning demonstrated the effectiveness of the design process (the gain difference between Figures 5.3 and 5.5 is mainly due to the difference in scaling). At very small steering amplitudes, the rack position did not meet the required specifications because of the combination of mechanical friction and low gains near zero in the hydraulic curve. In order to remedy such problem, non-linear techniques were implemented parallel to the linear compensator to boost the rack motion at very low input amplitudes. See [21] for more detailed description of the steering actuator design.
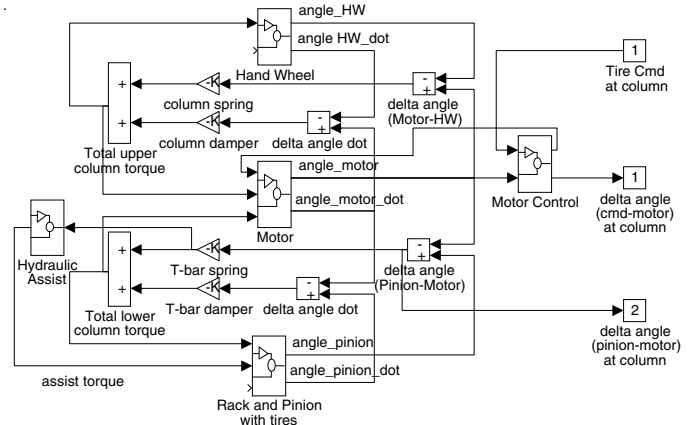

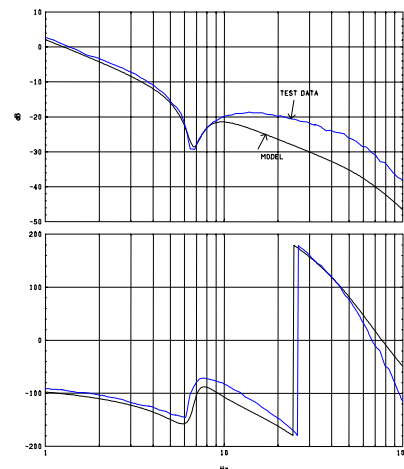Fig. 5.1. Matlab block diagram of steering actuator model.

Fig. 5.2. Open-loop frequency response comparison from motor command to tire position: model vs. plant. (360 degree jump at around 22Hz due to the phase wrapping between ± 180 degree).
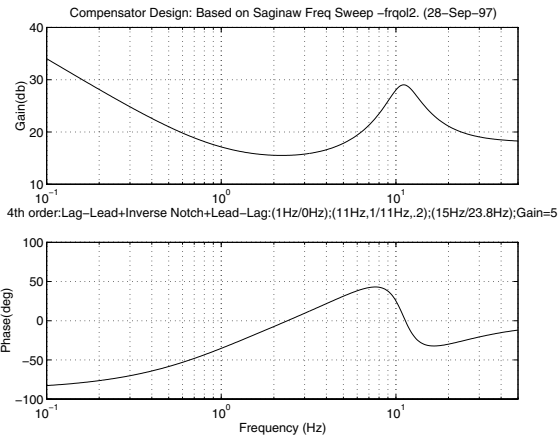
Fig. 5.3. Initial compensator design (motor position error to motor command).
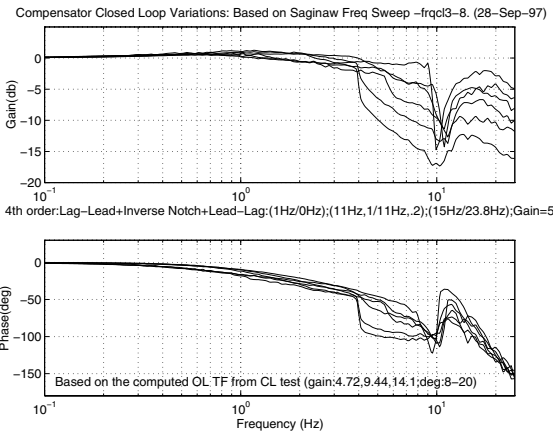

Fig. 5.4. Initial closed-loop responses (commanded motor position to motor position).
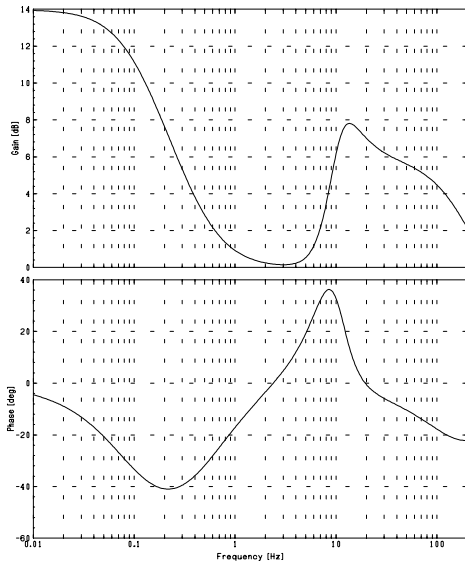

Fig. 5.5. Final compensator design (motor position error to motor command).

VI. VEHICLE DYNAMICS VALIDATION

The vehicle lateral characteristics for the LeSabre test vehicle were verified through the open-loop frequency sweep technique. Various amplitudes of steering commands, with frequencies ranging from 0.1 Hz to 6 Hz, were applied to steer the vehicle at speeds of 22, 45, and 67 mph (10, 20 and 30 m/s respectively). Data analysis was then performed to obtain the lateral frequency responses of the vehicle. Figures 6.1 and 6.2 show the resultant LeSabre transfer functions, from steering command at front tire to lateral acceleration and yaw rate, respectively.
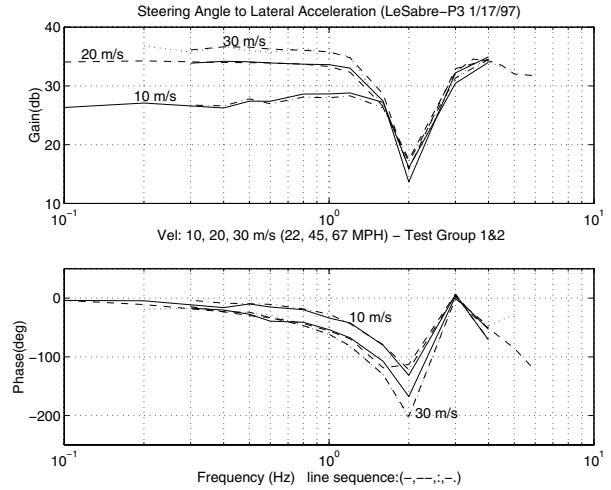
Fig. 6.1. LeSabre lateral dynamics (steering command to lateral acceleration).
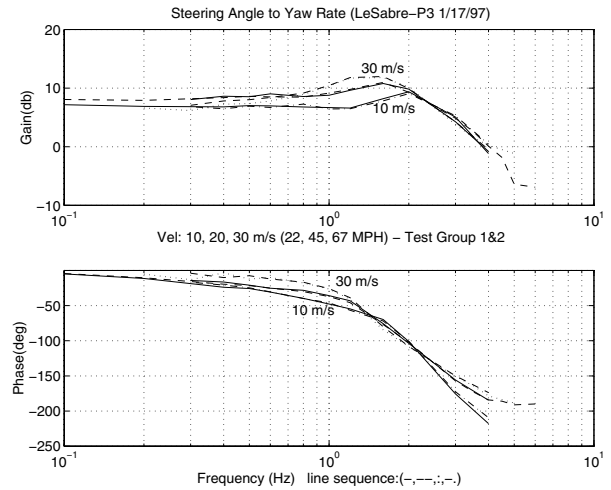

Fig. 6.2. LeSabre lateral dynamics (steering command to yaw rate).

In these two figures, two different methods applied to two different sets of test data yield almost identical results. The transfer functions of the LeSabre conclude the following:

(1) The understeer characteristics are significant. The lateral characteristics are therefore more sensitive to vehicle speed changes. Furthermore, the preview steering angle based on geometry produces larger mismatch when the vehicle is traveling at higher speed.

(2) The frequency response from steering command to lateral acceleration at CG has a deeper "notch" effect between 1 to 2 Hz than what the bicycle model predicts. This frequency range coincides with the fundamental roll suspension mode of the LeSabre.

The conventional bicycle model, which only includes lateral and yaw dynamics, can not reproduce the lowered gain and phase characteristics in the frequency range from 1 to 4 Hz as

shown in Figures 6.1 and 6.2. In order to substantiate the suspension effect in the test data, a linear vehicle model with suspension roll dynamics was developed in [22]. The model identification results matched the test data and confirmed the contribution from the vehicle roll dynamics to the steering dynamics. As a result, the soft suspension of the LeSabre generated additional phase lag that limited the achievable bandwidth of the automated steering control to the frequency below the suspension frequency. This also increased the difficulty of control system design.

VII. CONTROL ALGORITHM DEVELOPMENT

In order to experimentally validate the analysis results in Section 3 concerning the advantages of the virtual look-ahead concept, various look-ahead distances were experimented on the LeSabre. A constant proportional feedback steering control with varying virtual look-ahead distance (from 0 to 10 car length virtual look-ahead distances where one car length equals to 4.8 meters) was first implemented in the LeSabre and experimented at I-15 with different vehicle speeds. The experiments concluded the following observations:
(1) The shorter the look-ahead distance is, the more oscillatory the closed-loop lateral mode is.
(2) The longer the look-ahead distance is, the larger both the actuator mode oscillation and the high frequency noise are.
The additional look-ahead distance creates the needed phase-lead starting from the yaw natural frequency, however this also comes with the side effect of increasing controller gains at higher frequencies. With the soft suspension of the LeSabre, high control gain above 1 Hz is likely to excite the suspension oscillation, especially at high vehicle speeds. Therefore as one increases the look-ahead distance, one has to reduce the overall controller gain. This generates large steady state error when large virtual look-ahead distance is used.

Many different control algorithms have been tested with the virtual look-ahead concept. Among them, a simple controller such as PI (proportional plus integration) control achieved automated steering control for speeds up to 70 mph at I-15 using several car length virtual look-ahead distance [19]; link control concept [23] where the vehicle is towed by an imaginary link that connects to the road center several car length ahead of the vehicle, also achieved 65 mph automatic highway lane-keeping. However, the PI controller prefers lower controller gain in order to maintain good passenger comfort, thus limits its ability for robust performance. The link controller is stiff at high frequencies and it tends to excite the vehicle suspension mode. Both controllers use feedforward steering input based on preview road curvature to reduce the need for large controller gains. The main conclusions from these exercises are (1) the virtual look-ahead concept helps tremendously in the steering controller design, and (2) the frequency-shaped capability needs to be incorporated into the virtual look-ahead concept to reduce the adverse effects from extrapolating two potentially noisy measurements.

The control algorithm needs to satisfy both tracking accuracy and ride comfort requirements at all possible vehicle speeds regardless of the following uncertainties: road adhesion variations, preview errors, loss of road curvature information, marker installation misalignments, actuator bandwidth, vehicle dynamics changes, soft suspension modes, and all reasonable sensor and vehicle noises. A frequency shaped virtual look-ahead lane-keeping control algorithm using the form of the following equation was developed and implemented:

$$steer = -k_c G_c \left(\left(k_{\text{int}} + k_e k_{ext} \right) y_f - k_e k_{ext} y_r \right), \quad (7.1)$$

where k_{int} is the integrator at front sensor location, k_{ext} the virtual sensor extension filter, G_c the compensator at the virtual sensor location, k_e and k_c constants that can be tuned, y_f and y_r the lateral measurements at front and rear sensors respectively. This algorithm consists of three elements:
(1) an integral control that keeps the steady state tracking error at the front sensor to zero,
(2) a frequency shaped look-ahead distance that provides more look-ahead distance around the vehicle lateral modes and roll-off of the look-ahead distance at higher frequencies,
(3) a servo controller that uses the frequency shaped virtual displacement as input and compensates it for the actuator and suspension dynamics.
Lane-keeping experiments at speeds up to 90 mph were conducted without preview information at I-15 using the frequency shaped virtual look-ahead controller with constant controller parameters. Adding the feedforward steering command based on curvature preview information provides slightly better tracking error (by a few centimeters) during changes of curvature. The overall standard deviation of tracking error is less than four centimeters even at such high speeds.

In order to minimize the adverse effect from any misalignment of the magnet markers, a gain-scheduling scheme was incorporated into the lane-keeping control algorithm to provide a better tradeoff between passenger comfort and tight tracking control. The gain-scheduling scheme consists of a single parameter that changes the magnitude of the controller gain in such a way that the steady state gain decreases with increasing virtual look-ahead distance. A built-in hysteresis, which is applied only when the controller gain is reduced, is employed to eliminate excessive switching. High gain is used in the following situations: low vehicle speed, large tracking error, large lateral acceleration, and large curvature if the road information is known. Otherwise, low gain will be chosen. The scheme provides a single controller that achieves an overall tradeoff among robustness, tightness and comfort.

As part of the preparation of the 1997 NAHSC Demonstration, the robustness properties of the lane-keeping control algorithm were tested extensively on the I-15 test track. Test scenarios included missing magnets, missing coding information, loss of preview information, sudden tight curve transition, high vehicle speeds, and various passenger loading conditions. With several thousand-miles traveling under automated steering control, the lane-keeping algorithm was experimentally validated to be robust against all the above conditions.

VIII. AUTOMATED LANE-CHANGE CONTROL

The purpose of the automated lane-change controller is to steer the vehicle from the current lane to an adjacent lane. The fundamental difference of using look-down or look-ahead sensors in the automated lane-change maneuver resulted from the difference in the range of the lateral sensors. Look-ahead sensor typically has larger sensor range. Lane-change and lane-keeping maneuvers become virtually identical when the lateral sensor sees both lanes. The control problem becomes more complicated when the lateral sensor can not see both lanes and the vehicle must travel certain distance without detecting any markers during lane change. The most uncertain, and thus the most difficulty phase of this maneuver, occurs during the re-acquiring of the new road marker line on the target lane. The difficulty of catching the new marker line increases proportionally to the inverse of the lateral sensor range as well as to the velocity square, and the arriving angle square (the arriving angle is the angle between the vehicle and the new marker line as the sensor first sees the marker) [16].

Two schemes of lane-change maneuvers using roadway maker reference systems were successfully developed at PATH: infrastructure guided lane change and automated free lane change. In the infrastructure guided lane-change scenario, additional magnetic markers are installed between lanes at certain locations on the highway to provide a reference path for automated guided vehicles [16, 18]. This scheme alleviates control and estimation issues but limits the lane-change maneuvers to specific locations on the highway. On the other hand, in the free lane-change scenario, vehicle position is estimated by integrating yaw rate measurement during lane change. A smooth trajectory is generated as a virtual reference path to guide the vehicle in between lanes. However, the major difficulty involved in the free lane-change scenario is the extreme sensitivity of the system performance with respect to sensor noises and vehicle/road parameters variations. In principle, it is not difficult to perform one good lane-change but difficult to execute thousands of consecutive ones. In this paper, the more difficult free lane-change scenario will be discussed.

The proposed automatic free lane-change control algorithm consists of four vital control schemes that closely work with each other [see 24 for detail description]. They are:
(1) a lateral displacement observer/estimator that uses yaw rate sensor,
(2) an adaptive trajectory planning scheme that determines lane-change and lane-catching trajectories,
(3) a robust and high damping lane-keeping control algorithm that brings the vehicle to the road center even at the largest arriving angle created by the estimation errors, and
(4) a state machine that coordinates the above schemes based on sensor signals, available road information and maneuver demands.

The underline philosophy is to design a displacement estimator that results in bounded estimation error; a smart trajectory planning that guarantees the smooth final arrival to the target marker line; a strong lane-keeping controller that is capable of tracking the desired trajectory under the worst design scenario, and a state machine that quickly determines the vehicle operational states.

The idea of the lateral displacement estimator is to determine the lateral displacement based on the yaw rate measurement when the lateral sensors detect no markers in between lanes. Equation (8.1) describes the "kinematic" relationship of the estimate $\hat{y}$ with respect the yaw rate ω, where y_0, θ_0 and ω_0 are the initial conditions or biases of lateral displacement, vehicle angle and yaw rate, respectively:

$$\hat{y} = \hat{y}_0 + V\hat{\theta}_0 t + \tfrac{1}{2} V\hat{\omega}_0 t^2 + V\iint \omega \, dt . \tag{8.1}$$

The basic procedure of the observer/estimator is to first estimate the initial conditions and bias (y_0, θ_0 and ω_0) in Equation (8.1) when the lateral measurements are still available. A simple observer, based on the kinematic relationship between θ and ω, has been developed for these initial condition estimations [24]. When the vehicle exits the sensor range, $\hat{y}$ is computed through Equation (8.1) using the initial condition and bias estimates.

The free lane-change scenario contains two controller states: lane change and lane catching, as shown in Figure 8.1. Each state requires its own trajectory planning:
(1) Lane-change trajectory: This is the trajectory that the vehicle follows to leave the traveling lane (guided by markers) and to perform lane-change maneuver (yaw rate supported dead-reckoning) until the lateral sensor picks up the marker signal at the target lane.
(2) Lane-catching trajectory: This is the trajectory that smoothly leads the vehicle to align itself to the marker line once it sees the first marker of the target lane.

Simple third or fifth order polynomials based on either the first or last lateral measurements are used for the trajectory planning. The length of the trajectory planning is adaptive to the vehicle speed so that the time of dead-reckoning is limited to 3-5 seconds. Furthermore, the lane-change trajectory modifies itself if the vehicle does not reach the target lane after a prescribed time interval.
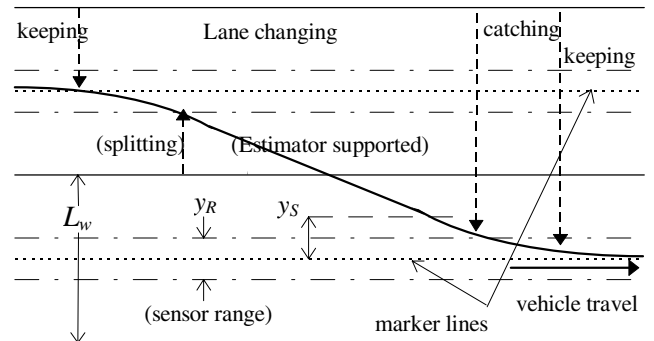

Fig. 8.1. Automated free lane change.

IX. HARDWARE AND SOFTWARE INTEGRATION

Eight Buick LeSabres were used in the platoon demonstration on the I-15 lanes, as well as one vehicle on the Mini Demo track. These vehicles were supported by add-on hardware devices and control software in order to deliver automated driving features such as close space following and tight lane tracking [see 5, 6 for detailed description]. Figure 9.1 illustrates the components in the test vehicle that relate to the steering control function.
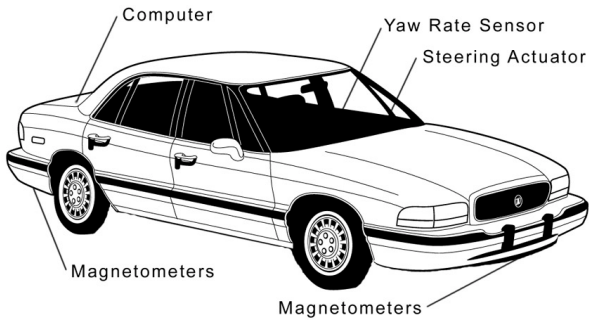
Fig. 9.1. Buick LeSabre test vehicle.

The hardware structure consisted of the following add-on devices:

(1) sensor (radar) to measure the distance between vehicles,
(2) sensors (magnetometers) to detect the lateral position of the vehicle relative to the center of the lane and the upcoming road geometry,
(3) communication links allowing the vehicle to exchange data with neighboring vehicles and roadside computers,
(4) control computer providing the intelligence needed for automated steering and speed control,
(5) electronically controlled steering, brake, and throttle actuators,
(6) human machine interface (HMI) allowing the driver to communicate with the automated vehicle.

The real-time software for vehicle lateral and longitudinal control was developed using C programming language under the real-time QNX operating system environment. The functions of the real-time software are to process the signals obtained from the sensors, the radar and the radio, to compute control commands based on those signals, and to send those control commands to the throttle, brake and steering actuators. The basic software structure is explained in Figure 9.2.
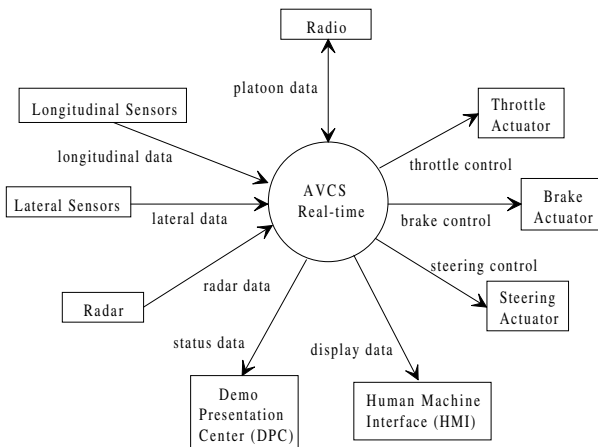

Fig. 9.2. Software structure for Buick LeSabre.

X. DEMONSTRATION RESULTS

Many data were collected and reviewed during the NAHSC preparation and demonstration. The test data at I-15 revealed that the tracking errors were generally within 5 centimeters with a maximum lateral error of 10 centimeters during curve transition at highway speed. Taking into account that the

magnet installation error is generally within 1.5 centimeters and that the standard deviation of the measurement error is about 0.4 centimeter, the steering controller is shown to maintain a consistently good tracking accuracy. The same algorithm as the one used for highway driving was applied to the high-g exhibition demonstration at the Miramar Mini Demo with consistent and robust performance. Over 400 consecutive successful automated free lane changes were performed at various locations of I-15 with different speeds. Over 1500 passengers rode in the automated vehicles, and no single failure occurred on the automated steering control system in all nine automated vehicles. The following figures present the capability, robustness, and versatility of the developed automated steering control system.

Figure 10.1 compares the steering performance between that of an experienced human driver and that of the automated steering control system for speed up to 80 mph. No road preview information was used during this test run. Comparable lateral acceleration (standard deviation STD: 0.24 m/s^2, maximum acceleration: 0.9 m/s^2) to a skilled manual driver (STD: 0.23 m/s^2, maximum acceleration: 1.2 m/s^2) was observed at I-15 but with much smaller tracking error for the automated steering system (STD of 3 vs. 11 centimeters, maximum error of 14 vs. 49 centimeters).
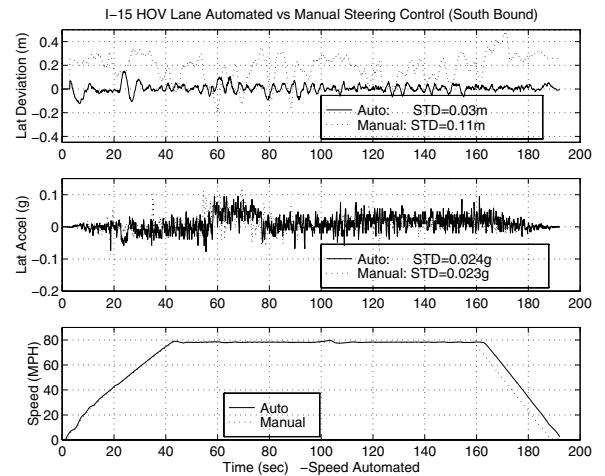

Fig. 10.1. Automated vs. manual steering comparison.

Figure 10.2 shows the automated lane-keeping performance during a platoon demonstration at 70 mph at I-15. The standard deviations of the tracking error for cars number 1, 2 and 3 are 3.0, 2.5 and 2.9 centimeters, respectively. The tracking errors stay within 9 centimeters over 99% of the time. Furthermore, the tracking performances among these three cars are almost identical at every location, which also demonstrates the consistency of the automated steering control algorithm. It is worthwhile noticing that identical steering controller is used in every vehicle.

Figure 10.3 illustrates the data from the Miramar Mini Demo where the lane-keeping capability was demonstrated through the high-g automated maneuver on a demanding test track. The automated steering control has consistently been demonstrated up to 0.5-g lateral acceleration with 95% of the tracking error within 10 centimeters. A couple of   sharp

transitions (54 meters radius of curvature) exhibit 20 centimeters tracking error but only during short transitions. Up to 0.7-g lateral acceleration has been maintained at the Miramar Demo site, however the demonstration speed was chosen to be far lower. Figure 10.4 shows a map for the Miramar Demo test track.
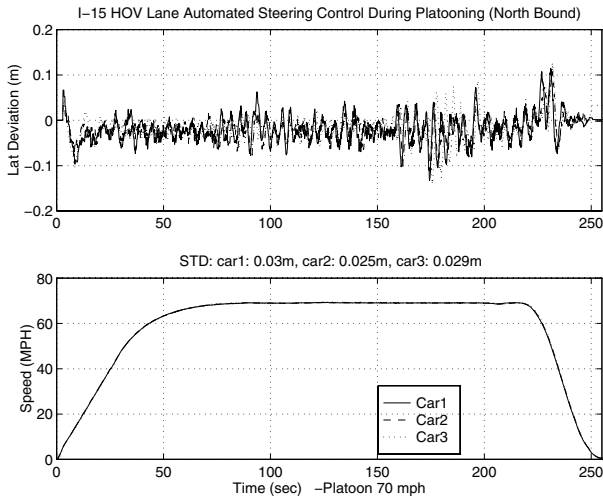

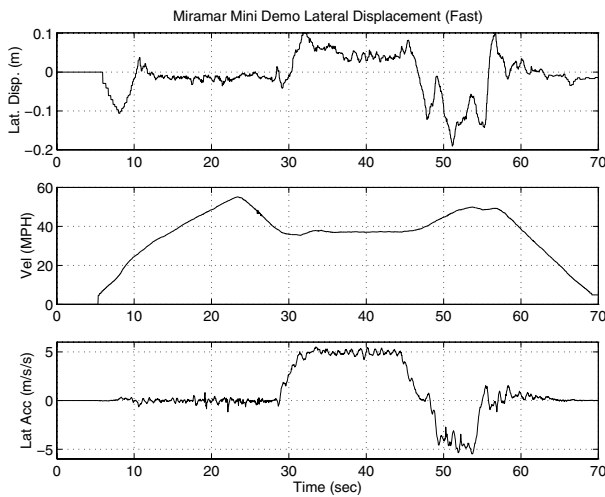Fig. 10.2. Platoon automated steering control performance.

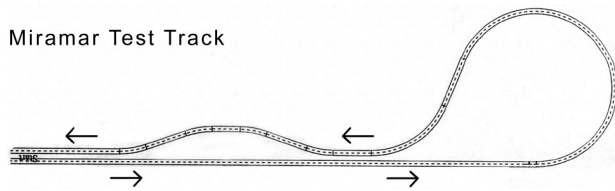Fig. 10.3. Automated steering control performance at Miramar Mini Demo.

Fig. 10.4. Miramar Mini Demo test track map.

Figures 10.5 and 10.6 illustrate an almost three-minute test segment with automated free lane-change maneuvers on I-15. The steering control was automated whereas the driver commanded brake and throttle to test the robustness with respect to various speeds. Five consecutive automated free lane changes were performed during this test run as indicated in Figure 10.5, with speed ranging from 63 mph to 78 mph (Figure 10.6). The sequence of state transitions during lane

change can also be observed in Figure 10.5. The vehicle first followed a desired lane-change trajectory (third order polynomials for this case) guided by the magnetic measurements until it left the sensor range (approximately ±0.53 meter). Instead of using the lateral measurements, the vehicle continued to track the same desired trajectory using the estimated displacement until the sensor saw the first magnet on the target lane at about 0.53 meter away from its center. At this time, the estimator readings were 2.90, -3.16, 2.75, -3.25 and 3.39 meters for the five lane changes. Since the corresponding correct estimation should be about ±3.1 meters (the lane width, 3.6 meters, minus the sensor range), the errors of these five estimates are within 0.35 meter. The vehicle then starts the lane catching function with a new desired trajectory calculated by third order polynomials whose coefficients are determined by the initial catching condition. The vehicle resumed lane keeping function after finishing lane catching.
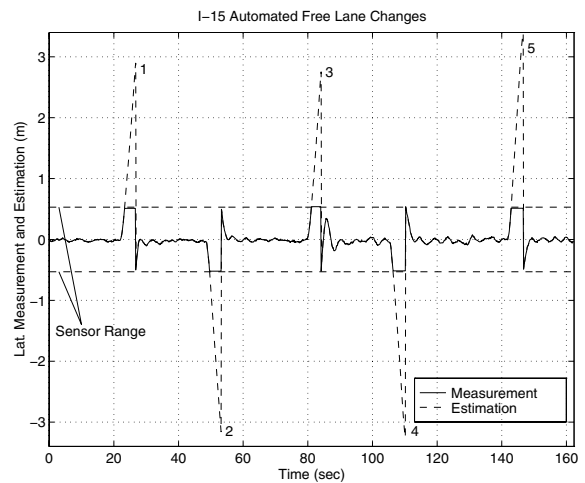

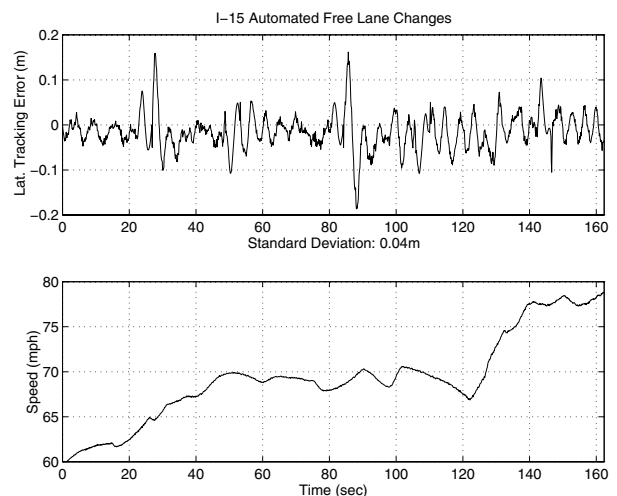Fig. 10.5. I-15 Automated free lane changes (measurement/estimate).

Fig. 10.6. I-15 Automated free lane changes (tracking error/velocity).

Figure 10.6 also illustrates the lateral tracking error, i.e. the error between the desired trajectory and either the lateral measurement or its estimate when the measurement is not available. The maximum tracking error is less than 0.2 meter. It is worthwhile noticing that errors that are more than 0.1 meter occur only during the lane-catching state, the most uncertain

state. The overall standard deviation of tracking error is 4 centimeters. Such tracking accuracy underscored the strong performance requirement for the lane-keeping controller.

XI. CONCLUSIONS

The systematic integration of mechanical systems and electronic devices played a crucial role in the development of automated vehicles. This paper demonstrates both the process and the results of such integration of an automated steering control system that uses magnetic markers embedded under the roadway for lateral guidance. The development process included the following integration: vehicle dynamics, smart steering actuator that incorporates the existing components with the new add-on devices, lateral sensing system that combines magnetometer with smart signal processing, inertial sensor with estimator that supports dead-reckoning lane change, as well as multi-level control functions that execute decision making, trajectory planning, feedback control and fault detection. The knowledge acquired from system analysis, the understanding of practical limitations, and the goal-oriented requirements guided the entire integration process. Without such diligent effort to integrate components, information, intelligence and control functions, the strong safety and performance requirements for a successful public demonstration could not have been achieved.

This automated steering control system was successfully demonstrated during the four-day August 1997 National Automated Highway System Consortium Feasibility Demonstration in San Diego. The same automated steering system was implemented on the platoon demonstration where eight vehicles were under full automation at 6.5 meter spacing and on the one vehicle high-g maneuver Mini Demo. Over 1500 passengers rode in the automated vehicles and no single failure occurred for the steering control system in all nine vehicles. The system achieved tight tracking error, good passenger comfort, and high robustness. This successful development process serves as a good example of mechatronic system design.

ACKNOWLEDGEMENT

REFERENCES

[1] W. Stevens, "The automated highway system program: A progress report", in *Preprints of the 13th IFAC World Congress (plenary vol.),* pp.25-34, San Francisco, CA, USA, 1996.

[2] S. Tsugawa, M. Aoki, A. Hosaka and K. Seki, "A survey of present IVHS activities in Japan", in *Preprints of the 13th IFAC World Congress (vol. Q),* pp.147-152, San Francisco, CA, USA, 1996.

[3] S. E. Shladover, "Review of the State of Development of Advanced Vehicle Control Systems," *Vehicle System Dynamics*, vol. 24, pp.551-595, July, 1995.

[4] J. G. Bender, "An overview of systems studies of automated highway systems", *IEEE Trans. on Vehicular Technology*, vol. 40, no. 1, pp. 82-99, 1991.

[5] H.-S. Tan, R. Rajamani, and W.-B. Zhang, "Demonstration of an Automated Highway Platoon System," in *Proc. American Control Conf.*, pp. 1823-1827, Philadelphia, PA, USA, June 1998.

[6] R. Rajamani, H.-S. Tan, B. Law and W.-B. Zhang, "Demonstration of Integrated Longitudinal and Lateral Control for the Operation of Automated Vehicles in Platoons," to appear *IEEE Transactions on Control Systems Technology*.

[7] E. D. Dickmanns and V. Graefe, V. "Application of Dynamic Monocular Machine Vision," *Machine Vision and Applications*, vol.1., no. 4, pp.241-261, 1988

[8] T. Jochem, D. Pomerleau, B. Kumar and J. Armstrong, "PANS: A Portable Navigation Platform," *Proceedings of Intelligent Vehicles Symposium*, Detroit, MI, USA, pp.107-112, 1995.

[9] Q. T. Luong, J. Weber, D. Koller, and J. Malik, "An Integrated Stereo-Based Approach to Automatic Vehicle Guidance," *Proceedings of the 5th ICCV*, pp. 52-57, 1995.

[10] A. Ünyelioglu and C. Hatipoğlu and Ü. Özgüner, "Design and stability analysis of a lane following controller," *IEEE Trans. on Control Systems Technology*, Vol. 5, pp. 127-134, Jan. 1997.

[11] R. E. Fenton, G. C. Melocik and K. W. Olson, "On the steering of automated vehicles: Theory and Experiment", *IEEE Trans. on Automatic Control*, vol. 21, no. 3, pp. 306-315, 1976.

[12] W. Darenberg, "Automatische Spurführung von Kraftfahrzeugen (in German)," *Automobil-In-dustrie*, pp. 155-159, 1987.

[13] R. J. Mayhan and R. A. Bishel, "A two-frequency Radar for Vehicle Automatic Control," *IEEE Trans. On Vehicular Technology*, vol. 31, no. 1, pp. 32-39, 1982.

[14] W.-B. Zhang and R. E. Parsons, "An Intelligent Roadway Reference System for Vehicle Lateral Guidance/Control," in *Proc. American Control Conf.*, San Diego, CA, pp.281-286, 1990.

[15] J. Guldner, H.-S. Tan and S. Patwardhan, "Analysis of Automatic Steering Control for Highway Vehicle with Look-down Lateral Reference Systems," *Vehicle System Dynamics*, vol. 26, no. 4, pp. 243-269, 1996.

[16] H.-S. Tan, J. Guldner, S. Patwardhan and C. Chen, "Changing Lanes on Automated Highways with Look-Down Reference Systems," in *Preprints of IFAC Workshop on Advances in Automotive Control*, pp. 69-74, Mohican State Park, OH, USA, Feb.1998.

[17] H. Peng and M. Tomizuka, "Vehicle lateral control for highway automation", *Proc. American Control Conf.*, San Diego, CA, USA, 1990, pp. 788-794.

[18] J. Guldner, S. Patwardhan, H.-S. Tan and W.-B. Zhang, "Coding of Magnetic Markers for Demonstration of Automated Highway Systems", *Preprints of the Transportation Research Board Annual Meeting*, Washington, DC, USA, 1997.

[19] J. Guldner, H.-S. Tan, and S. Patwardhan, "Study of Design Directions for Lateral Vehicle Control," *Proceedings of the 36th IEEE Conference on Decision and Control*, pp. 4732-4737, San Diego, CA, 1997.

[20] C. Chen and H.-S. Tan, "Steering Control of High Speed Vehicles: Dynamic Look Ahead and Yaw Rate Feedback," in *Proceedings of the 37th IEEE Conference on Decision and Control*, pp. 1025-1030, Tampa, Florida, USA, Dec. 1998.

[21] R. Sebastian, T. Kaufmann, F. Bolourchi and H.-S. Tan, "Design of an Automated Highway Systems Steering Actuator Control System," in *Proceedings of IEEE Conference On Intelligent Transportation Systems*, pp. 254-259, Boston, MA, USA, Nov. 1997.

[22] K.-T. Feng, H.-S. Tan and M. Tomizuka, "Automatic Steering Control and Validation of Vehicle Lateral Motion with the Effect of Roll Dynamics," in *Proc. American Control Conf.*, pp. 2248-2252, Philadelphia, PA, USA, June 1998.

[23] S. Patwardhan, H.-S. Tan, J. Guldner and M. Tomizuka, "Lane Following During Backward Driving for Front Wheel Steered Vehicles," in *Proc. American Control Conf.*, Vol. 5, pp. 3348-3353, Albuquerque, NM, USA, 1997.

[24] H.-S. Tan, J. Guldner, C. Chen, S. Patwardhan and B. Bougler, "Lane Change Maneuvers on Automated Highways with Look-Down Reference Systems," submitted for review to *IFAC Journal, Control Engineering Practice*.